THE UNIVERSITY OF CHICAGO

SYNTHESIS OF MERCURY CHALCOGENIDE COLLOIDAL QUANTUM DOTS AND CORE SHELLS

A DISSERTATION SUBMITTED TO

THE FACULTY OF THE DIVISION OF THE PHYSICAL SCIENCES

IN CANDIDACY FOR THE DEGREE OF

DOCTOR OF PHILOSOPHY

DEPARTMENT OF CHEMISTRY

BY

GUOHUA SHEN

CHICAGO, ILLINOIS

MARCH 2019

Table of Contents

List of Figures

List of Tables

List of Abbreviations

AOT	bis(2-ethylhexyl)sulfosuccinate
ATR	attenuated total reflection
BLIP	background-limited infrared performance
c-ALD	colloidal atomic layer deposition
CQD	colloidal quantum dot
DDAB	didodecyldimethylammonium bromide
DDT	dodecanethiol
DMSO	dimethyl sulfoxide
EDT	ethanedithiol
FA	formamide
IPA	isopropanol
IR	infrared
FMT	furanmethanethiol
FTIR	Fourier-transform infrared spectroscopy
FWHM	full-width at half maximum
$Hg(Ac)_2$	mercury acetate
ICP-MS	inductively coupled plasma – mass spectrometry
ICP-OES	inductively coupled plasma – optical emission spectrometry
LWIR	long-wave infrared
MBE	molecular beam epitaxy
MCT	mercury cadmium telluride

MEA	mercaptoethylamine
MWIR	mid-wave infrared
NC	nanocrystal
NMR	nuclear magnetic resonance
O.D.	optical density
OAcid	oleic acid
OAm	oleylamine
ODA	octadecylamine
ODE	octadecene
PC	photoconductor
PL	photoluminescence
PV	photovoltaics
QD	quantum dot
QY	quantum yield
RBS	Rutherford backscattering spectrometry
RT	room temperature
SCE	standard calomel electrode
SHE	standard hydrogen electrode
SWIR	short-wave infrared
TBP	tributylphosphine
TCE	tetrachloroethylene
TEM	transmission electron microscopy
TG	1-thioglycerol

THF	tetrahydrofuran
$(TMS)_2S$	bis(trimethylsilyl)sulfide
$(TMS)_2Se$	bis(trimethylsilyl)selenide
$(TMS)_2Te$	bis(trimethylsilyl)telluride
TOP	tri-n-octylphosphine
TOPO	trioctylphosphine oxide
w-	wurtzite
XPS	X-ray photoelectron spectroscopy
XRD	X-ray diffraction
zb-	zinc-blende

ACKNOWLEDGEMENTS

Time flies. In the blink of an eye, I have already spent more than five years in PGS lab. Here, I want to first express my gratitude to Professor Philippe Guyot-Sionnest for his supervision and support duing my PhD. Philippe is a big name in the field of quantum dots, who has done many pioneer works including the first core/shell synthesis, first electrochemistry doping and first air-stable intraband transition. Philippe is a physicist with a strong instinct. Given a new system, he could very quickly analyze it from basic theory, design experiments and find its unique properties. My former group member Wei Qin once expressed his admiration by saying anyone who has 30-40% of Philippe's problem-solving skills would live confortably under any circumstances. It is truly a great honor for me to work with Philippe and learn from a person who has a deep insight and really enjoys scientific research.

I would like to thank all faculties in the chemistry department, especially Professor Bozhi Tian and Professor Dmitri Talapin, who generously agreed to be in my dissertation committee. Bozhi and Dmitri are both working on nanoscale materials and have made many fundamental discoveries from synthesis to applications. I have been talking and discussing a lot with them and their knowledge has always been inspiring to me.

I am very thankful to all current and former group members in PGS lab. PGS lab is usually small, 5-6 members at most, but we collaborate and work together closely. During the past ten years, our group has been one of the pioneers in the field of infrared photodetection. Dr. Sean Keuleyan, Dr. Heng Liu, Dr. Emmanual Lhuillier, Dr. Zhiyou Deng, Dr. Kwang Seob Jeong, Menglu Chen, Matt Ackerman, Chris Melnychuk and Dr. Xin Tang, tens of PhD and post-doc have been contributing to the problem and after years of hard-working, we are finally coming close to real products. It is a great honor that I am able to contribute in the process.

I want to express my gratitude to Qiti Guo, Justin Jureller, Yimei Chen, Joe Austin and Alex Filatov, who have been very knowledgeable and patient in the instrument training sessions. No result could be obtained without their help and instructions.

I would like to give a special thanks to Meishan Zhao and Melinda Moore. They helped me, as well as all international students a lot. I wouldn't be able to go through the first year transition period without their support.

Finally, I would like to thank my friends and family, who make the life much easier for me. I still remember the loneliness I felt during the first night at Chicago, when everything seems so different and unreal. Luckily, I have them in my corner. Thanks!

Abstract

Mercury chalcogenide colloidal quantum dots based infrared photodetection has been intensely studied in the past few years and achieved background limited detectivity, sub-microsecond response time and much lower cost compared with the current leading technologies. To further improve their performances, new synthetic protocols need to be developed to tackle some of the current difficulties such as the control of doping-level and improvement in mobility and quantum yield. In this thesis, I focused on the synthetic efforts to obtain mercury chalcogenide quantum dots with better morphology and properties. For HgTe, non-aggregated HgTe quantum dots were synthesized for the first time and stabilized in the absence of thiols. HgTe/CdTe core/shells were then grown from these cores and showed much improved thermal stability. For HgSe, I used selenourea-derivatives to lower the precursor reactivity and obtained HgSe quantum dots with a better monodispersity around 6-7%. HgSe/CdX (X=S, Se, Te) core/shells were synthesized by both hot-injection and c-ALD methods and showed improved thermal stability and intraband PL quantum yield. The intraband PL quantum yield reached 10^{-3} at 5 μm. For HgS and HgS/CdS, a novel 2-phase method was used to provide an easy way of synthesizing these materials. The gradual transition from intraband to surface plasmon resonance was observed in HgS quantum dots and was explained by considering the local field effect. These methods open up possibilities to use these materials in current applications and new scenarios.

Chapter 1 Introduction

Colloidal quantum dots (CQDs) are a group of semiconductor materials that have discrete energy levels due to the quantum confinement effect. As a result, they have two significant differences from their bulk counterparts. First, the bandgap of CQDs is decided by the confinement energy, which is directly related to the particle sizes. This allows us to use the same material to cover a large range of the spectrum simply by tuning some synthetic parameters. Second, CQDs have energy levels instead of bands in the conduction and valance "bands", which makes intraband transitions available in these systems (e.g., the $1S_e - 1P_e$ transition shown in Figure 1-1).

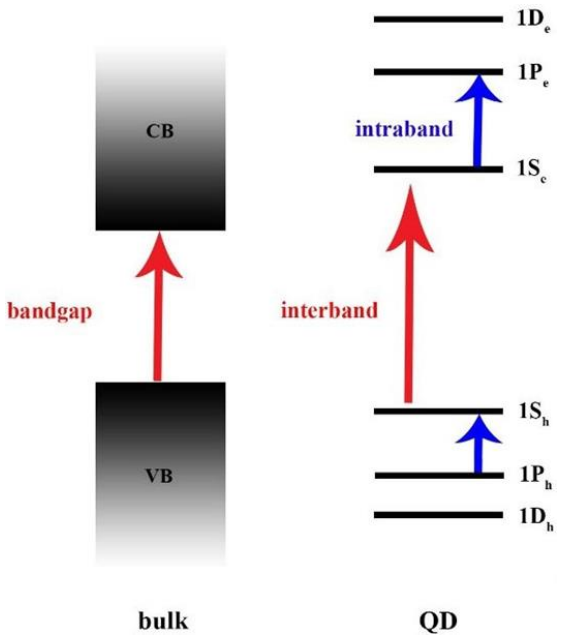

Figure 1-1 *Energy levels of bulk semiconductor and semiconductor quantum dot.*

The focus of this thesis is mid-infrared CQDs. As suggested above, there are usually two strategies to make CQDs that have infrared transitions. One is to start from small gap or even zero gap semiconductors or semimetals and make their corresponding CQDs. The other is to dope the CQDs

and use their intraband transitions instead of interband. In principle, any CQD system can be used as an infrared material with proper doping.

1.1 CQDs in Mid-Infrared Photodetection

1.1.1 Mid-Infrared Photodetection Technologies

The main purpose of developing mid-wave infrared (MWIR: 3-5 μm) CQDs is to make infrared photodetectors in this important atmospheric window. Currently, the most widely-used MWIR detectors are bolometer and bulk mercury cadmium telluride ($Hg_{1-x}Cd_xTe$, MCT) detector.[1-3] Bolometer is a thermal detector and uses the thermal effect of infrared light, where the heat-induced temperature change is recorded in the form of electric resistance difference. It is the dominant detector on the consumer thermal imaging market due to its low cost and room-temperature operation. On the other hand, for some more sophisticated applications such as military and scientific research, MCT detectors are chosen because of their higher detectivity and faster response time. However, MCT detector requires large and expensive molecular beam epitaxy (MBE) system to grow and usually needs to operate at low temperatures (e.g., liquid N_2 at 77 K) to suppress the Auger relaxation process and improve detectivity.

With CQD photodetector, there is a hope to combine the advantages of both systems. First, the solution-based synthesis and processing makes CQD much cheaper than MCT; Second, CQD photodetectors have already demonstrated a high detectivity and sub-microsecond response time that is comparable to some of the commercial products;[4] Third, a recent study showed that HgTe CQDs have a 3-order magnitude smaller Auger coefficient compared with the same band gap bulk MCT.[5] In principle, the suppressed Auger relaxation in CQDs will allow a higher operating temperature than MCT.

1.1.2 HgTe as Photodetection Material

Bulk HgTe is a semimetal, which has an inverted band structure due to its large spin-orbit coupling. As a result, HgTe CQDs should be able to cover the whole IR range. Currently, HgTe is the most studied CQD material for IR photodetection, which can work as photoconductors (PC) or photovoltaics (PV). Since 2011, there have been more than 5 studies that demonstrated the use of HgTe for 3-5 μm (mid-IR) photodetection, which are summarized in Table 1-1.

Table 1-1 Summary of mid-infrared HgTe photodetector

Year	Wavelength (μm)	Temp (K)	D^* (Jones)	Mode	Comment	Reference
2011	5	130	2×10^9	PC	first PC device	6-7
2013	3.5	230	3.5×10^{10}	PC	As_2S_3 matrix	8
2015	4	140	1.14×10^{10}	PV	first PV device	9
2018	4	100 200	10^{11} 10^{10}	PV	$HgCl_2$ treatment	4
2018	4.5	85 295	4×10^{11} 7.2×10^8	PV	plasmon and interference	10

As shown in Table 1-1, currently the best devices are HgTe PV with $HgCl_2$-treated Ag_2Te layer and optical enhancement structures. It exhibits background-limited infrared performance (BLIP) for temperatures below 200 K. However, MCT detector still outperforms it at higher temperatures.

1.1.3 HgSe and HgS as Photodetection Materials

Bulk HgSe is a semimetal while HgS band gap is uncertain, with various values reported from -0.5 eV to 0.6 eV.[11-14] Nevertheless, both materials should be able to work in mid-IR in their quantum dot form. However, later experiments showed that unlike HgTe, HgSe and HgS CQDs are naturally n-doped and exhibit intraband transitions instead of interband. In 2014, Zhiyou et al. first demonstrated the use of HgSe CQDs as an intraband photoconductor at 4.5 μm with a detectivity $D^* = 2 \times 10^9$ at 80 K.[15] However, the difficulty to precisely control the doping level at 2 e^-/dot in HgSe and HgS greatly limits their performances. This is because any deviation from 2 e^-/dot would cause a faster recombination process and larger dark current. As a result, there are only a few reports on intraband photodetector with limited detectivity.[16-17] One possible solution would be to use HgSe or HgS in PV devices. This requires some precise energy level matching between the active materials and the electron and hole transport layers. Another approach is to further improve the monodispersity of the particles to minimize the disorder coming from the inhomogeneity in size.

1.1.4 Other Possible Infrared CQD Materials

One of the biggest challenges in mercury-based photodetector research and commercialization is the toxicity of mercury compounds. As a result, people are always looking for better substitutes. One possible choice is Ag_2Se, which has a narrow band gap ~0.15 eV in its bulk form.[18] In 2011, Norris and his co-workers first synthesized Ag_2Se CQDs with good monodispersity and shape control.[19] However, only visible and near-infrared spectra were investigated at the time, which showed no excitonic feature. One year later, the same group revisited the material in the mid-infrared region and found Ag_2Se CQDs had tunable infrared absorption from 3 μm to 6 μm.[20] In 2018, Kwang and his co-workers used spectroelectrochemistry technique to study this material

and observed a bleach in its mid-infrared absorption peak and an emergence of a near-infrared peak as the electrochemistry potentials moved more negative (more n-type).[21] As a result, they assigned this mid-infrared absorption to the $1S_e$-$1P_e$ intraband transition and not the band gap transition Norris suggested. Three months later, Emmanuel Lhuillier's group used X-ray photoemission to study the material and confirmed that the environmental Fermi level was between the $1S_e$ and $1P_e$ states.[22] This makes Ag_2Se CQD a promising material to be used in intraband photodetection to replace HgSe and HgS.

Another choice is SnTe, which has a bulk band gap of 0.18 eV.[23-24] In 2007, Kovalenko et al. synthesized SnTe CQDs with the reddest absorption at 3.5 μm and attributed this to the $1S_h$-$1S_e$ transition.[25] In 2011, SnTe CQDs were synthesized in polar solvents and also exhibited a mid-infrared absorption ~3.4 μm.[26] Klimov and his co-workers pushed the synthesis of SnTe even further with a better shape control and obtained nanocubes and nanorods with different aspect ratios. A 36 × 16 nm nanorod had an absorption onset ~3.3 μm.[27]

SnTe can be mixed with another narrow gap material PbTe (bulk band gap of 0.29 eV) to form $Pb_{1-x}Sn_xTe$. And its minimum band gap is obtained when x equals 0.67. As a result, $Pb_{0.33}Sn_{0.67}Te$ CQDs with 4.4 nm diameter size had a 4.4 μm absorption transition.[28]

1.2 Synthesis of Mercury Chalcogenide CQDs

Since the first colloidal synthesis of CdSe in 1993, hundreds of CQDs have been made.[29] However, compared with the large library of CdSe, mercury chalcogenide CQDs synthesis lags far behind, where only ~15 synthetic papers have been published since the first aqueous synthesis of HgTe CQDs in 1999.[30]

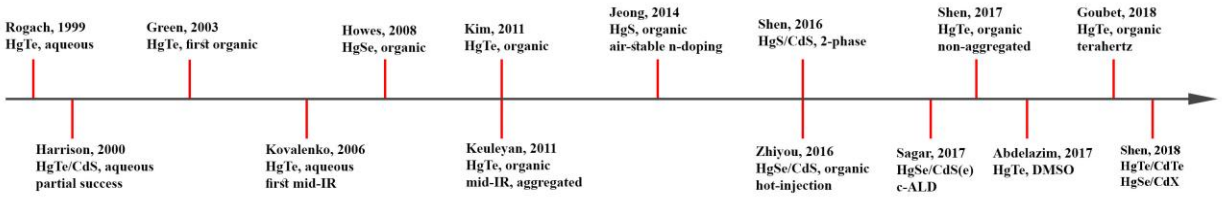

Figure 1-2 *Timeline of mercury chalcogenide CQDs synthesis.*

The main difficulties in mercury chalcogenide CQD synthesis are: the toxicity of mercury compounds, the limited stability of mercury precursors at elevated temperatures, the small library of chalcogenide precursors with suitable reactivity and the tendency to aggregate, especially for HgTe CQDs. The difficulty to build mid- and long-IR optics also makes it harder for researchers to study their optical properties.

1.2.1 Synthesis of HgTe CQDs

The synthesis of HgTe CQDs can be classified into two categories: polar and nonpolar. The polar synthesis usually takes place in solvents such as H_2O and DMSO, where inorganic mercuric salts react with chemically- or electrochemically-generated H_2Te gas. Meanwhile, nonpolar synthesis requires some organic solvents, most commonly long chain amines, and is usually done in an air-free, water-free environment.

The first polar synthesis, which is also the first HgTe CQD synthesis, was done by Rogach et al. in 1999.[31] In this report, $Hg(ClO_4)_2$ was dissolved in H_2O at pH 11.2 and reacted with H_2Te, the latter was generated via Al_2Te_3 and H_2SO_4 hydrolysis. To stabilize the quantum dots, 1-thioglycerol (TG) was used as ligand. The resulting particles were strongly aggregated with sizes varied from 3 nm to 6 nm. Their optical properties were also not satisfying. The dots exhibited a

broad absorption spectrum with no excitonic feature. The PL, which was peaked at ~1.1 μm, had a FWHM more than 400 nm. This structural and optical quality makes the dots not suitable for real applications in the telecommunication infrared region. However, there are several general rules that are important for later HgTe CQDs syntheses. First, cubic (zinc-blende) HgTe is always the final product; second, thiols are good capping ligands for HgTe because of the strong chemical bond between mercury and sulfur; third, the presence of thiols in aqueous synthesis limits the size of the particles and makes their absorption only in the near-infrared.

In 2006, Kovalenko et al. successfully synthesized HgTe CQDs that covered a large spectrum range from 1.2 μm to 3.7 μm.[32] To overcome the size limitation shown by Rogach, the authors used a special 3-step approach: aqueous synthesis → ligand exchange → Ostwald ripening. First, small HgTe CQDs were synthesized using the same $Hg(ClO_4)_2$ and H_2Te reaction, the only differences were that the H_2Te gas was generated via electrochemistry to better control the reaction rate and mercaptoethylamine (MEA) or TG can both act as stabilizing ligand. The particles, which had an absorption ~1.2 μm, were ligand exchanged to the nonpolar CCl_4 phase by adding excess 1-dodecanethiol (DDT). Cooking the transferred dots at 75-80 °C greatly increased the particle sizes and quantum dots as large as 9 nm were obtained. This synthetic protocol, which was able to produce HgTe CQDs with good size tunability, clear excitonic feature and reasonably narrow PL peak, was an important advance from the first aqueous synthesis. Moreover, the relationship between PL quantum yield (QY) and emission wavelength was investigated, which is shown in Figure 1-3.

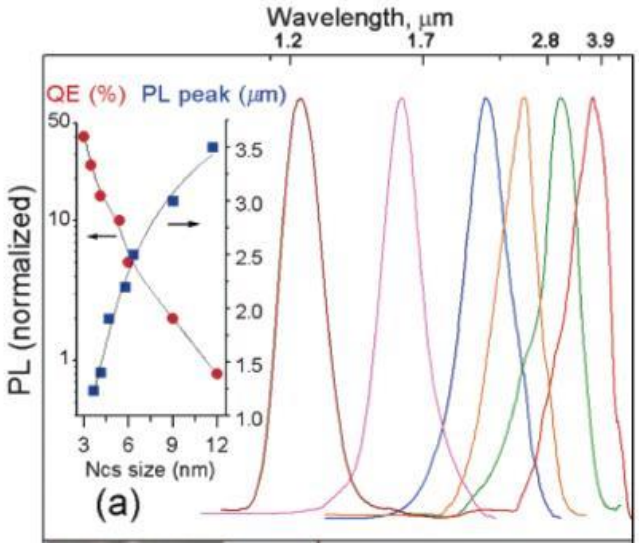

Figure 1-3 *PL spectrum and quantum efficiency of HgTe CQDs. Adapted from reference 32.*

From 1.2 μm to 3.7 μm, the PL QY of HgTe CQDs drops 2 orders of magnitude. The exact origin of the low PL QY in small gap CQD materials has been a puzzle and will be discussed in detail in section 3.3.

In 2017, Rogach and his co-workers came up with another synthesis of HgTe, this time in aprotic DMSO.[33] Without any postsynthetic treatment, the authors made HgTe CQD as red as 3 μm, which is the biggest dots in any one-step polar synthesis. The key to grow bigger dots is the use of DMSO. Compared with H_2O, DMSO cannot support a large hydrogen bond network, which might be the reason that there were less interactions between particles and therefore less aggregation at large sizes. In addition, the authors also developed a computer-controlled electrochemistry setup to better control the releasing of H_2Te gas. The synthesized HgTe CQDs had a good PL QY, ~17% at 2070 nm, which is the highest at the wavelength. However, the dots were still very poor in terms of monodispersity (size distribution up to 55%) and shape control (a lot of irregular shapes). As a result, the PL peak was very broad, which had a FWHM ~800 nm at 2000 nm.

To summarize, polar synthesis of HgTe CQDs usually faces the problems of poor size and shape control as well as small particle sizes. To make particles in the mid- or long-IR range, organic synthesis is needed.

The first organic synthesis was done by Green et al. in 2003.[34] In this synthesis, $HgBr_2$ was dissolved in trioctylphosphine oxide (TOPO) and octadecylamine (ODA) under Schlenk line at 70 °C. Trioctylphosphine telluride (TOPTe) was then injected into the mixture and reacted for 30 min. The obtained particles had an average size of 17 nm with a large size dispersion ~30%. Their shapes were also irregular, with a large proportion being teardrop-shaped rather than spherical. The authors did not find any absorption feature or PL in the visible or near-IR region.

Although this organic synthesis failed to give HgTe CQDs with good optical properties, it pointed out a way to grow large HgTe quantum dots. More importantly, the authors used amine-dissolved mercury halide salts and TOPTe as the mercury and tellurium precursors, respectively, which are still the most commonly used precursors nowadays. If the authors had checked the mid-IR spectrum of the dots with proper instruments, we may not need to wait for another 8 years to see the first mid-IR application of HgTe CQDs.

In 2011, Sang-Wook Kim and his co-workers developed a synthesis by using a combination of oleylamine and 1-dodecenethiol (DDT) as ligand.[35] By varying the reaction temperatures from 60 °C to 100 °C, the authors made particles with diameter from 3.6 nm to 7.2 nm and corresponding emission from 1050 nm to 1420 nm. However, there might be some problems in this paper because later experiments showed a 7.2 nm dot should give an emission ~3 μm, much redder than the value of 1.4 μm they reported.

Almost at the same time of Sang-Wook Kim's report, Sean Keuleyan from Philippe Guyot-Sionnest's group came up with a new synthesis of HgTe CQDs, which might be the most important synthetic paper in HgTe.[36] Compared with Green's synthesis, Sean removed the unnecessary part of TOPO and used oleylamine as both solvent and ligand. The precursor concentration was also lowered ~4-5 times, which greatly decreased the number of nucleation events and put the particle growth under better control. Sean also added a long-chain thiol (DDT) during the cleaning step, which provided the dots with long-time stability in air. The obtained HgTe CQDs had great size tunability, sharp absorption edge, clear excitonic feature as well as strong PL in the IR. The absorption and PL spectra are shown in Figure 1-4.

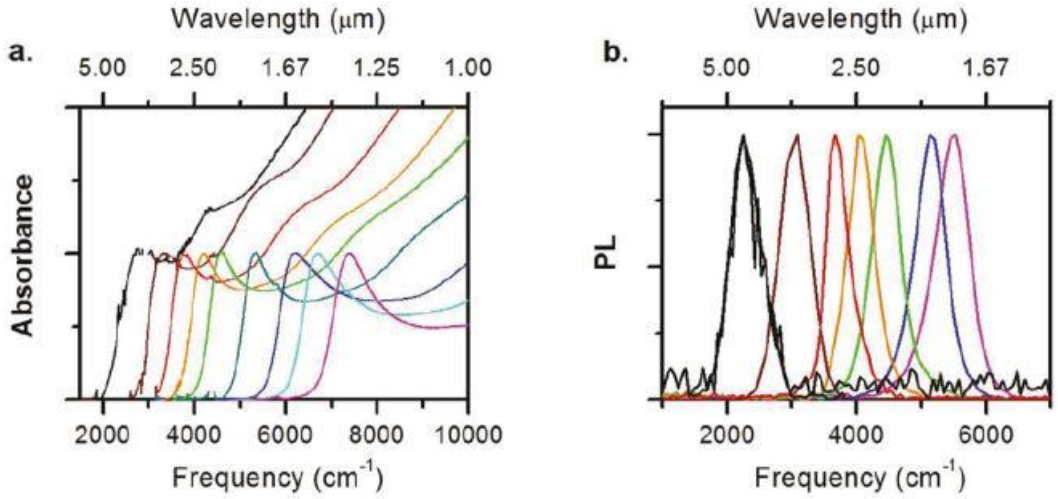

Figure 1-4 *Normalized (a) absorption and (b) PL spectrum of HgTe CQDs. Adapted from reference 36.*

These excellent optical properties make HgTe CQDs possible for many IR applications. Nowadays, most HgTe-based IR devices are using this synthesis.[4, 6-10, 37-41]

In 2014, Sean improved his previous synthesis by using a much more diluted TOPTe precursor (0.02 M TOPTe vs the previous 1 M).[42] The diluted TOPTe had a much lower reactivity, therefore allowed a more homogenous reaction mixture to form before any significant nucleation and growth started. Moreover, a sudden drop of temperature because of the large injection volume also helped lowering the precursor reactivity. HgTe CQDs with better monodispersity were obtained this way, and their absorption spectra showed up to 5 excitonic features.

The above organic syntheses of HgTe CQDs were all done at temperatures ~70-120 °C. This is because mercury halide-amine precursor tends to be reduced to Hg(0) when heated at higher temperatures for a long time. However, in 2018, Lhuillier and his co-workers made a small modification by injecting both mercury and tellurium precursors into a very hot amine solvent, with temperatures as high as 300 °C.[43] The authors found that the mercury precursor stayed stable if the reaction duration was short. By deploying this high-temperature, short reaction time strategy, extremely large HgTe nanoparticles (as big as 200 nm) could be obtained. These large particles, which were well above the Bohr radius of HgTe, showed a clear plasmonic peak in the terahertz region. The same protocol could be used to synthesize large HgSe and HgS nanoparticles.

In summary, compared with polar synthesis, organic synthesis of HgTe CQDs gives a much better size tunability and size dispersion. As a result, their absorption and PL peaks are also much narrower. However, the toxicity of organomercury compounds is a major concern.

Besides these 0-dimensional HgTe CQDs, 2D HgTe (or HgSe) nanoplatelets have also been made by cation exchange with their cadmium counterparts.[44-47] However, they are beyond the scope of this thesis and will not be discussed here.

1.2.2 Synthesis of HgSe and HgS CQDs

Compared with HgTe, there are even fewer reports on HgSe or HgS CQDs. In 2002 and 2003, Mattoussi and his co-workers published a series of papers on the syntheses of binary HgS, HgSe and ternary $HgSe_{1-x}S_x$ CQDs using an inverse-micelle approach.[48-49] The general idea of the inverse-micelle growth is to separate mercury and chalcogenide precursors in two phases and uses a surfactant, bis(2-ethylhexyl)sulfosuccinate (AOT) in these cases, to support a slow mass transfer across the phase interface. Therefore, CQD nucleation and growth are under better control. Here, the mercury precursor was mercury acetate ($Hg(Ac)_2$) dissolved in water and chalcogenide precursors were bis(trimethylsilyl)sulfide ($(TMS)_2S$) and bis(trimethylsilyl)selenide ($(TMS)_2Se$) in hexane. Mixing the two phases with AOT and some stabilizing ligand (such as TG) quickly formed CQDs. The dots were generally quite small, with absorption and emission between 500 nm to 800 nm. However, aggregation was still a problem in these syntheses.

In 2008, Howes et al. developed a new polar synthesis of HgSe CQDs.[50] The authors dissolved mercury acetate and TOPO in ethanol, then injected trioctylphosphine selenide (TOPSe) at room temperature to grow small HgSe CQDs. The dots were heavily aggregated with an average size of 4.9 nm and the authors claimed they had an excitonic shoulder ~3 eV. However, later experiments proved that a 4.9 nm HgSe dot should only give intraband absorption ~5 μm (0.25 eV). Possible reasons could be that the authors mis-identified some absorption peaks from impurities or that there were some HgSe clusters acting as intermediates. Another interesting finding was that there seemed to be a correlation between particle shape and TOPO concentration, with lower TOPO concentrations yielding more tetrahedral shapes. This was likely due to the fact that the surface ligands (TOPO) preferentially bind to some facets of the dots, likely (111) in this case, when their

concentrations cannot support a full surface coverage. This will then let the dots grow along (100) crystallographic directions.[51]

Zhiyou Deng and Kwang Seob Jeong from Philippe Guyot-Sionnest's group developed the first organic synthesis of HgS CQDs in 2014, inspired by the HgTe synthesis by Sean.[11] The mercury precursor was $HgCl_2$ in oleylamine and the sulfur precursor was thioacetamide. Thioacetamide is a precursor with high reactivity. As a result, the synthesis was done at room temperature and the resulting CQDs had a large size dispersion ~20% at 5-6 nm diameter. The most important finding from this paper was the ambient n-doping of HgS CQDs and the intraband transition at 5 μm, which will be discussed later in section 1.3.1.

In 2014, Zhiyou Deng from Philippe Guyot-Sionnest's group synthesized HgSe CQDs following a similar approach as Sean and Kwang.[15] The mercury precursor was still $HgCl_2$-oleylamine and the selenium precursor was selenourea. Later reports showed that urea-based chalcogenides (thiourea and selenourea) in amine were an important group of precursors in II-VI CQD synthesis, mainly because of their slow releasing rate, no introduction of new ligands and a high reactivity tunability.[52-54] As a result, the HgSe CQDs had a better monodispersity than Kwang's HgS, which was ~12% at 6.2 nm diameter. Similar to HgS, HgSe CQDs also featured an air-stable intraband transition, and this paper highlighted the first mid-IR intraband photodetector.

To summarize section 1.2.1 and 1.2.2, the general trend of mercury chalcogenide CQD synthesis is the pursuit for better dots, with wider size tunability, smaller size dispersion and less aggregation. To achieve this, organic syntheses become more and more dominant. A list of all mercury chalcogenide syntheses and their synthetic parameters is shown in Table 1-2.

Table 1-2 Summary of mercury chalcogenide synthesis

Ref	Hg precursor, amount (mmol)	X precursor, amount (mmol)	Hg/X	Solvent, volume (mL)	Ligand, amount (mmol)	Temp (°C)	Size (nm), Dispersion	Absorption (μm)	PL (μm), PL QY
15	$HgCl_2$, 0.1	selenourea, 0.1	1	OAm, 4	OAm, 19	110	5.5-6.2, 12%	4-5	4-5, NA
11	$HgCl_2$, 0.3	thioacetamide, 0.3	1	OAm, 10	OAm, 48	RT	6.4, 20%	5	5, NA
50	$Hg(Ac)_2$, 0.11	TOPSe, 0.13	0.85	ethanol, 20	TOPO, 1.3	RT	4.9	no feature	no emission
48	$Hg(Ac)_2$, 0.01	$(TMS)_2S$, 0.01	1	H_2O, 0.11 cyclohexane, 20 hexane, 10	TG, 0.01	RT	1-5	0.5-0.8	0.6-0.8, < 1% 5-6% with Cd/Zn
43	HgX_2, 0.1 (X=Cl, Br, I)	TOPTe, 0.1	1	OAm, 10	OAm, 48	120-340	5-200	2-65	no emission
42	$HgCl_2$, 0.1	TOPTe, 0.1	1	ODA, 3.3 OAm, 5	ODA, 11 OAm, 23	60-120	5-20	1.5-5, no feature	1.5-5, NA 7.7, NA
36	$HgCl_2$, 0.1	TOPTe, 0.1	1	OAm, 4	OAm, 19	60-100	aggregation	1.5-5	1.5-5, NA
35	$Hg(Ac)_2$, 0.25	TOPTe, 0.1	2.5	diphenyl ether, 4	OAm, 0.5 DDT, 0.5 TOP, 3	60-100	3.6-7.2, <7%	0.9-1.3	1.05-1.42, 10%
34	$HgBr_2$, 1.38	TOPTe, 1.3	1.06	TOPO, 11 ODA, 6	TOPO, 25.8 ODA, 18.5 TOP, 4	70-100	17, 30%	no feature	no emission
33	$Hg(Ac)_2$, 0.4	H_2Te, NA	NA	DMSO, 300	FMT, 0.8	RT	4.4, 55%	NA	1.2-2.1, 17%
32	$Hg(ClO_4)_2$, 2.72	H_2Te, 1.36	2	H_2O, 250	MEA, 7.88	RT, post-heat at 75-80	3-10, good	1.2-2.7	1.2, 40% 3.5, 0.5-2%
31	$Hg(ClO_4)_2$, 2.35	H_2Te, 0.14	16.8	H_2O, 125	TG, 5.77	RT	3.5, large	no feature	1.1, 48%

1.2.3 Synthesis of Mercury Chalcogenide Core/Shell Heterostructures

Since the first CdSe/ZnS quantum dot synthesis in 1996, growing core/shell heterostructures has been a standard approach to improve CQD stability, increase PL QY and achieve some unique carrier distributions.[55-56] However, for mercury chalcogenide CQDs, there are three main difficulties in core/shell growth. First, CQD aggregation has been a big problem, especially for those synthesized in polar solvents. Growing core/shell on these aggregated dots will result in precipitation or partial shell coverage. Second, to improve stability, mercury chalcogenide CQDs are usually protected by thiols. The Hg-S bond is so strong that it becomes difficult to expose the "fresh" core surfaces in order to let the shell precursors nucleate on them. Third, mercury chalcogenide CQDs have poor thermal stability. They will start sintering and losing their quantum confinement at temperatures as low as 100 °C, which is well below the growth temperatures of most shell materials such as CdSe and ZnS. As a result, very reactive chalcogenide precursors need to be used to lower the growth temperature. This will then increase the chance of secondary nucleation of shell materials. In effect, aggregation morphology, thiol ligands and thermal stability are the reasons why there are less than 5 core/shell papers ever published.

In 2000, Rogach et al. developed a synthesis of HgTe/CdS core/shell.[57] HgTe CQDs were still made by $Hg(ClO_4)_2$ and H_2Te in H_2O. The freshly-made cores were diluted in H_2O with $Cd(ClO_4)_2$. H_2S gas was then injected into the solution at room temperature to grow CdS shell. The absorption of HgTe/CdS red-shifted from HgTe cores, which had an excitonic feature moving from 850 nm to 920 nm. To verify the shell growth, the authors did an annealing test by refluxing the as-prepared HgTe and HgTe/CdS solution at 100 °C for 30 min. After heating, the PL of HgTe cores completely quenched, while HgTe/CdS kept half of the PL intensity with much broader PL peak.

This indicated that the shell could partially protect the cores. The authors did provide other proofs. The TEM images exhibited a darker core portion and a thick lighter shell portion (thickness > 2 nm), likely caused by the different contrast of Hg and Cd under electron beam. The XRD spectrum showed that the HgTe/CdS CQDs were still zin-blende, but their peaks were shifted from the positions of bulk HgTe to bulk CdS, which also indicated a CdS growth.

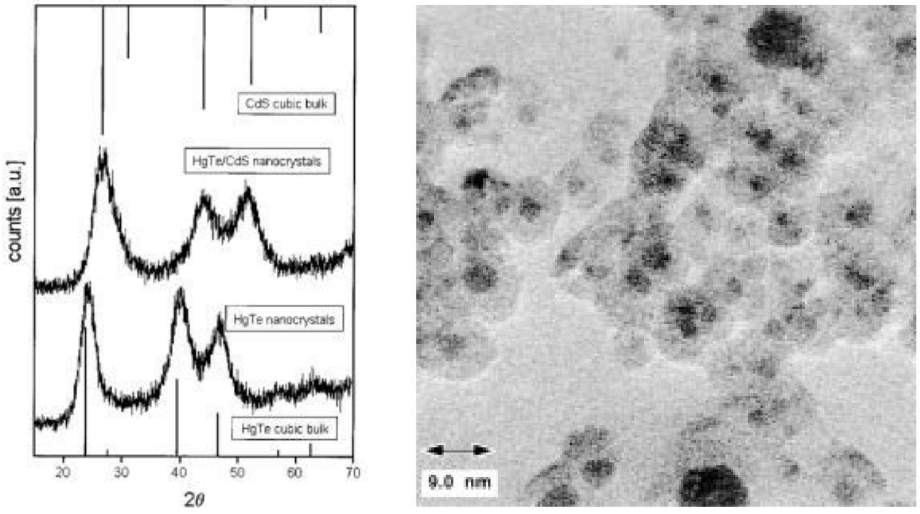

Figure 1-5 *(left) XRD of HgTe and HgTe/CdS; (right) TEM of HgTe/CdS. Adapted from reference 57.*

From the prospective of today's researchers, the first core/shell synthesis was only partially successful. First, the lattice mismatch between HgTe and CdS is larger than 10%, which means CdS is not a good shell material for HgTe from the beginning. As a result, growing a CdS shell with a thickness > 2 nm (> 6 monolayers) is almost impossible. Second, if there were such a thick CdS shell, annealing HgTe/CdS at 100 °C would not have caused such a big PL broadening and intensity drop. Third, the XRD peak width of HgTe/CdS was broader than HgTe cores (Figure 1-5). From Scherrer equation, this simply means the average grain size of HgTe/CdS is smaller than

HgTe, which is also impossible. In conclusion, there might be 1-2 monolayers of CdS attached to the HgTe surface that partially protects the cores from annealing. But most CdS should exist in the form of secondary nucleation. The TEM image could also suffer from over-focusing, which shows extra white rings around particles.

It was until 2016 that the first successful mercury chalcogenide core/shell came out.[58] Zhiyou Deng from Philippe Guyot-Sionnest's group deployed a standard hot-injection method to grow HgSe/CdS core/shell. The HgSe cores were prepared by $HgCl_2$-amine and selenourea, which were then cleaned and reheated to 100 °C. Cadmium oleate and H_2S were injected stepwise to grow CdS with certain thicknesses. TEM showed an increase in size from 5.8 nm to as large as 8.5 nm diameter with obvious secondary nucleation. XRD peaks of HgSe/CdS shifted from bulk HgSe to bulk CdS. More importantly, the XRD linewidth of HgTe/CdS had no change after annealing at 200 °C for 10 min, while HgTe greatly narrowed under the same condition, indicating a sintering. This excellent thermal stability is a strong proof of a complete shell protection.

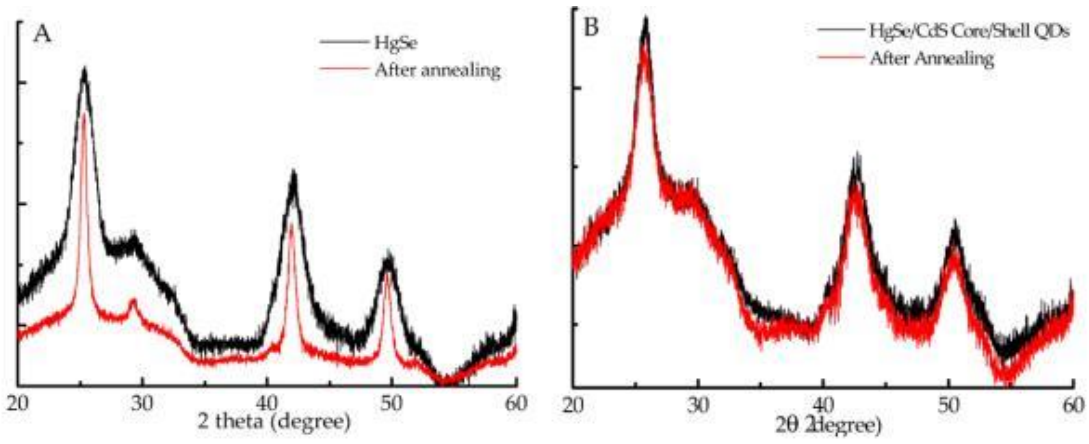

Figure 1-6 *(left) HgSe core and (right) HgSe/CdS core/shell XRD before (black) and after (red) 200 °C annealing for 10 min. Adapted from reference 58.*

The absorption and PL spectra of HgSe/CdS had an interesting interband to intraband shift with respect to the local environment change, which will be discussed in section 1.3.1. The intraband PL of a HgSe/CdS film, which was peaked at 5 μm, improved ~3-fold compared with a similar thickness HgSe film.

In 2017, Zeger Hens and his co-workers developed a new HgSe/CdE (E=S or Se) synthesis based on colloidal atomic layer deposition (c-ALD).[59] c-ALD is a way to grow core/shell heterostructures layer-by-layer at room temperature. The cores that dissolved in nonpolar solvents are mixed with an immiscible polar solvent that contains a cation or anion precursor. Each half-cycle will coat the core with a full coverage of one cation or anion. In this case, the core is HgSe, the cation precursor is cadmium acetate in formamide and the anion precursor is $(NH_4)_2S$ or Na_2Se in formamide. Compared with hot-injection, c-ALD method can grow core/shell at room-temperature, which is a perfect fit for mercury chalcogenide CQDs to avoid aggregation and secondary nucleation. The authors used a small HgSe core of 4.3 nm diameter, which only showed interband absorption and PL ~1.8 μm, to grow CdSe or CdS shell. The PL QY of core/shells with different shell materials and thicknesses were measured.

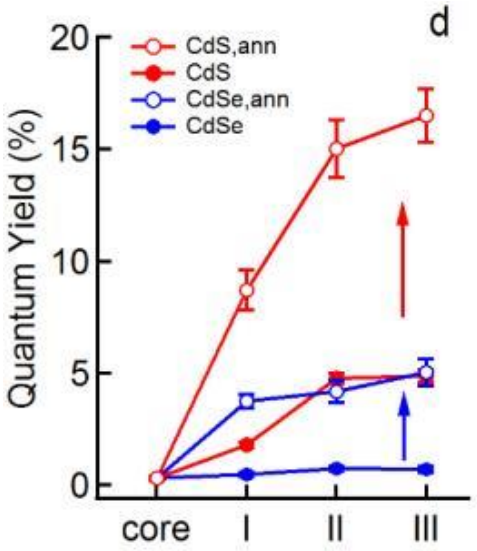

Figure 1-7 *Comparison of PL QY of HgSe/CdSe (blue) and HgSe/CdS (red) core/shells before (full markers) and after (open markers) annealing at 60 °C in solution under inert atmosphere. Adapted from reference 59.*

As shown in Figure 1-7, all core/shells had improved PL QY compared with HgSe cores, but the best result came from HgSe/3CdS with a solution annealing treatment, which had a QY of 16.5%. The large improvement in QY after annealing treatment is likely because of a reconstruction of the quantum dot lattice that removes some surface or interface traps. And the reason why CdSe, which is lattice matched with HgSe, behaved worse than CdS is probably that CdS is better in terms of confining holes in HgSe cores.

1.3 Properties of Mercury Chalcogenide CQDs and Core/Shells

1.3.1 Intraband Transition and Air-Stable n-Doping

Compared with bulk semiconductors, the intraband transition is unique to quantum dots (Figure 1-1). With proper doping, any CQD system can have intraband transition. Early works on this topic

usually used chemical or electrochemical doping methods to inject carriers into CQDs. In 2000, Moonsub Shim from Philippe Guyot-Sionnest's group observed the first steady state intraband absorption in charged CdSe CQDs.[60] In this work, a very reducing sodium diphenyl reagent was added to an inert gas sealed CdSe solution to n-dope the dot and its absorption spectrum was monitored before and after the reducing. As shown in Figure 1-8, a bleach of CdSe interband absorption ($1S_h$-$1S_e$) ~2 eV and an emergence of its intraband absorption ($1S_e$-$1P_e$) ~0.3 eV were clearly observed. The same behavior was also observed in other CQDs such as ZnO and CdS.

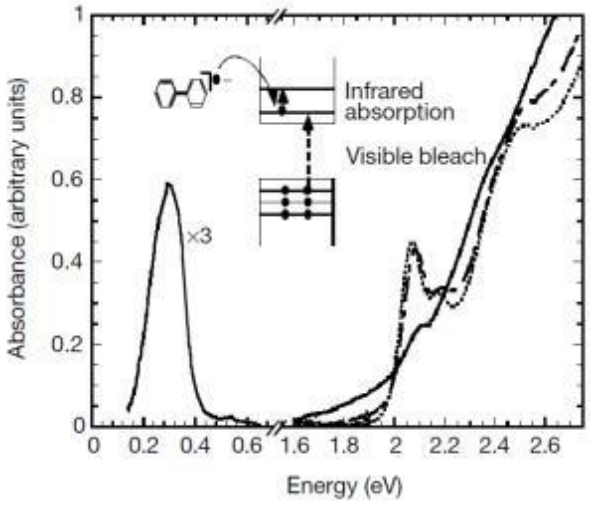

Figure 1-8 *Absorption spectrum of CdSe CQD solution before (dotted line), immediate after (solid line) and 27 hours after the addition of sodium diphenyl. Adapted from reference 60.*

The initial interband PL of CdSe was quenched after the biphenyl treatment. However, whether or not the dots had intraband PL was still unknown at that time because of the lack of emission measurement setup in the mid-IR.[61]

In 2003, Dong Yu and Congjun Wang from Philippe Guyot-Sionnest's group found that doing electrochemistry on CdSe CQD films could reversibly dope and undope the dots, which allowed a

more flexible and precise doping control compared with chemical doping.[62-63] These papers are of great importance, which are not only the first electrochemistry doping studies, but also the first ones to introduce solid state ligand exchange by replacing the original long-chain organic ligands with shorter ones, the latter becomes a standard treatment nowadays to improve the mobility of CQD films.

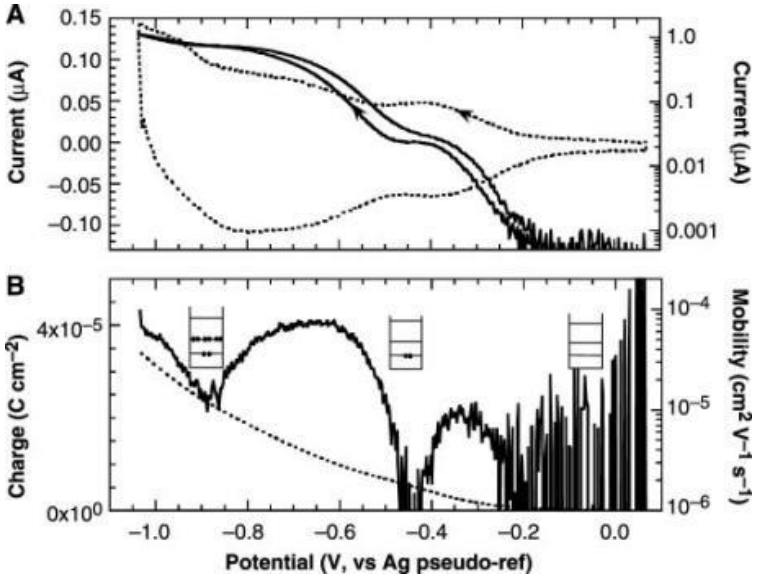

Figure 1-9 *(A) Electrochemistry current (dotted) and conduction current (solid) from cyclic voltammetry measurement of 1,7-heptanediamine exchanged CdSe film; (B) Integrated surface charge density (dotted) and differential mobility (solid). Adapted from reference 62.*

Figure 1-9A showed a typical result from cyclic voltammetry measurement. There were 2 waves of reduction current, which corresponded to the n-doping in CdSe $1S_e$ and $1P_e$ states. The integrated mobility had 2 clear rises and falls (Figure 1-9B), which indicated the dots were half-filled or fully-filled in their $1S_e$ or $1P_e$ states. The mobility improved 2 orders of magnitude after half-doped the $1P_e$ state.

Both chemical and electrochemical doping need to be done under inert gas atmosphere. The doping will disappear within minutes once exposed to air, which makes it hard to be used in real devices. As a result, air-stable n-doped CQDs become ideal materials to really use the intraband transitions. However, finding those materials is not an easy task, as it requires the ambient Fermi level to be above the $1S_e$ energy level of the CQDs. Giving the fact that the environmental Fermi level is usually between -0.1 and 0.1 V versus standard calomel electrode (SCE), most wide-gap semiconductors are not possible to have air-stable n-doping in their CQD forms.[64] As a result, until 2018, only four kinds of CQDs and their type-I core/shell heterostructures, namely HgS, HgSe, HgTe and Ag_2Se, have been reported to have air-stable intraband transitions and all of them are narrow gap semiconductor materials.[11, 15, 21, 65]

In 2014, Kwang et al. reported the first air-stable n-doped HgS CQDs.[11] The authors deployed a spectroelectrochemistry technique to monitor the change in absorption spectrum with respect to different electrochemical potentials. The results are shown in Figure 1-10.

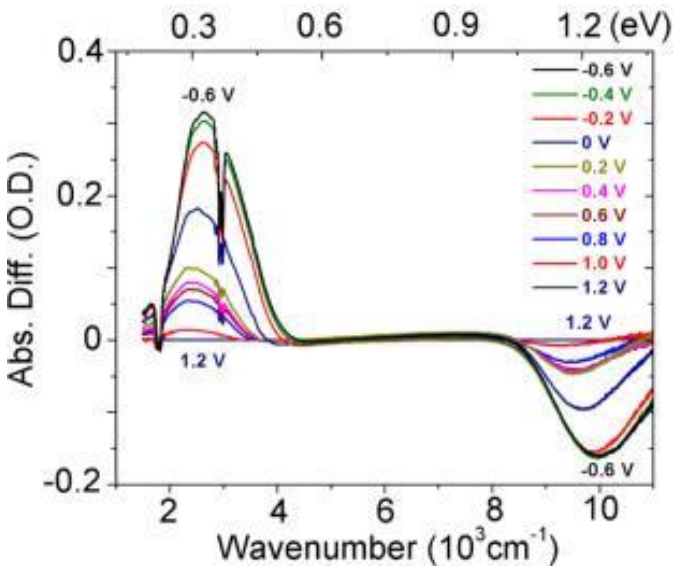

Figure 1-10 *Difference spectra of a HgS CQD film under increasingly negative potential vs Ag/AgCl. The spectrum at +1.2 V is used as the reference. Adapted from reference 11.*

When the applied potential moved to the negative side, which means more electrons were injected into the dots, the interband absorption ~10000 cm^{-1} got more and more bleached and the intraband peak ~2600 cm^{-1} became stronger. This correlation is a direct evidence that the mid-IR absorption is from the intraband transition. Similarly, intraband transition was also verified in HgSe CQDs.[15] Because of their small gaps, the intraband/interband can be tuned to favor one or the other by changing their local environment. Common methods include ligand exchange, shell growth and annealing. For example, exposing the surface of HgS CQDs to Hg^{2+} or S^{2-} would turn the intraband absorption on or off, which is shown in Figure 1-11.[11]

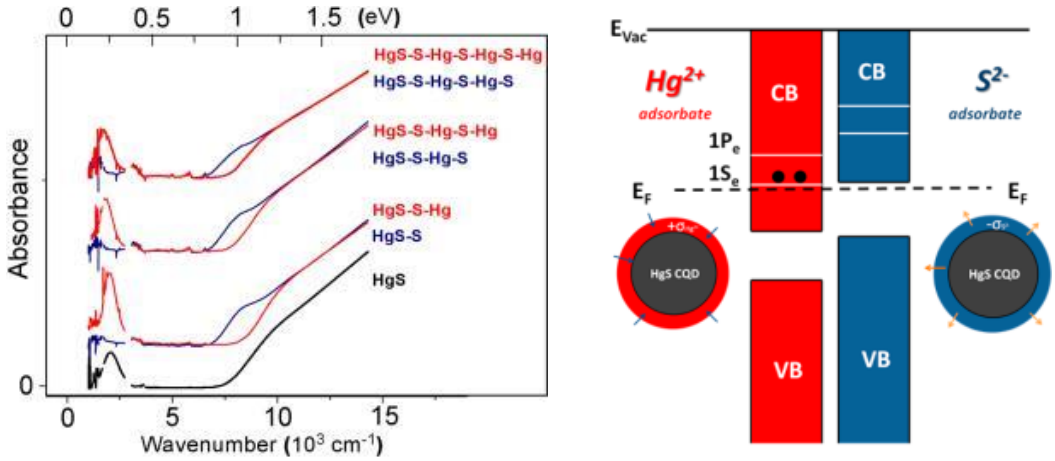

Figure 1-11 *(left) Absorption spectrum of HgS dots with alternating S^{2-} and Hg^{2+} layer-by-layer growth; (right) Schematic energy diagrams of Hg^{2+} and S^{2-}-treated HgS CQDs. Adapted from reference 11.*

A possible explanation is that Hg^{2+} and S^{2-} would introduce some surface dipoles (Figure 1-11). A dipole from Hg^{2+} would point inward from the surface ligand to the dot and S^{2-} the opposite. This surface gating effect would cause some energy level shift in order to stabilize the surface changes through electrostatic forces. This shift, usually ~0.1-0.3 eV, is enough to move the characteristic absorption back and forth between intraband and interband.

Growing a type-I core/shell heterostructure is a different story. Compared with HgSe, HgSe/CdS CQDs were less n-doped and their interband absorption and PL became dominant.[58] One interesting result was that when annealing or doing dithiol ligand exchange on the HgSe/CdS film, the intraband absorption and PL would reappear. A surface gating explanation may still apply here, as the metal thiolate formed by the dithiol treatment creates a dipole toward the core and therefore stabilizes the electron.

1.3.2 PL QY of Mercury Chalcogenide CQDs

PL QY is an important figure of merit for CQD applications such as LED and laser. It may also play a role in quantum dot-based photodetectors because it is an indicator of the number of recombination centers within the device. As a result, we usually want its value to be as close to 1 as possible. Near unity QY is readily available for quantum dots emitting in the visible range.[66] However, IR CQDs, especially in the mid- or long-IR, still have low PL QY.

Table 2 listed all mercury chalcogenide CQD syntheses and their PL QY. And Figure 1-12 showed some of the previously reported QY values of HgTe CQDs.[33, 67]

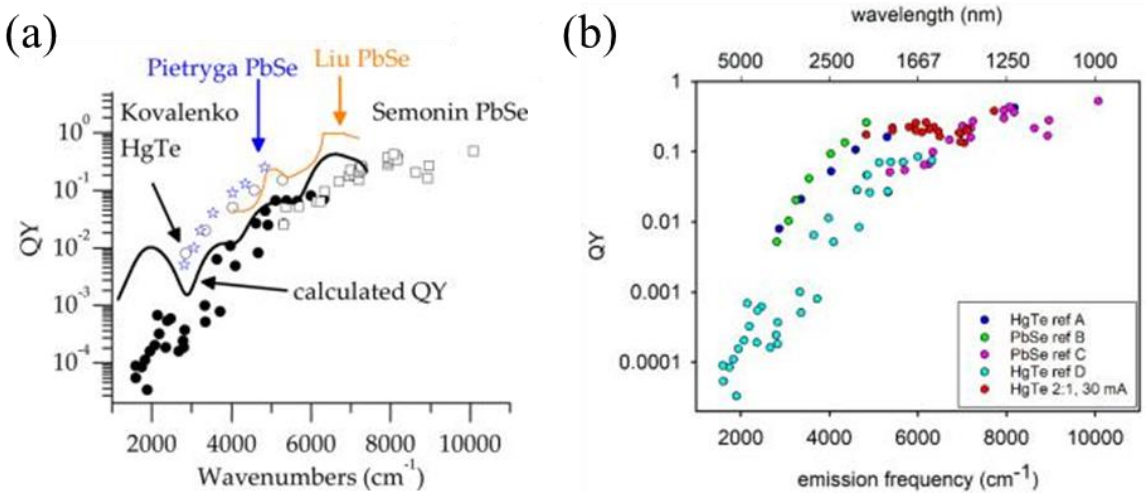

Figure 1-12 *PL QY of HgTe CQDs. Adapted from (a) reference 67 and (b) reference 33.*

In short-IR range (1.4-3 μm), the best HgTe CQDs have PL QY comparable to PbSe and PbS.[68-71] The QY decreases exponentially as the emission moves deeper into the infrared. At 5 μm, QY is on the order of 10^{-4}. The interband PL QY of HgSe is even lower, with published value ~0.003 at 1.8 μm.[59] No mid-IR intraband QY has been reported yet. The exact origin of the low QY in the infrared is still unknown. Surface traps, energy coupling to the ligand vibrational modes and

phonon related processes are some of the possible candidates, which will be discussed in depth in section 3.3.

Recently, Arjan Houtepen, Zeger Hens, Jonathan Owen and Ivan Infante published a computational study on CdSe nanocrystals and emphasized the importance of the 2-coordinated selenium atoms.[72] Those atoms, which are located on the surface unprotected Se sites, can create midgap states and act as carrier traps. Similar computational method has been used in HgTe quantum dots, where results showed that 2-coordinated tellurium atoms also generated midgap states. In practice, the authors suggested excess washing of CQDs may cause the loss of surface ligands and therefore unprotected chalcogenide sites.[73] A possible solution it to introduce Z-type ligands such as oleylammonium and $InCl_3$-OAm complex to passivate those trap states and PL QY of CdTe CQDs becomes close to 1 after such treatments.[74-76] However, because chalcogens are easily oxidized in air, the exact chemical environment of the surface chalcogenide sites in air is still unknown.

Chapter 2 Synthesis of HgTe CQDs and Core/Shells

In this chapter, the synthesis of non-aggregated HgTe CQDs will be discussed, both in amine and in oleic acid. The non-aggregated nature of these dots makes it possible to grow core/shell heterostructures for the first time, as the result from HgTe/CdTe core/shell will show. Other interesting properties such as air-stable n-doping, shape control and phase control will also be discussed. This chapter includes the published results from references 65 and 77 as well as some unpublished data.

2.1 Instrumentations

Without further specification, the same absorption, PL, electrochemistry and other material characterization techniques are used for all CQD studies in the thesis.

Transmittance electron microscopy (TEM) images were obtained using a FEI Tecnai F30 microscope at 300 kV.

X-ray diffraction (XRD) spectra were taken with a Bruker D8 powder diffractometer.

X-ray photoelectron spectroscopy (XPS) results were obtained using Kratos Axis Nova XPS system.

Solution absorption spectra were taken with an Agilent Cary 5000 UV-Vis-NIR spectrometer and a Nicolet Magna-IR 550 spectrometer.

Film absorption spectra were measured in an attenuated total reflection (ATR) mode. Films were fabricated by drop-casting CQD solutions on a 45°-cut ZnSe window, which were then loaded on a Nicolet Magna-IR 550 spectrometer to measure their ATR-IR.

PL spectra were recorded with an 808 nm laser diode modulated at 90 kHz with an average power of 150 mW over a 1 mm^2 area. The PL was collected by an off-axis (60°) parabolic gold mirror of 25 mm diameter and 50 cm effective focal length. The PL was then sent through a home-built step-scan Michelson interferometer and detected by an MCT detector with a lock-in amplifier.

The PL quantum yield values shown in this thesis were determined separately by measuring the QY for a film of HgSe/CdSe CQD which exhibited relatively bright interband emission at 2.5 microns. Then, the absolute QY of the interband PL was determined with a gold integrating sphere and a PbSe photodetector. Using a thermopile, we verified than the signal from the PbSe detector was linear with photon energy within 15% for low intensity light from 2.5 μm to 808 nm. A silicon window in front of the detector of transmission, T_{Si} = 60%, was used to block the 808 nm and to measure the PL intensity, *PL*. The Si window was then removed to measure the 808 nm intensity, I_{sample}, with the sample and without the sample, $I_{no\ sample}$, in the sphere. The QY for the interband emission was then calculated using equation 1, which is appropriate for low PL efficiency.

$$QY = \frac{PL/T_{Si}}{(I_{no\ sample} - I_{sample})} \times \frac{\tilde{\nu}}{\tilde{\nu}_{808}} \qquad (1)$$

The quantum yield for intraband emission and for all other samples are then obtained by their relative signals to that sample, given the fact that all samples had similar absorption (>80%) at 808 nm.

Electrochemistry measurement was done following the procedures below:

a. Prepared CQD films on interdigitated electrodes by drop-casting;
b. The prepared film was submerged in 2% ethanedithiol (EDT) and 2% HCl in isopropanol for 30 second and then rinsed with isopropanol. This ligand exchange step will replace the long-chain ligand with shorter dithiol ligand and increase the conductivity of the film;

c. Electrochemistry was done using a four-electrode setup: two working electrodes, one reference electrode, and one Pt counter electrode. During the measurement, a bipotentiostat (DY2300 series Digi-Ivy) applied a small bias (5 mV) between the two working electrodes and measured the currents on the two working electrodes (I_1, I_2) as a function of potential. ($I_1 + I_2$) is the Faradaic current of the film and ($I_1 - I_2$)/2 is the conduction current. The electrolyte was 0.1 M tetrabutylammonium perchlorate in propylene carbonate, under nitrogen bubbling, but no precaution was taken to guarantee an anhydrous electrolyte. As a result, the measurement was done in an ethanol/dry ice bath at 203 K to minimize the Faradaic currents due to reaction of water and other impurities.

2.2 Non-Aggregated HgTe CQDs Synthesized in Oleylamine

2.2.1 Synthesis Procedures

The detailed procedures are shown below:

a. Oleylamine (OAm) (Sigma-Aldrich, 70%) was purified by degassing it using a Schlenk line setup under vacuum at 135 °C for 3 h. It was then cooled down under argon and stored in glovebox for future use. The purpose of this step is to remove the absorbed CO_2 and H_2O in OAm;
b. Weighed a certain amount of $HgCl_2$ powder (Sigma-Aldrich, 99.5%) along with 4 mL purified OAm in a 3-neck flask. Under the Schlenk line, degassing it at room temperature for 20 min, then degassing at 100 °C for another 1 h. The solution was clear, which means the $HgCl_2$ powder was fully dissolved. This step is to prepare Hg precursor;
c. Flushed the system with argon and kept the Hg precursor under argon for 20 min;
d. Reset the temperature at the desired reaction temperature;

e. In glovebox, prepared the Te precursor by dissolving a certain amount of bis(trimethylsilyl)telluride ($(TMS)_2Te$, Fisher, 98%) in 0.5 mL of hexane. The Te precursor solution was then loaded in a 1 mL syringe and quickly injected into the Hg precursor;

f. Extracted all reaction mixtures with a long needle syringe when the reaction was finished and quenched it in pure tetrachloroethylene (TCE);

g. Precipitated the dots by adding a mixture of acetone and methanol until the solution became turbid. After centrifugation, black precipitate was collected. Washed the precipitate with ethanol for 3 times to remove excess ligands. The dots were re-dispersed in TCE.

In this synthesis, amount of $HgCl_2$, amount of $(TMS)_2Te$, reaction temperature and reaction time were the 4 parameters to control the size of HgTe CQDs. Table 2-1 lists the average sizes (in diameter) of HgTe CQDs with their corresponding reaction conditions.

Table 2-1 HgTe CQDs sizes and synthetic parameters

HgTe CQD size (nm)	Reaction temperature (°C)	Reaction time (min)	Amount of $HgCl_2$ (mmol)	Amount of $(TMS)_2Te$ (mmol)
4.8	100	1	0.1	0.05
5.9	100	1	0.2	0.1
7.1	100	1	0.4	0.2
8.0	120	1	0.1	0.05
9.6	120	10	0.1	0.05
11.5	120	10	0.2	0.05

2.2.2 Comparison between Aggregated and Non-Aggregated HgTe CQD Synthesis

As shown in section 1.2.1, the reaction between mercury(II) salts and trioctylphosphine telluride (TOPTe) in long-chain amine solvents produces HgTe CQDs with a good size-tunability in the mid-infrared, as well as detectable and narrow photoluminescence (PL) peaks.[36] However, the synthesized HgTe CQDs have aggregated morphology and poor surface stability, which leads to two problems. First, HgTe CQDs easily crash from solution overtime; second, in order to stabilize the colloid, one has to use strong ligands such as thiols. The thiols effectively passivate the surface Hg sites, but also make further surface modifications almost impossible. This has seriously impeded the efforts to proceed with ligand exchange, core/shell growth, and tunable doping by surface modifications, which are essential to improve device performance. There was, therefore, a definite need for a new synthesis that provides improved morphology, colloidal stability, while also opening up new possibilities for surface modifications.

In the reaction between TOPTe and mercury(II) chloride salts, the ligands that bind to surface Hg sites are alkyl amine/ammonium, TOP, and likely chloride ions as in the case of lead chalcogenides CQDs.[71] During the cleaning process, which involves precipitation with a polar solvent and re-dispersion in a non-polar solvent, the colloidal stability is typically lost due to the dilution of the ligands. This was previously mitigated by adding more TOP and the stronger-binding DDT to the solution right after reaction.[36] It is expected that the thiol replaces the alkyl amine and chloride. As for the Te sites, there have been reports that TOP can act as the surface Se capping ligand in CdSe CQDs, which suggests that TOP may also bind to Te sites.[78-81] However, the bulky TOP ligand should be rather weak because of steric hindrance in particular on the well-developed facets of these HgTe CQDs.[82] This could lead to the poor passivation of the Te sites and may explain the

moderate long term stability of even the thiol capped colloids. The oxidation from TOP to TOPO may cause even faster stability loss in air. The difficulties with HgTe are in striking contrast to the case of HgS and HgSe CQDs, which have much better stability and good processability without a thiol treatment, and are also rather spherical.[11, 15] The main difference in the synthesis of HgS and HgSe is the use of more reactive sources of sulfide and selenide than the complexes of TOPSe or TOPS.

We therefore explored more reactive sources of tellurium including NaHTe, H_2Te generated from Al_2Te_3, bis(trimethylsilyl)telluride ($(TMS)_2Te$), and tributylphosphine telluride (TBPTe). Our best results have been obtained with $(TMS)_2Te$. The use of $(TMS)_2Te$ has two advantages. First, $(TMS)_2Te$ greatly simplifies the reaction system. There is no TOP or TOPO (TOP being oxidized) that could act like surface ligands, and trimethylsilyl- is a good leaving group which cannot act as a ligand. Second, $(TMS)_2Te$ has a very high reactivity such that it will react quantitatively with Hg precursor. In contrast, TOP forms a complex with Hg, which limits the yield of HgTe.

The detailed synthetic procedures were shown in section 2.2.1. The final HgTe CQDs size is determined by the reaction temperature, reaction time and amount of precursors. During the cleaning process, thiol is not needed, unlike the synthesis using TOPTe. Figure 2-1 shows the TEM images of a size series of HgTe CQDs and XRD spectrum. These pictures indicate a much-improved dispersion of the colloids compared to the TOPTe method, all the more remarkable in the absence of thiols. These dots can be stored in the cleaned solution for months without any precipitate. The dots are still β-HgTe (zin-blende).

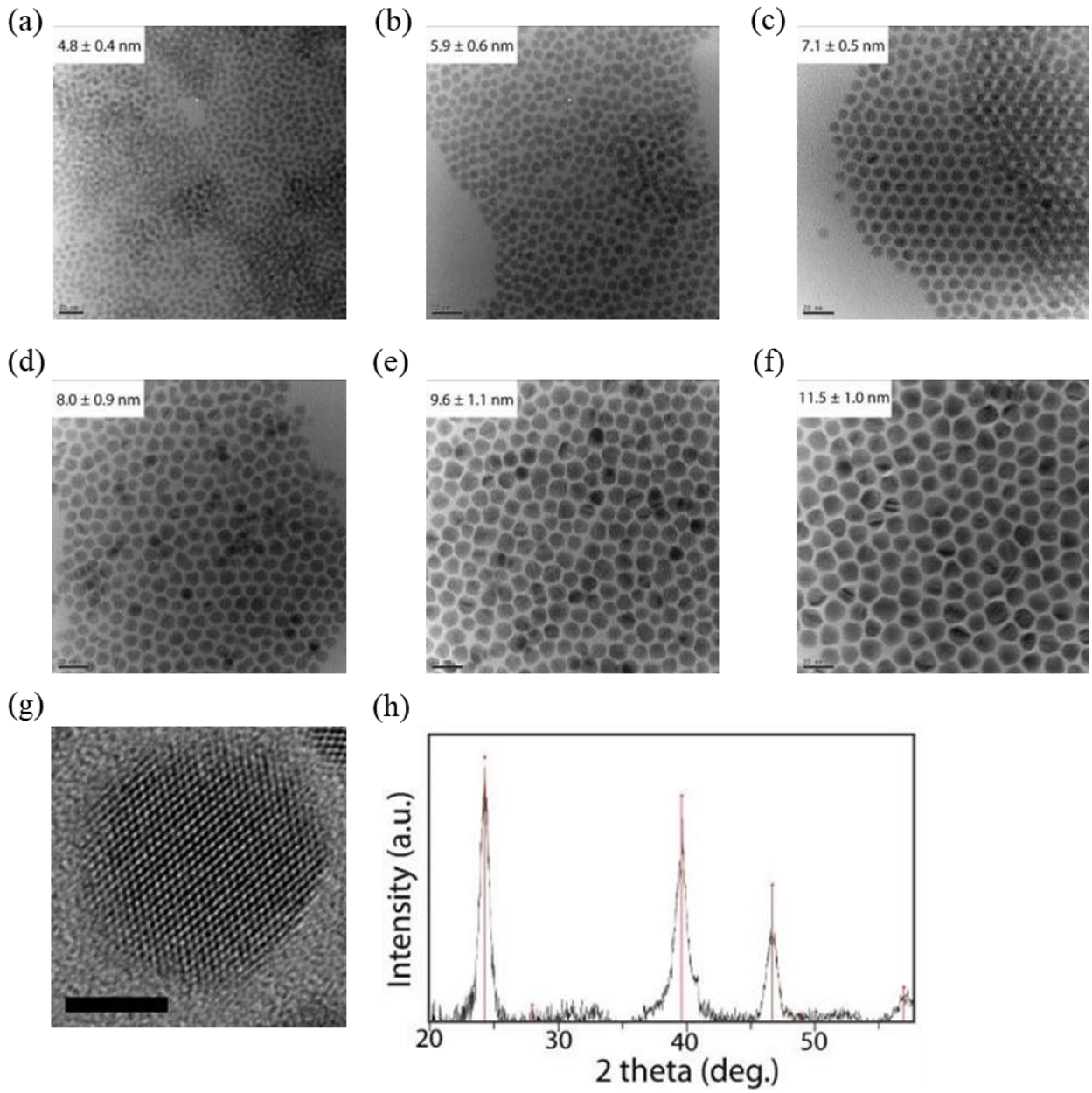

Figure 2-1 *(a-f) TEM images of $(TMS)_2Te$ synthesized HgTe CQDs with diameter ranging from 4.8 to 11.5 nm (scale bar: 20 nm); (g) High resolution TEM (scale bar: 5 nm) and (h) XRD spectrum of HgTe CQDs with 11.5 nm size (red line: standard zinc-blende HgTe peaks).*

Figure 2-1 also shows that the CQDs are rather spherical, in contrast to the strongly facetted TOPTe synthesized HgTe dots.[36] Faceting generally arises when growth is slow such that the

slowest growing facets dominate the final structures. It is possible that the fast growth due to the high reactivity of $(TMS)_2Te$ is the reason why faceting is strongly reduced compared to the synthesis using TOPTe.

Besides the reduced faceting which limits oriented attachment when ligands are starved, we propose that another reason behind the colloidal stability is excess mercury precursor.[83] For all samples shown in Figure 2-1, there is at least a 2-fold excess of Hg precursor. At high temperatures, the $HgCl_2$ salt is dissolved in OAm, forming a clear solution where the Hg precursor likely exists in the form of $HgCl_2(OAm)_n$ complex. After the quantitative reaction between the Hg precursor and $(TMS)_2Te$, we propose that the excess Hg precursor acts as ligands that bind to the surface Te sites. To test the role of excess Hg, the ratio between $HgCl_2$ and $(TMS)_2Te$ precursor has been varied and the best results were always with excess Hg. For example, Figure 2-2 shows the TEM images of a sample with Hg:Te = 1:1 and another sample with Hg:Te = 2:1, other reaction parameters being the same.

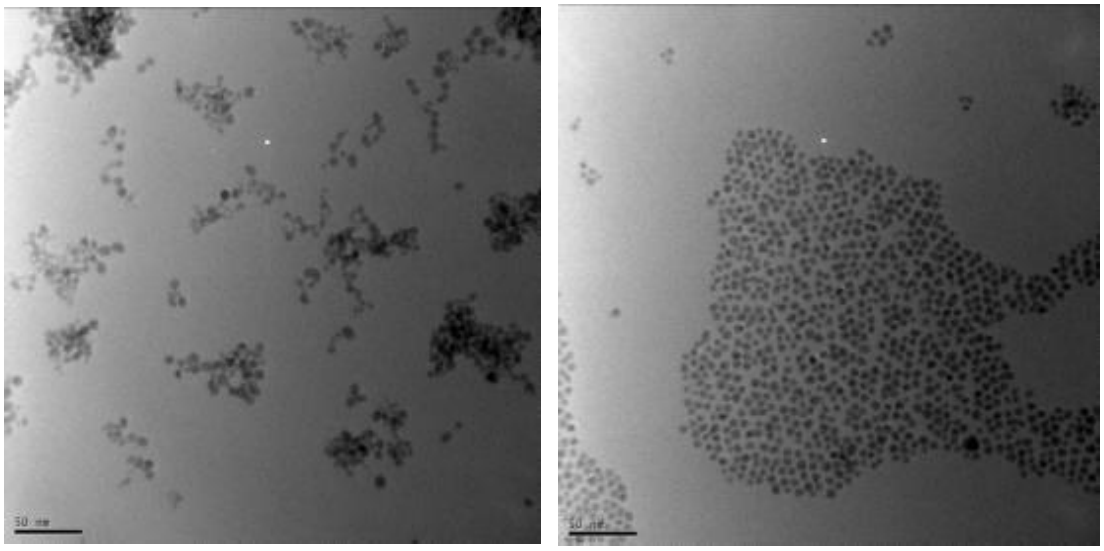

Figure 2-2 *(Left) HgTe CQDs with $HgCl_2$: $(TMS)_2Te$ = 1:1; (Right) HgTe CQDs with $HgCl_2$: $(TMS)_2Te$ = 2:1.*

Figure 2-2 shows that the particles have attained similar sizes, but their colloidal stabilities are markedly different. In the cleaning step, the 1:1 sample could only be re-dispersed by adding excess thiol ligands and still crashed out quickly. Furthermore, it is apparent in Figure 2-2 that these HgTe CQDs are already subject to some aggregation, even with thiols. In comparison, the 2:1 sample can be cleaned and re-dispersed while remaining well-separated on the TEM images, without thiols. Therefore, the excess Hg precursor, while not modifying significantly the nanocrystal growth, acts as surface ligands in a crucial way to help stabilizing the HgTe CQDs.

Table 2-2 XPS results of different HgTe CQDs films

HgTe CQD	Peak	Binding Energy (eV)	Raw area (cps eV)	Atomic concentration (%)	Hg:Te atomic ratio
11.5 nm $(TMS)_2Te$	Te 3d	572.000	375994.6	21.96	1.52:1
	Hg 4f	99.000	488629.0	33.27	
8.0 nm $(TMS)_2Te$	Te 3d	572.000	243752.5	22.92	1.39:1
	Hg 4f	100.000	290312.8	31.86	
8.0 nm TOPTe	Te 3d	572.000	891556.9	24.81	1.15:1
	Hg 4f	100.000	884086.8	28.72	

The elementary analysis results using XPS are shown in Table 2-2 and clearly demonstrates the Hg rich surface with a Hg:Te ratio of 1.4−1.5. We also tested whether a similar excess Hg precursor method would facilitate the dispersion of HgTe CQDs synthesized with TOPTe. However, we found that adding excess Hg precursor during or after the reaction cannot prevent aggregation and

that the Hg:Te ratio is significantly smaller at ~1.15. Therefore, we propose that the improved dispersion of the HgTe CQDs using $(TMS)_2Te$ results from both the more spherical shape, which makes them less prone to oriented attachment, and the excess Hg ligands.

2.2.3 Properties of Non-Aggregated HgTe CQDs

In this section, the results from optical and electrochemistry measurements are shown. The non-aggregated HgTe CQDs have a very interesting air-stable n-doping, which makes it the third system behind HgS and HgSe that has this property.

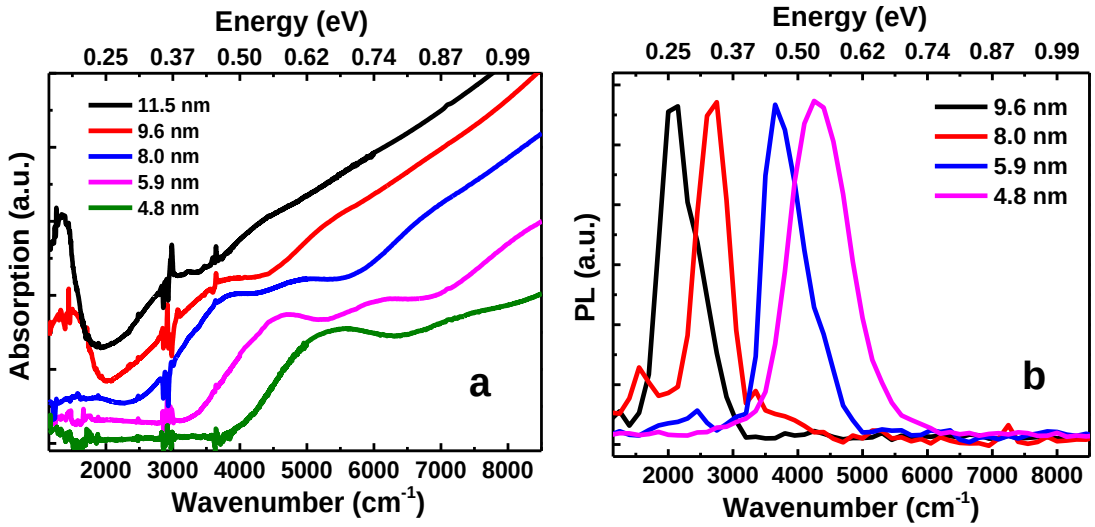

Figure 2-3 *(a) Absorption spectra of HgTe CQDs solution in TCE; (b) Normalized PL spectra of the same HgTe CQDs films after thiol ligand exchange.*

Figure 2-3 shows the absorption and PL spectra of HgTe CQDs with different sizes. It exhibits a monotonic trend in absorption and PL peaks with respect to particle sizes. More importantly, in Figure 2-3a, the absorption spectra of 11.5 nm and 9.6 nm CQDs show a clear intraband absorption around 1350 cm^{-1} and 1500 cm^{-1}, respectively, which corresponds to the transition between the

quantum dot $1S_e$ and $1P_e$ states. Therefore, this indicates the air-stable n-doping in HgTe CQDs, which is further confirmed by electrochemistry experiments, as shown in Figure 2-4.

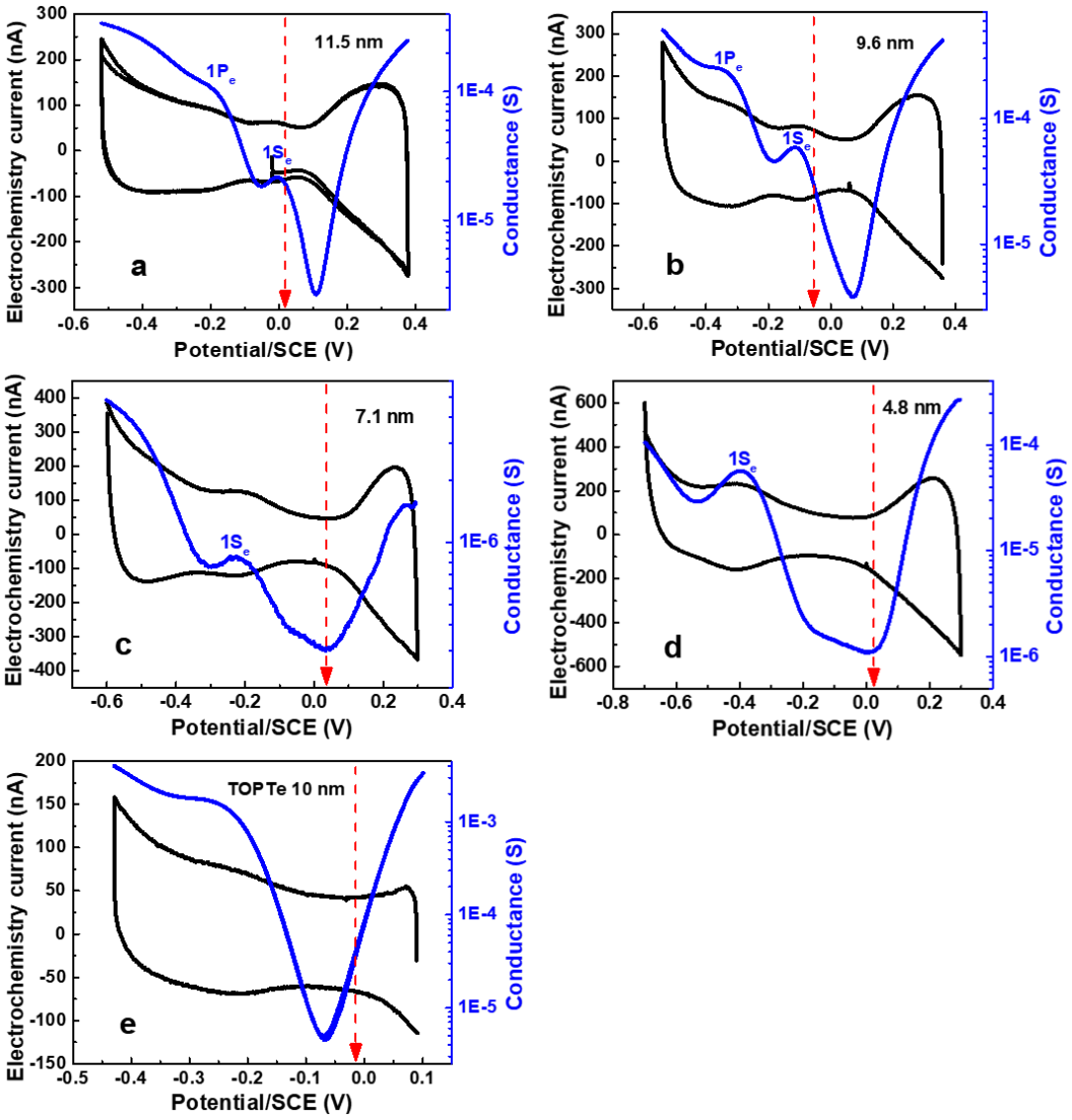

Figure 2-4 *Cyclic voltammetry results of (a) 11.5 nm; (b) 9.6 nm; (c) 7.1 nm; (d) 4.8 nm; (e) ~10 nm HgTe CQD films. Films (a-d) used $(TMS)_2Te$ synthesized HgTe and film (e) used TOPTe. The black and blue curves are the electrochemistry current and conductance of the film, respectively. The red dashed arrow is the position of the rest potential. The reference electrode is saturated calomel electrode.*

Figure 2-4b shows the cyclic voltammetry with two clear electrochemical waves corresponding to the $1S_e$ and $1P_e$ states. This is compared to the same experiment in Figure 2-4e with similar size HgTe synthesized with TOPTe, where only the $1S_e$ state appears, and only as a shoulder.[64, 84] The position of the environmental Fermi level (rest potential) with respect to the $1S_e$ state also clearly confirms the n-doping for the $(TMS)_2Te$ synthesized dots, since it is within the $1S_e$ state wave. In contrast, and in agreement with prior results, the Fermi level is slightly closer to the hole injection for the TOPTe synthesized dots, which are therefore slightly p-doped.

From Figure 2-4(a-b), the n-doping is estimated at 1 e^-/dot and 0.5 e^-/dot, respectively, assuming that the peak of the $1S_e$ charging wave is at 1 e^-/dot. For smaller particles (Figure 2-4(c-d)), the $1S_e$ peaks move more negative, so that the n-doping disappears, in accord with the absence of the intraband absorption in Figure 2-3.

A recent study compared the electron mobility of films of HgTe dots synthesized with TOPTe with films of HgS and HgSe dots, using a same dithiol ligand exchange.[64] It showed two orders of magnitude higher mobility for TOPTe synthesized HgTe CQDs. This large difference in conductance was assigned to the partial aggregation of the HgTe CQDs, even though XRD cannot clearly identify significant narrowing. This conjecture is verified in Figure 2-4, which shows that the films of the non-aggregating HgTe dots made with $(TMS)_2Te$ have much lower conductance compared with the partially aggregated HgTe dots made with TOPTe. This result therefore supports the notion that partial aggregation enhances the mobility in CQD films.

Combining the electrochemistry and optical spectra, we derived the state energies for HgTe CQDs synthesized using $(TMS)_2Te$ and compared the values with TOPTe synthesized ones. The results are shown in Figure 2-5.

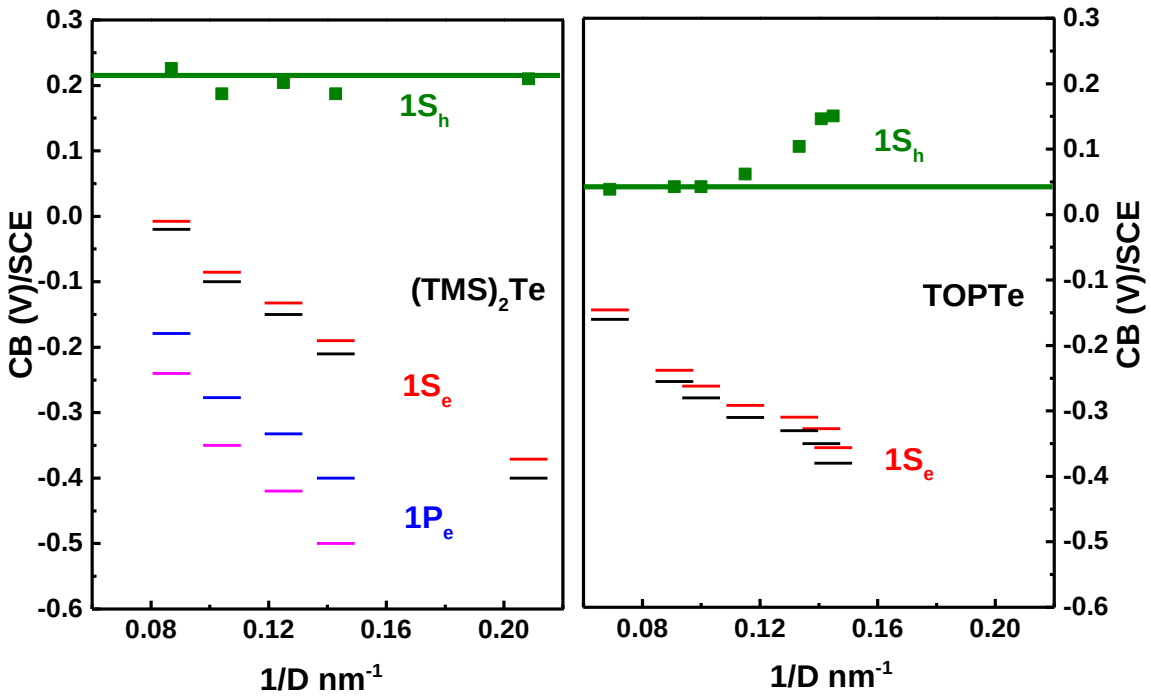

Figure 2-5 *State energies of HgTe synthesized using (left) $(TMS)_2Te$ and (right) TOPTe versus size. The black and magenta dashes are $1S_e$ and $1P_e$ states derived from electrochemistry, respectively. The red and blue dashes are $1S_e$ and $1P_e$ states corrected by the charging energy.*[64] *The green dots are the estimated conduction band minimum using the optical interband absorption. The right plot of TOPTe synthesized HgTe is adapted from reference 64.*

Figure 2-5 shows that the HgTe CQDs synthesized with $(TMS)_2Te$ are about 0.15 V more positive than previously reported data for TOPTe.[64] This difference, although small, is sufficient to bring the $1S_e$ state of the larger dots in the range of the ambient Fermi level (usually between -0.05 and

0.05 V versus SCE) and induce n-doping. We note that the valence band positions for HgS, HgSe and HgTe were recently reported at -5.85, -5.50, and -4.77 eV.[64] The new synthesis shifts the band position of HgTe to -4.92 eV by producing more spherical and well-separated HgTe dots, which are likely to have similar surface passivation as the prior HgSe and HgS CQDs.[11, 15, 85] The new HgTe valence band and its relative position with HgSe and HgS are in better agreement with theory.[86]

As discussed in section 1.3.1, the state energies are influenced by surface dipoles.[11] When surface dipoles are pointing towards the dot, state energies are lowered, and the states become occupied if they lie below the environment Fermi level. The Hg^{2+}-ligands is likely acting as a surface dipole pointing towards the dot. Therefore, the Hg rich surface created by the new synthesis explains the shifts of the $1S_e$ state towards the positive direction, which facilitates n-doping.

To summarize section 2.2, we developed a new synthetic method for HgTe CQDs using a more reactive source of tellurium $(TMS)_2Te$ and an excess of mercury precursor. This leads to HgTe CQDs that are more spherical with no longer a tendency to aggregate. An important result is that the particles are stably dispersed in the absence of thiols. This is significant since the surface is now accessible for surface chemical modifications using chemicals less strongly bound than sulfides. This new synthesis will therefore allow for the further investigation of ligand exchange and core/shells in order to improve device performance. Another important result is that the HgTe dots show air-stable n-doping for the larger sizes. Electrochemistry verifies that there is a 0.15 eV shift of the band energy, which induces n-doping.

2.3 Non-Aggregated HgTe CQDs synthesized in Oleic Acid

2.3.1 Synthesis Procedures

The detailed procedures are shown below:

a. Weighed 10 mmol of tellurium granules (Sigma-Aldrich, 99.999%, pellets) in a 20 mL vial. Added 10 mL of trioctylphosphine (TOP, Sigma-Aldrich, 90%) and took the vial to glovebox. Stirred overnight at room temperature to let the solid dissolved and a yellow-green solution was prepared. This step is to prepare 1 M TOPTe;

b. Weighed 1 mmol of HgO powder (Sigma-Aldrich, 99%) in a 20 mL glass vial. Added 6 mL of oleic acid (OAcid, Sigma-Aldrich, 90%) and 4 mL of octadecene (ODE, Sigma-Aldrich, 90%). Put the vial on a hot plate inside the glovebox;

c. Set the hot plate temperatures at 125 °C and started stirring. When the actual temperature reached 110 °C, the red color from HgO powder gradually disappeared. It took about 15 min for the solution becoming colorless, then stopped heating. This step is to prepare mercury oleate ($Hg(oleate)_2$) as mercury precursor;

d. When the solution was cooled to room temperature (~24 °C), injected 0.1 mL of 1 M TOPTe. The color turned red then black within 5 s;

e. Took 1 mL aliquots of reaction mixture each time after a certain reaction duration at a certain temperature. A list of reaction temperature, reaction time and the corresponding PL peak position (indicating particle size) was shown in Table 2-3. Note that it was a continuous reaction, which means a row went through all the steps above it. The dots were precipitated by adding a mixture of acetone and ethanol. After centrifugation, the solids were re-dispersed in TCE with the help of sonication.

Table 2-3 Synthetic parameters for oleic acid synthesized HgTe CQDs

Sample number	Reaction time (h)	Reaction temperature (°C)	Film PL position (cm^{-1})
a	1.5	24	8200
b	15	24	7950
c	20	24	6550
d	2	35	6200
e	3	35	6000
f	16	45	4750
g	16	60	3550
h	16	70	2650*

* Measured after EDT/HCl ligand exchange, others measured as-prepared.

2.3.2 Surface Ligands of Different HgTe CQD Syntheses

Researchers have classified CQD binding ligands into 3 categories: Z-type, L-type and X-type ligands, where one ligand can accept 2 electrons (donate 1 orbital), donate 2 electrons and donate 1 electron, respectively, to form chemical bond with the quantum dot surface cations and anions.[87-88] Their differences are shown in Figure 2-6.

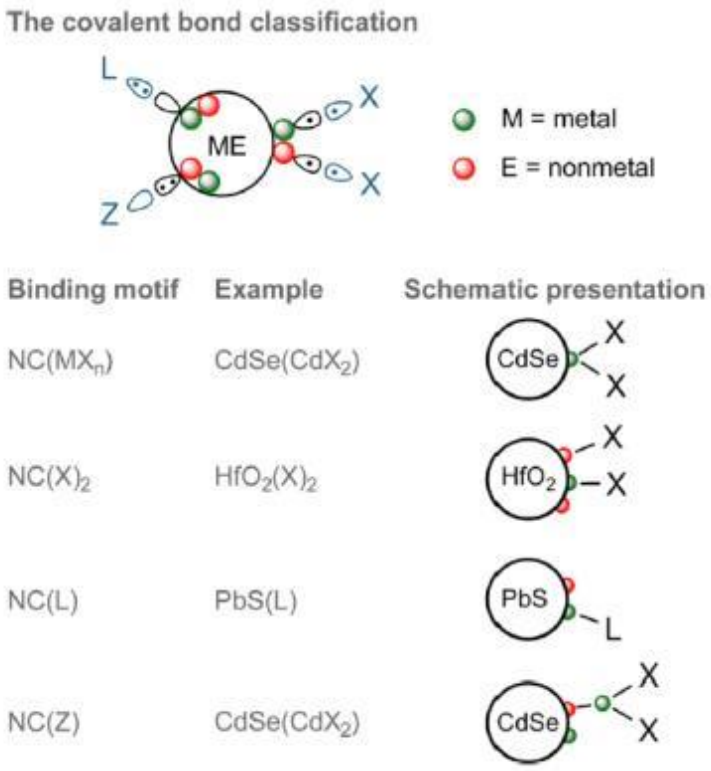

Figure 2-6 *Schematic representations of the most important ligand classes within the covalent bond classification regime. Adapted from reference 88.*

Based on this classification, an L-type ligand prefers to bind to metal sites on the quantum dot surface while a Z-type ligand tends to bind to nonmetal sites. An X-type ligand can choose to bind to either metal or nonmetal sites, but in practice, most X-type ligands are bound to metal sites, such as thiols. Specifically, for HgTe CQDs, the binding ligands of different HgTe CQD syntheses are shown in Table 2-4.

Table 2-4 Binding ligands on HgTe CQD surfaces

Synthesis	Hg sites binding ligands	Te sites binding ligands
TOPTe, OAm[36]	OAm (L-type), DDT (X-type)	TOP (L-type, weak)*
$(TMS)_2Te$, OAm (section 2.2)	OAm (L-type)	$HgCl_2(OAm)_x$ (Z-type)
TOPTe, OAcid (section 2.3)	oleate (X-type)	$Hg(oleate)_2$ (Z-type)

* TOP is a weak Te binding ligand and quickly oxidized to TOPO in air.

From Table 2-4, it is clear that the old synthesis from Hg-amine and TOPTe lacks Te sites binding ligands. As a result, it requires a very strong thiol to be the Hg-site ligand.[36] For the other two syntheses, because the Te sites are also protected, the dots can be stable without thiols. Another result from the existence of Z-type ligand is the higher Hg/Te ratio, which is verified by XPS. Metal/nonmetal ratio greater than 1 seems to be a general law in other CQD systems such as CdSe, PbSe and PbS, where Z-type ligand is believed to be present.[89-95]

The presence of underpassivated surface chalcogen sites may create mid-gap states that act as electron traps. Introducing additional Z-type ligands such as $CdCl_2$ has proved to be effective in passivating these trap states and improving the PL efficiency.[76] However, things may be different for quantum dots stored in air, as the unpassivated Te will be quickly oxidized to $TeO_x(OH)_y$, which is transparent in the IR and may be acting as an inorganic matrix.

2.3.3 Properties of HgTe CQDs Synthesized in Oleic Acid

Since Xiaogang Peng's work in 2001, metal precursors produced by the reaction between metal oxides and organic acids became an important group of precursors, which greatly lowered the

threshold of nanocrystal synthesis.[96] The commonly used organic acids are fatty acids such as oleic acid and phosphonic acids such as tetradecylphosphonic acid.[97-98] Depending on the desired capping ligands, metal-acid complexes can be used directly in a one-pot synthesis or separated by adding acetone and redissolved in other solvent/ligand systems.[99-100] In this HgTe CQD synthesis, $Hg(oleate)_2$ was made in-situ and OAcid acted as both solvent and ligand, similar to the role of OAm in section 2.2.

In a typical OAcid-based HgTe synthesis, the Hg:Te precursor ratio is 10:1. As suggested in section 2.3.2, to produce a metal-rich surface usually acquires a high metal/nonmetal precursor ratio, sometimes as high as 24:1.[101] And for these HgTe CQDs, any precursor ratio smaller than 5:1 will not allow the dots to be stable in TCE after cleaning. Figure 2-7 shows the TEM images of HgTe CQDs with a series of sizes.

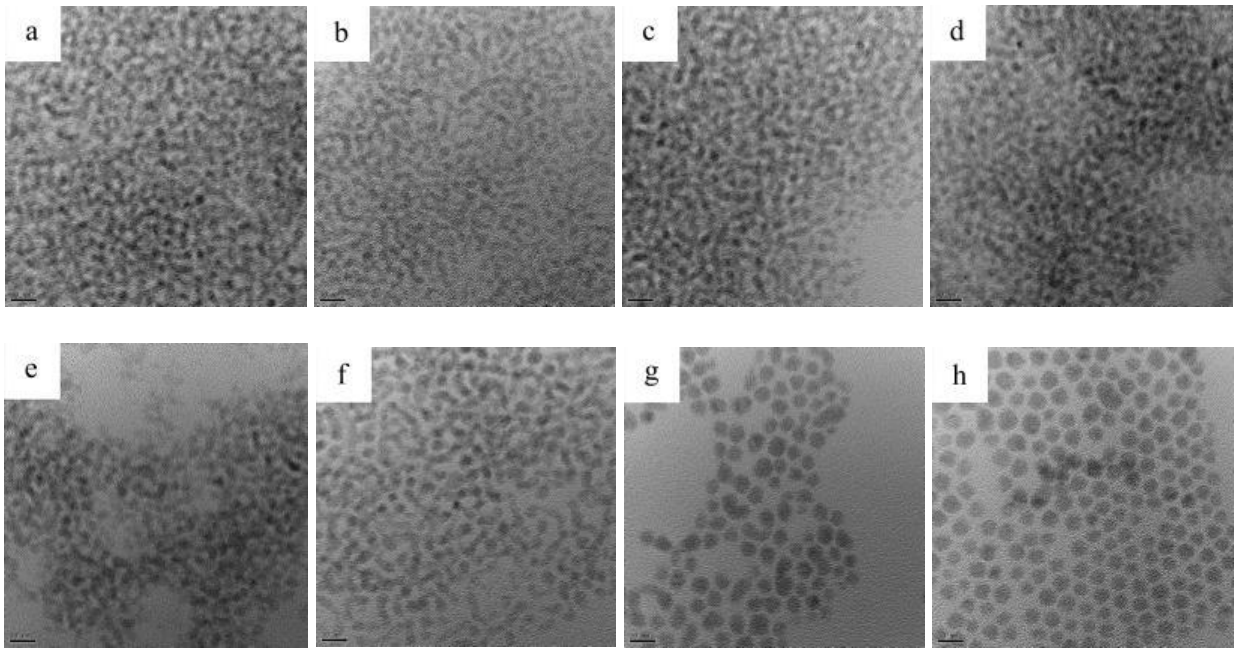

Figure 2-7 *TEM images of HgTe CQDs synthesized in oleic acid (scale bar: 10 nm). (a-h) correspond to the sample numbers in Table 2-3.*

Even with Hg:Te = 10:1, aggregation is still a problem in these HgTe CQDs, especially for small ones. As a result, smaller dots such as 2-7a will precipitate out in TCE within hours and bigger ones can last for weeks in the absence of thiols. The aggregation is likely due to oriental attachment, as shown by the elongated and knotted particle chains in Figure 2-7b and 2-7f. When the particle size increases, the dots become more and more separated and spherical and their solution stability improves.

Figure 2-8a shows the normalized PL spectra of HgTe CQDs with different sizes. The HgTe CQD samples were drop-casted on aluminum substrates and measured as-prepared. All samples, except h, exhibit a narrow PL peak, with FWHM between 600 and 1000 cm^{-1}. The broad PL from sample h is likely due to the energy transfer from dots to the C-H vibrational modes from ligands, which bleaches the PL ~2900-3000 cm^{-1} and creates a dip in the PL peak. Therefore, a solid-state ligand exchange with EDT/HCl will help cleaning the C-H stretch. The results are shown in Figure 2-8(b-c).

After EDT/HCl ligand exchange, more than 90% of C-H stretches as well as most of the low energy vibrations from 1000 cm^{-1} to 2000 cm^{-1} (from C=O) are removed and a more Gaussian PL peak is obtained. The PL is much stronger (increased an order of magnitude in intensity) after the removal of surface ligands. It also red-shifts, likely due to the slight sintering with shorter ligands. No intraband absorption or PL is observed and electrochemistry also confirms that the environmental Fermi level is below the $1S_e$ state of HgTe CQDs.

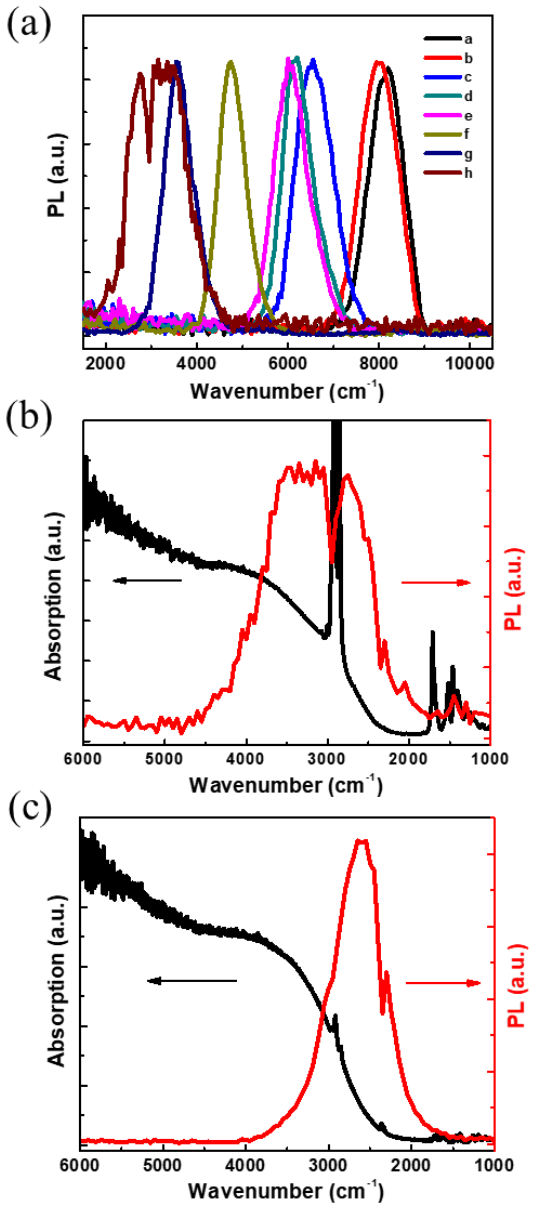

Figure 2-8 *(a) Normalized PL spectrum of films of sample (a-h) from Table 2-3. Measured on Al substrate; (b-c) Absorption and PL spectrum of a film of sample h (middle) before and (bottom) after EDT/HCl treatment. Measured on ZnSe substrate.*

An interesting observation is that the absorptions from non-aggregated HgTe CQDs, either synthesized in OAm or in OAcid, have broader excitonic features than aggregated ones (shown in Figure 1-4, 2-3 and 2-8, respectively). A recent report showed that with more monodispersed dots,

a splitting in the first excitonic feature happened, which suggested that the feature was actually a combination of 2 transitions ($1S_h$-$1S_e$ and $1P_h$-$1S_e$).[102] However, even after Gaussian fit and only considering the $1S_h$-$1S_e$ transition, the absorption shoulder was still broader than aggregated HgTe CQDs. This might be due to the different particle shapes from three syntheses, i.e. spherical (non-aggregated) vs. tetrahedral (aggregated), but further experiments and calculations need to be done to verify it.

To summarize section 2.3, non-aggregated HgTe CQDs were synthesized using $Hg(oleate)_2$ and TOPTe, the former was made in-situ with HgO and oleic acid. A large Hg:Te precursor ratio (10:1) is needed to produce Hg-rich surface and improve stability. The particle growth is very slow and different sizes could be obtained after days of reaction. The dots are aggregated at small sizes but become separated as they grow. Large particles are stable for weeks in the absence of thiols. This synthesis provides an alternative route for the $(TMS)_2Te$ method in section 2.2 and avoids the use of very reactive and expensive $(TMS)_2Te$ precursor. The similarity between OAcid-synthesized HgTe CQDs and oleate-capped PbS or PbSe also makes it possible to borrow some ideas such as cation exchange and surface doping from these well-studied systems.[103-106]

2.4 HgTe/CdTe core/shell Heterostructures Synthesized via c-ALD

2.4.1 Synthesis Procedures

The detailed procedures are shown below:

a. Oleylamine (OAm) (Sigma-Aldrich, 70%) was purified by degassing it using a Schlenk line setup under vacuum at 135 °C for 3 h. It was then cooled down under argon and stored in glovebox for future use;

b. Prepare non-aggregated HgTe CQDs in glovebox. In a typical synthesis, $HgCl_2$ (0.2 mmol, Sigma-Aldrich, 99.5%) and 5 mL of purified OAm was added to a 20 mL vial. The mixture was heated on hot plate at 100 °C to dissolve the $HgCl_2$. Reset the hot plate at 110 °C and injected $(TMS)_2Te$ (0.1 mmol, Fisher, 98%) into the vial. The solution turned black immediately. Reacted for 10 min and quenched in 5 mL of TCE. Precipitated the dots by adding ethanol followed by centrifugation. The dots were re-dispersed in 10 mL of toluene for shell growth;

c. Synthesize HgTe/CdTe core/shell via colloidal atomic layer deposition (c-ALD) in glovebox. In a typical synthesis, 1 mL of HgTe toluene solution (contained 0.01 mmol of HgTe) was put in a test tube together with 100 μL of purified OAm and 2 mL of formamide (FA) to form a 2-phase system. To grow one layer of CdTe, 40 μL of 1.1 M Na_2Te/FA solution was injected and vigorously stirred for 2 min. Then the bottom FA phase was removed and the top toluene phase was washed three times with FA to remove any leftover Na_2Te. Next, 2 mL of FA and 60 μL of 0.1 M solution of cadmium acetate ($Cd(OAc)_2$, Sigma-Aldrich, 99.99%) in FA was injected and stirred for 2 min. The FA phase was removed and the toluene phase was washed three times with FA to remove any leftover $Cd(OAc)_2$. After the desired number of CdTe layers were grown, 3 drops of DDT was added and the dots were precipitated with ethanol and centrifugation. The precipitate was re-dispersed in TCE for further characterization.

2.4.2 Properties of c-ALD synthesized HgTe/CdTe Core/Shells

Following the prior synthesis protocol in section 2.2, we use $(TMS)_2Te$ and $HgCl_2$ in oleylamine to synthesize HgTe CQDs at 100-120 °C. The CQDs are quasi-spherical and well-separated as

shown in Figure 2-9a.[65] We explored the growth of CdTe shells using a hot-injection method but found no conditions of reagents or temperatures where the core sizes and compositions could be preserved. The most typical outcome was larger and alloyed HgCdTe nanoparticles with blue-shifted energy gaps. c-ALD was introduced by Ithurria and Talapin as a method to form a shell at room temperature.[107] Here we chose CdTe as the shell material because it forms a type-I core/shell structure with HgTe with nearly matching lattice constants of 0.646 nm for HgTe and 0.648 nm for CdTe.[64, 108]

Figure 2-9a shows the TEM images of HgTe core and HgTe/CdTe core/shell after 3 c-ALD growth cycles. After c-ALD growth, the core/shells remain quasi-spherical and well-separated in solution. The sizes were determined by visual determination from the TEM images. The average diameter increases from 9.0 ± 0.3 nm to 10.1 ± 0.3 nm or a ~12% size increase. The error given is the variance of the measurements divided by the square root of the number of measurements (around 100). The size increase of 1.1 ± 0.4 nm, corresponds to ~1.7 monolayers of CdTe, using half of the CdTe lattice constant of 0.648 nm for one monolayer. In spite of much effort, the size did not increase with subsequent c-ALD cycles. More cycles only led to secondary nucleation, despite washing the colloids three times with FA after each half cycle. Given the lack of strain expected in this lattice matched core/shell structure, the difficulty with c-ALD is tentatively attributed to the choice of ligands.

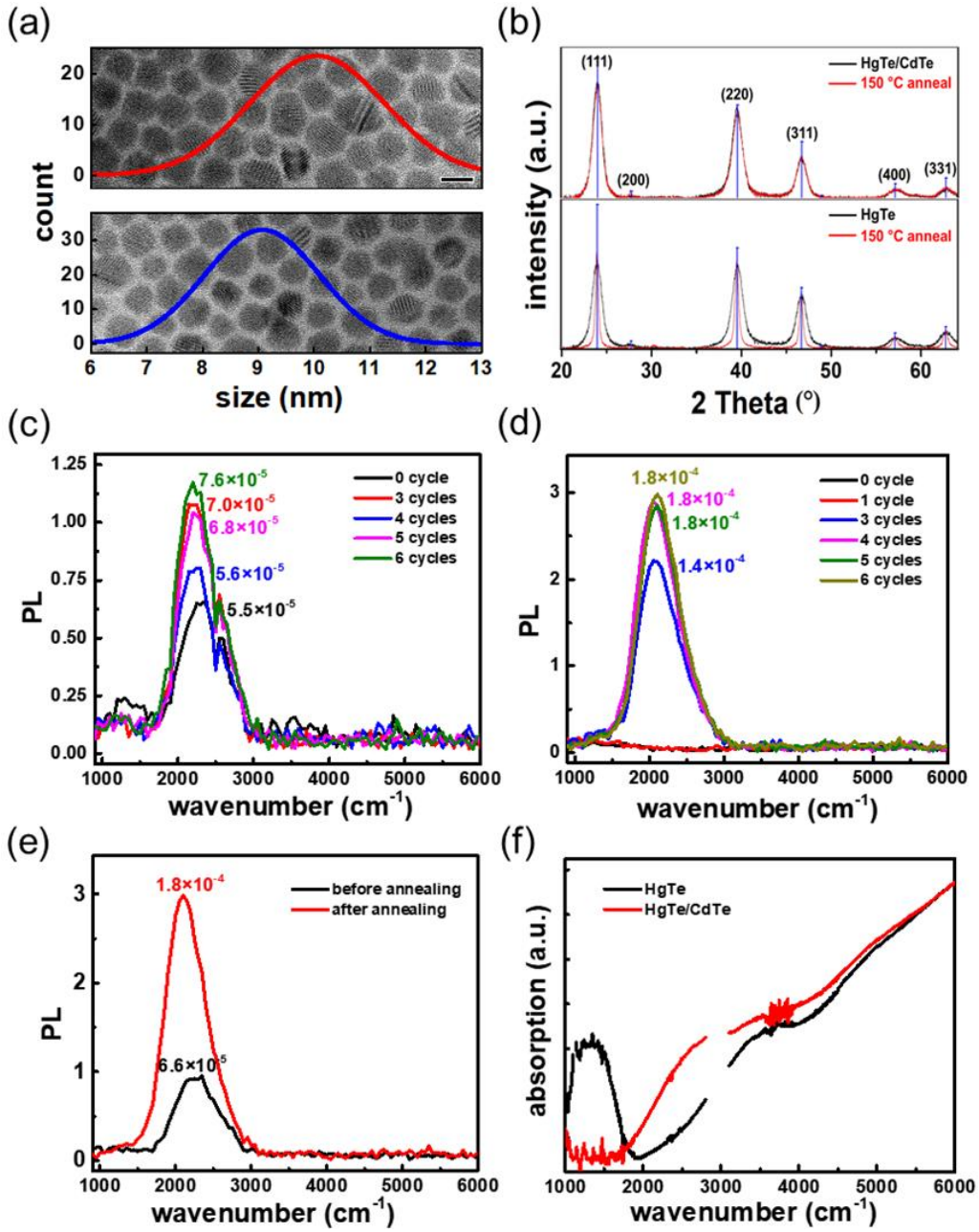

Figure 2-9 *(a) TEM images and normal size distributions of (bottom) HgTe core and (top) HgTe/CdTe core/shell after 3 cycles of c-ALD (scale bar: 10 nm); (b) XRD spectra of (bottom) HgTe core and (top) HgTe/CdTe core/shell before (black curve) and after (red curve) annealing at 150 °C for 1 h. The blue lines indicate the position of bulk zinc-blende HgTe; (c) PL spectra of HgTe core and HgTe/CdTe core/shells, measured in TCE solution; (d) PL spectra of HgTe/CdTe core/shells after EDT ligand exchange and annealing, measured on films; (e) PL spectra of*

Figure 2-9, continued

HgTe/6-cycle CdTe before and after annealing at 160 °C for 2 h, measured on the same film. The values in (a-c) are the integrated QY; (f) Absorption spectra of HgTe core and HgTe/CdTe core/shell measured in TCE solution, normalized at 6000 cm^{-1}. Absorption ~2900 cm^{-1} was blanked due to the strong C-H vibrations from surface ligands.

Figure 2-9b shows XRD spectra. The FWHM for the XRD peak at ~24° is 1.4° for the HgTe core and 1.2° for the HgTe/CdTe core/shell. This is also consistent with a 16% size increase with the lattice matched shell. Even though the CdTe shell is thin, it already improves dramatically the thermal stability of the CQD films. As shown in Figure 2-9b, the linewidth of the HgTe core XRD peak narrows 3-fold after annealing the films at 150 °C for 1 h, indicating a corresponding increase in the average grain size. On the other hand, the films of the HgTe/CdTe core/shell show no change in the XRD spectrum under the same annealing condition. The results also imply that no sintering happens to the CdTe shell at 150 °C, and this is consistent with the sintering studies of CdTe nanocrystals which required annealing temperatures around 300 °C.[109-110]

Figure 2-9c shows the PL of HgTe core and HgTe/CdTe core/shells in solution, normalized by their absorbance at 808 nm. The core PL quantum yield is around 6×10^{-5}, which is slightly lower than for the aggregated HgTe synthesis with dodecanethiol ligands, at similar energy of emission.[67] With the shell growth and the same ligand dodecanethiol, there is no shift of the emission but a systematic, yet moderate, increase in the PL intensity with the number of c-ALD cycles. With 6 cycles, the PL increases 2-fold. This confirms that the CdTe shell indeed forms a type-I heterostructure with HgTe. However, the 2-fold PL enhancement for a type-I core/shell, with a weak PL to start from, is strikingly different from the high PL QY typically obtained with type I

core/shell of wider gap CQDs. Another effect of the shell growth is the removal of n-doping. The initial HgTe core, which has an average size of ~9 nm, is n-doped as demonstrated by an air-stable intraband absorption peak at ~1500 cm^{-1} in Figure 2-9f. After the CdTe shell growth, the intraband absorption disappears, as shown by the red curve in Figure 2-9f. This removal of doping upon shell growth has been observed in HgS and HgSe before.[58, 85]

Figure 2-9d shows the PL spectra of HgTe/CdTe core/shells after EDT ligand exchange and annealing, measured on films; the PL of the HgTe core is completely quenched after annealing at 150 °C for 30 min, and this is consistent with the sintering to larger particles determined by XRD. In contrast, the PL of core/shells neither decreases nor shifts after 2 h at 160 °C except for the 1 c-ALD cycle sample. The latter is likely caused by its incomplete surface passivation. The PL intensity actually benefits from the annealing treatment. From Figure 2-9e, the PL improves more than 3 times for the 6-cycle sample, after annealing. The PL improvement upon annealing is seen for all core/shell samples.

At temperatures above 180 °C, the PL of films of HgTe/CdTe core/shells starts to blue-shift. This is assigned to the Hg/Cd alloying through the core/shell interface. 180 °C is therefore a temperature limit for HgTe/CdTe core/shell. Future attempts to grow a CdTe shell with hot injection will then require the use of reagents below that temperature. A similar upper temperature limit is known for growing HgTe/HgCdTe quantum well.[111-112]

To summarize section 2.4, using c-ALD, a thin CdTe shell was effectively grown on the HgTe cores at room temperature. The thin shell protects the quantum dots against annealing and preserves the optical and structural properties up to the alloying temperature of 180 °C. The shell also provides a moderate PL enhancement by a factor of ~2.

2.5 Shape Control of HgTe Nanoparticles with Tellurone Precursor

2.5.1 Synthesis Procedures

Thiourea, selenourea and their derivatives have proved themselves to be a useful group of precursor for HgSe, PbSe, PbS and CdS CQDs syntheses.[15, 52-54, 72] Naturally, one may consider developing a similar tellurourea synthesis. After checking literature, the only possible tellurourea derivative is tellurone, which is a four-substituted tellurourea and first made by Arduengo in 1997.[113]

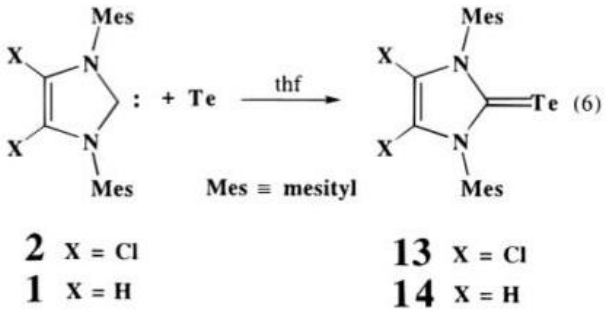

Figure 2-10 *Synthetic route for making tellurone. Adapted from reference 113.*

As shown in Figure 2-10, a very special carbene compound needs to be used for the tellurone synthesis. This type of carbene, named Arduengo carbene, has excellent stability and could be crystalized and stored in the absence of water and oxygen.[114-116] The procedures for making tellurone are shown below:

a. In glovebox, weighed 1 mmol 1,3-Dimesitylimidazol-2-ylidene (TCI America, 97%) and 1 mmol tellurium powder (Sigma-Aldrich, 200 mesh, 99.5%) in a pre-dried 20 mL glass vial;

b. Added 10 mL tetrahydrofuran (THF, Sigma-Aldrich, anhydrous, 99.9%) to the vial. Started stirring at room temperature for 12 h;
c. Heated the solution at 60 ℃ for 1 h. The top layer was clear yellow-orange solution and there was some black powder (undissolved tellurium) on the bottom. Collected the top solution and used directly as tellurium precursor.

The procedures for making HgTe CQDs with various shapes are shown below:

a. OAm was purified by degassing it using a Schlenk line setup under vacuum at 135 °C for 3 h. It was then cooled down under argon and stored in glovebox for future use;
b. Weighed 0.1 mmol of mercury precursor along with 6 mL purified OAm in a 3-neck flask. Under the Schlenk line, degassing it at room temperature for 10 min, then degassing at 90 °C for another 30 h. The final shape of HgTe CQDs were tuned by changing different mercury precursors;
c. Flushed the system with argon and kept the Hg precursor under argon for 10 min;
d. Reset the temperature at 100 °C and injected 0.5 mL tellurone precursor. The solution turned black. Extracted aliquots of reaction mixtures with a long needle syringe and quenched it in chloroform;
e. Precipitated the dots by adding a mixture of acetone and methanol until the solution became turbid. After centrifugation, black precipitate was collected. Washed the precipitate with ethanol for 3 times to remove excess ligands. The dots were re-dispersed in TCE.

2.5.2 Properties of Anisotropic HgTe Nanoparticles

As shown in Figure 2-11, different mercury precursors will result in different shapes. The used precursors are $Hg(Ac)_2$, $HgCl_2$, $Hg(SCN)_2$ and a combination of $Hg(Ac)_2$ and $HgCl_2$ (1:1). The actual Hg/Te ratio is larger than 2:1, given the fact that not all tellurium powders dissolved in THF.

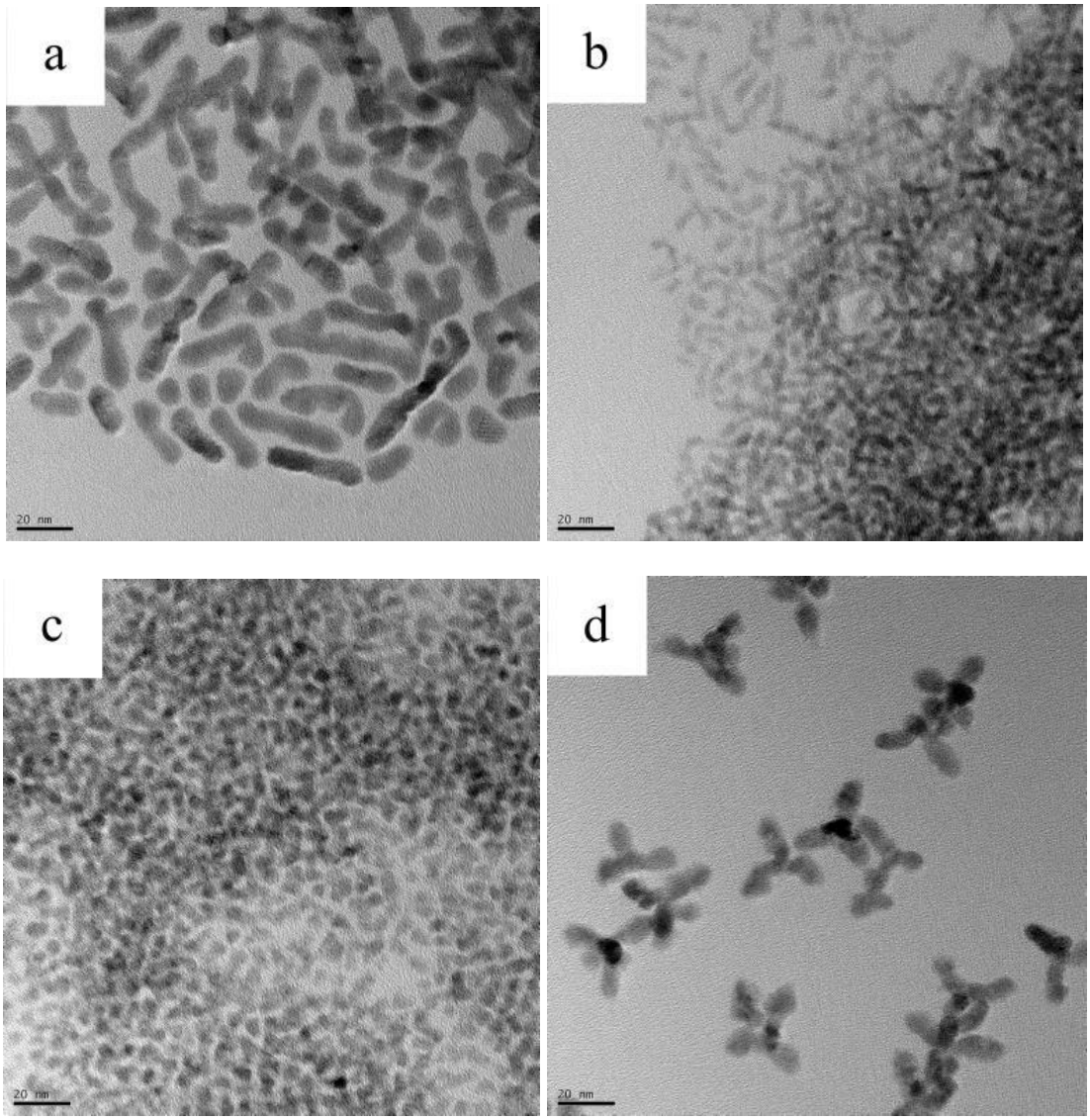

Figure 2-11 *TEM images of HgTe CQDs with different shapes: (a) branched thick nanorods; (b) branched thin nanorods; (c) quasi-spherical particles; (d) tetrapods. The particles were obtained using $HgCl_2$, $Hg(SCN)_2$, $Hg(Ac)_2$ and 1:1 = $Hg(Ac)_2$: $HgCl_2$ as mercury precursor and tellurone as tellurium precursor, respectively.*

Shape control of CQDs is usually achieved by tuning ligand environment.[117-120] Different ligands can preferentially bind to certain crystal facets, which tunes the relative surface energies on different facets. Things are different in this tellurone synthesis, where the ligand is the same OAm. One possible reason behind the different shapes is the reactivity difference of mercury precursors. In a typical synthesis, $Hg(Ac)_2$ turns black in 1 s after the injection of tellurone, while $HgCl_2$ and $Hg(SCN)_2$ need 10 s and 20 s, respectively. As a comparison, the color change is instant for Sean Keuleyan's TOPTe synthesis and different mercury precursors have no effect on the final products.[36] This indicates that tellurone has a much lower reactivity compared with TOPTe, which is due to its 4-substituted molecular structure and allows it to differentiate the various mercury precursors based on their reactivity.[52-53] In section 2.2, we mentioned the shape difference between aggregated and non-aggregated HgTe CQDs came from the fact that $(TMS)_2Te$ is much more reactive than TOPTe. The same idea could be used here: the more reactive the precursor is, the less anisotropic the final particles are.

Reactivity: $Hg(Ac)_2$ > $HgCl_2$ and $Hg(Ac)_2$ mixture > $HgCl_2$ > $Hg(SCN)_2$

Anisotropy: quasi-spherical < tetrapods < (thin or thick) branched nanorods

The synthesized HgTe nanoparticles are still zin-blende and their typical absorption and PL spectra are shown in Figure 2-12.

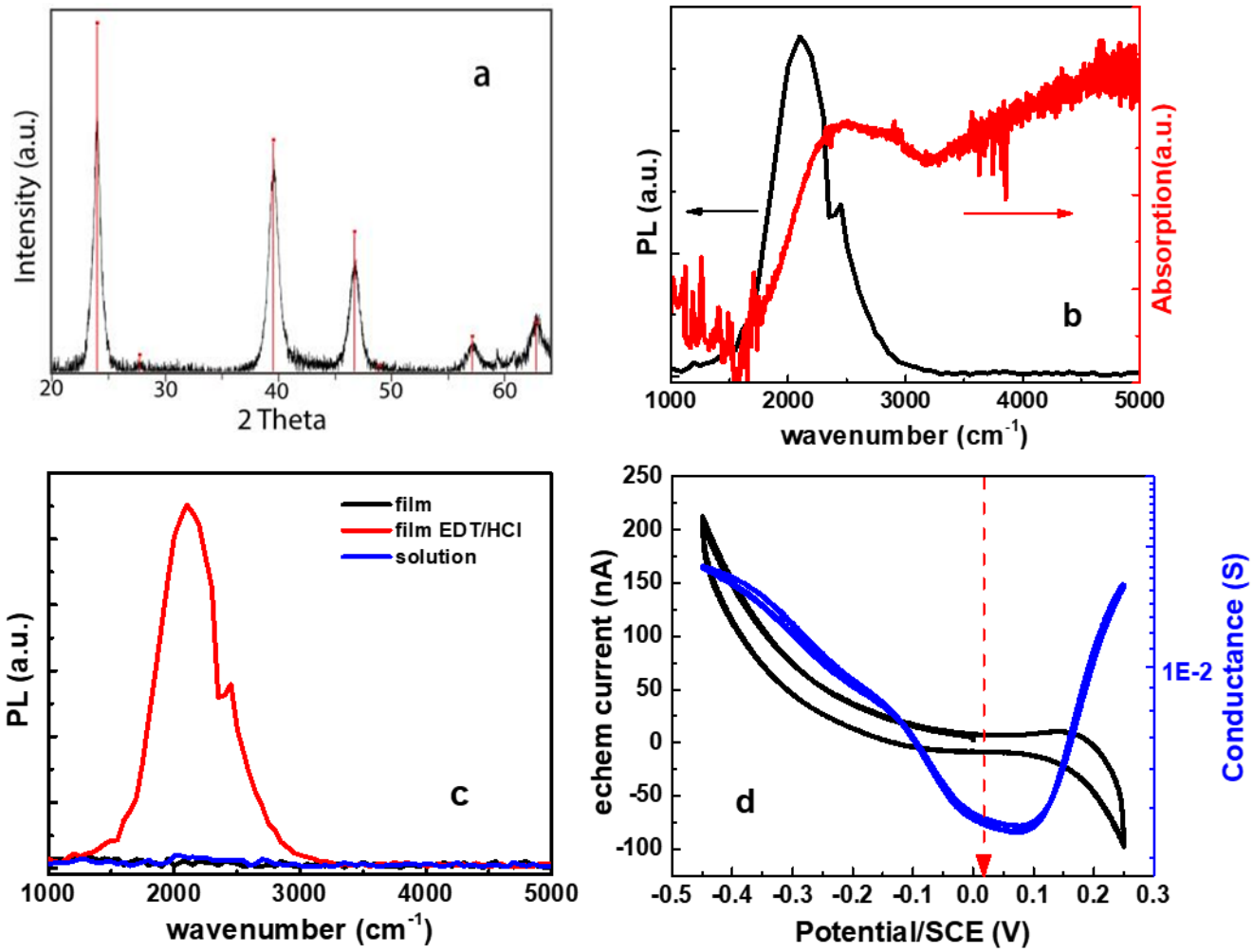

Figure 2-12 *(a) XRD spectrum of HgTe nanorods corresponding to Figure 2-11a. The red lines indicate the position of bulk zinc-blende HgTe; (b) ATR-IR and PL spectra of the same sample. Measured on ZnSe window after EDT/HCl ligand exchange; (c) PL measured under different conditions. PL has reasonable intensity only on film with ligand exchange; (d) Cyclic voltammetry results of the same HgTe nanorods. The black and blue curves are the electrochemistry current and conductance of the film, respectively. The red dashed arrow is the position of the rest potential. The reference electrode is saturated calomel electrode.*

The branched nanorods have a clear absorption feature and PL emission at 2100 cm^{-1} with almost no Stokes shift. The PL peak has a FWHM ~550 cm^{-1} but only shows up after ligand exchange. This indicates there might be a strong energy coupling to ligand vibrational modes in these nanorods. Given the fact that the width of branched nanorods is ~7-8 nm (the length varies a lot), which is smaller than the diameter of 5 μm emitting HgTe quantum dots, there is less confinement in the 1D nanorods compared with 0D quantum dots. Similar behavior has been observed in CdSe nanowires versus nanorods, where the absorption energy red-shifts from nanorods to the less confined nanowires.[121]

Electrochemistry result in Figure 2-12d shows that the nanorods are intrinsic and have a 2-order higher mobility compared with non-aggregated HgTe CQDs, even better than aggregated ones (shown in Figure 2-4). This could be explained by the smaller numbers of grain boundaries and therefore the recombination centers. The branched structures that connect several nanorods together may also facilitate the charge transport.

2.6 Phase Control of HgTe/CdSe Heterostructures

All HgTe and HgTe/CdTe shown above are in zinc-blende (*zb*-) phase. And to the best of our knowledge, it is the only reported phase in mercury chalcogenide CQDs.[25, 31, 36] Zin-blende is the kinetically favored phase, and the low temperatures used in mercury chalcogenide growth might be the reason that it becomes dominant.

In this section, inspired by the work done by Jennifer Hollingsworth and her co-workers, I successfully synthesized *zb*-HgTe/wurtzite-CdSe heterostructures.[122] The growth method is hot-injection. As mentioned in section 2.4, hot-injection is usually not a good way to synthesize HgTe/CdSe (or CdTe) because the temperature needed for growing CdSe or CdTe is too high for

HgTe. Experiments also proved it. When trying to grow CdSe or CdTe at ~180 °C, non-aggregated OAm-synthesized HgTe cores crashed out quickly. It is only possible to grow these heterostructures from OAcid-synthesized HgTe CQDs.

2.6.1 Synthesis Procedures

The detailed synthesis procedures are shown below:

a. In glovebox, weighed 10 mmol Se powder (Sigma-Aldrich, 99.99%) in a 20 mL vial. 10 mL of TOP (Sigma-Aldrich, 97%) was added and the solution was stirred at room temperature overnight to form a yellow solution. This step is to prepare 1 M TOPSe as Se precursor;

b. 10 mmol CdO (Sigma-Aldrich, 99.99%) and 40 mmol OAcid (Sigma-Aldrich, 90%) was added to a flask, which was purged under argon for 15 min. Next, the mixture was heated at 240 °C for 20 min to dissolve CdO powders. The solution was cooled to 50 °C and poured into 100 mL of acetone. White cadmium oleate solid precipitated out. Rinsed the product with acetone twice and dried it under vacuum for 2 days. The cadmium oleate powder was dissolved in OAcid to make a 0.5 M solution and used as Cd precursor;

c. Synthesized HgTe CQDs in OAcid following the procedures in section 2.3.1. The HgTe cores had a size ~7.4 nm diameter;

d. Took 2 mL OAcid and 4 mL ODE (Sigma-Aldrich, 90%) in a 3-neck flask. The flask was degassed under Schlenk line for 1 h. 1 mL of HgTe TCE solution from step d was injected into the flask and degassed for another 30 min to remove TCE;

e. Flushed the system with argon and kept the HgTe cores under argon for 15 min;

f. 0.6 mL of Cd(oleate)$_2$ solution, 0.3 mL of TOPSe and 5.1 mL of ODE were filled in a 6 mL syringe. Loaded the syringe on a syringe pump. Next, increased the temperature of the flask to 200 °C, started the pump at an injection speed of 1.6 mL/h. When the injection was finished, cooled down the reaction mixture to room temperature and quenched in chloroform;

g. Precipitated the quantum dots with acetone and ethanol followed by centrifugation. Re-dispersed in TCE.

2.6.2 TEM and XRD of *zb*-HgTe/*w*-CdSe Tetrapods

The TEM image and XRD spectrum are shown in Figure 2-13.

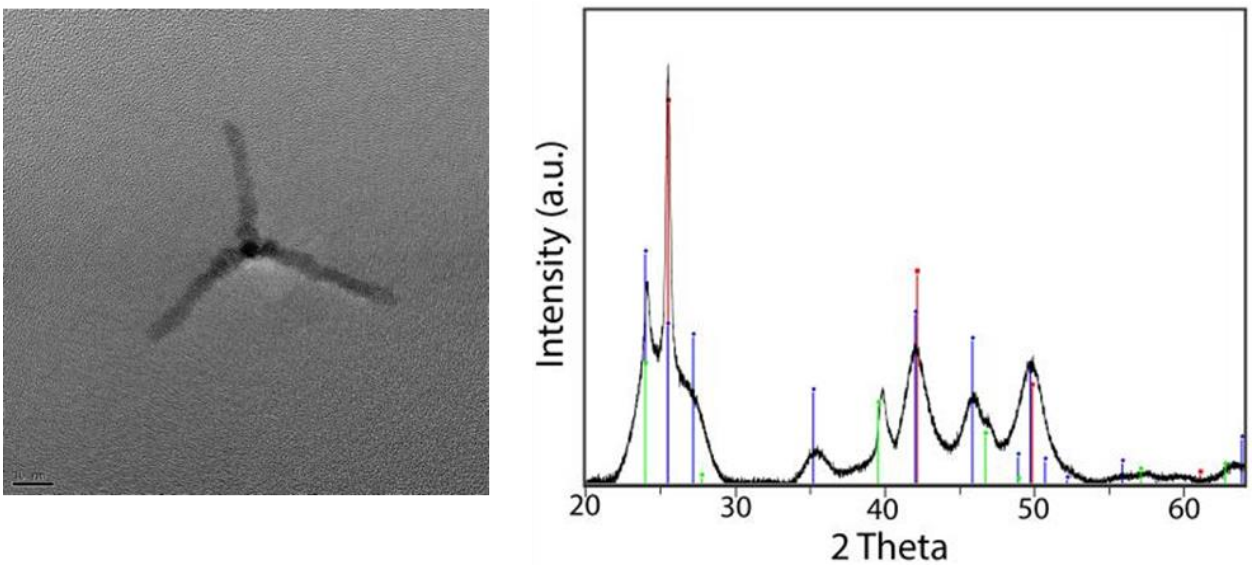

Figure 2-13 *(left) TEM and (right) XRD of HgTe/w-CdSe. Green, red and blue lines indicate the positions of zb-HgTe, zb-CdSe and w-CdSe, respectively.*

The *zb*-HgTe/*w*-CdSe heterostructure has a tetrapod shape. The coexistence of *zb*-HgTe and *w*-CdSe can be verified by XRD spectrum. While the peak ~45.8° indicates the *w*-CdSe, the peak

~39.6° and the little shoulder ~46.8° suggest that *zb*-HgTe is still in the structure. This seeded growth of wurtzite arms on zinc-blende cores has been used to synthesize a variety of different tetrapods.[122-125] The general idea is to let wurtzite arms grow along their (0001) directions, from (111) facets of the zinc-blende cores. This will form the least strained interface between *w*- and *zb*-domains.

The same idea could be used to grow *zb*-HgSe/*w*-CdSe tetrapods, which will be discussed in section 3.4. The tetrapods are nonemissive.

2.7 Conclusions

In this chapter, I described the efforts of growing various HgTe CQDs and their heterostructures. Non-aggregated HgTe CQDs could be made in oleylamine or oleic acid, which allows the growth of core/shells for the first time. HgTe/CdTe core/shell has a type-I structure and is the first successful shell growth on HgTe with excellent thermal stability. Moreover, different shapes and phases could be achieved in HgTe and *zb*-HgTe/*w*-CdSe by tuning the right synthetic parameters such as precursor and surface ligand. These results will provide new possibilities for a variety of HgTe-based IR applications, such as photodetection and IR-lasing.

Chapter 3 Synthesis of HgSe CQDs and Core/Shells

In this chapter, the synthesis of more monodispersed HgSe CQDs will be discussed, using a less reactive substituted selenourea precursor. HgSe/CdSe core/shells are grown in both c-ALD and hot-injection ways with improved PL at 5 μm and better thermal stability. *zb*-HgSe/*w*-CdSe tetrapods and phase control by changing precursors will also be discussed. This chapter includes the published results from reference 77 as well as some unpublished data.

3.1 Synthesis and Properties of Monodispersed HgSe CQDs

In the previous HgSe CQDs synthesis by Zhiyou Deng et al., the reaction between selenourea and $HgCl_2$-amine is not very controllable due to the high reactivity of selenourea. During the hot-injection, if we cannot instantaneously mix the two precursors, inhomogeneity will rise from the nucleation stage. For example, at the time the last drop of selenourea meets $HgCl_2$, HgSe nuclei from the first drop of selenourea may already grow to a large size. As a result, the size dispersion of HgSe CQDs is not good, usually ~10-15%, and there could be a large variation from time to time depending on how good the mixing is.[15]

Jonathan Owen and his group first synthesized 3 or 4-substituted selenourea (or thiourea), which could lower the reactivity of selenourea (or thiourea) several orders of magnitude.[52-54] Precursor mixing becomes less of a problem because of the low reactivity. Figure 3-1 shows the one-step synthetic route for making a special 3-substituted selenourea using selenium powder, isocyanide and amine. According to Owen, this precursor is 3-4 orders lower in conversion rate compared with selenourea and can be easily made at 95% yield. The low conversion rate also helps

maintaining a relatively high precursor concentration in the reaction mixture, which will suppress the Ostwald ripening. It will be the precursor for HgSe CQDs synthesis in section 3.1.

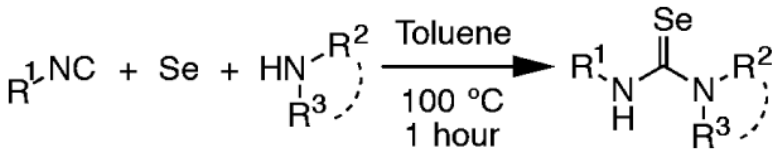

R^1	R^2	R^3	yield (%)
n-C_4H_9	$-(CH_2)_5-$		95

Figure 3-1 *Synthetic route for making substituted selenourea. Adapted from reference 53.*

The detailed synthesis procedures for making substituted selenourea are shown below:

a. In glovebox, weighed 6 mmol selenium powder (Sigma-Aldrich, 100 mesh, 99.99%) in a 20 mL glass vial. Added 4.8 mL toluene (Sigma-Aldrich, anhydrous, 99.8%), 0.6 mL piperidine (Sigma-Aldrich, 99.5%) and 0.62 mL butyl isocyanide (Sigma-Aldrich, 97%) to the same vial. Put the vial on hot plate;
b. Set the hot plate temperature at 115 °C and stirred for 1.5 h. Most selenium powders dissolved, and solution became yellow. Stored the solution in glovebox and used directly as Se precursor.

The detailed synthesis procedures for making HgSe CQDs are shown below:

a. Oleylamine (OAm) (Sigma-Aldrich, 70%) was purified by degassing it using a Schlenk line setup under vacuum at 135 °C for 3 h. It was then cooled down under argon and stored in glovebox for future use;

b. Weighed 0.13 mmol $HgCl_2$ powder (Sigma-Aldrich, 99.5%) along with 5 mL purified OAm in a 3-neck flask. Under the Schlenk line, degassing it at room temperature for 20 min, then degassing at 100 °C for another 1 h;
c. Flushed the system with argon and kept the Hg precursor under argon for 10 min;
d. Reset the temperature at the desired reaction temperature;
e. In glovebox, diluted 0.1 mL of substituted selenourea in 3 mL of purified OAm. The Se precursor was then loaded in a 3 mL syringe and quickly injected into the Hg precursor;
f. Extracted all reaction mixtures with a long needle syringe when the reaction was finished and quenched it in chloroform;
g. Precipitated the dots by adding a mixture of acetone and methanol until the solution became turbid. After centrifugation, black precipitate was collected. Washed the precipitate with ethanol for 3 times to remove excess ligands. The dots were re-dispersed in nonpolar solvents such as TCE and toluene.

Figure 3-2a shows a typical TEM image of HgSe CQDs after 2 h reaction at 100 °C. It forms a nice self-assembly pattern that indicates a good size dispersion. The monodispersity is ~6% at 6.5 nm diameter, which has never been achieved using previous methods.

The HgSe CQDs has narrow intraband absorption peaks as anticipated. The absorption peak has a wide tunability between 2000 cm^{-1} and 3000 cm^{-1}. Compared with selenourea synthesis, which usually finishes within 10 min, these new syntheses are much slower, requiring hours to achieve similar sizes and absorption peak positions.

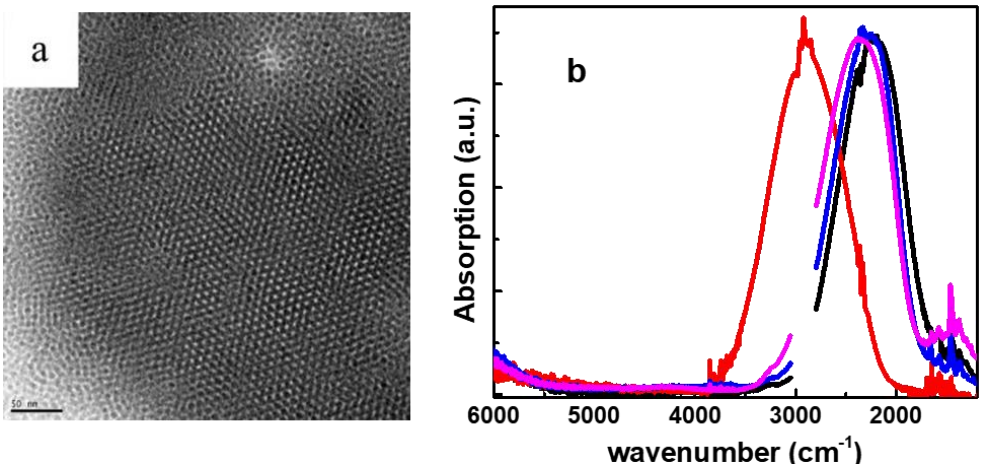

Figure 3-2 *(a) TEM image of 6.5 nm HgSe CQDs that shows self-assembly pattern (scale bar: 50 nm); (b) ATR-IR spectrum of HgSe CQDs with different sizes. Measured on ZnSe substrate.*

3.2 Synthesis of HgSe/CdSe Core/Shell via Hot-Injection

3.2.1 Synthesis Procedures

The detailed synthesis procedures are shown below:

a. OAm was purified by degassing it using a Schlenk line setup under vacuum at 135 °C for 3 h. It was then cooled down under argon and stored in glovebox for future use;

b. In glovebox, weighed 10 mmol Se powder (Sigma-Aldrich, 99.99%) in a 20 mL vial. 10 mL of TOP (Sigma-Aldrich, 97%) was added and the solution was stirred at room temperature overnight to form a yellow solution. This step is to prepare 1 M TOPSe as Se precursor;

c. 10 mmol CdO (Sigma-Aldrich, 99.99%) and 40 mmol OAcid (Sigma-Aldrich, 90%) was added to a flask, which was purged under argon for 15 min. Next, the mixture was heated at 240 °C for 20 min to dissolve CdO powders. The solution was cooled to 50 °C and

poured into 100 mL of acetone. White cadmium oleate solid precipitated out. Rinsed the product with acetone twice and dried it under vacuum for 2 days;

d. HgSe CQDs were synthesized following the procedures in reference 15 and re-dispersed in TCE at a concentration of 0.01 mmol HgSe/mL TCE;
e. 1 mL of HgSe TCE solution and 5 mL of purified OAm was added to a 3-neck flask. The flask was degassed under Schlenk line for 30 min to remove TCE, which was then purged with argon for 15 min. At the same time, cadmium oleate (0.2 g, 0.3 mmol) was dissolved in 5.7 mL of purified OAm in glovebox. The cadmium oleate solution and 0.3 mL of TOPSe were filled in a 6 mL syringe. Loaded the syringe on a syringe pump. Next, increased the temperature of the flask to 200 °C, started the pump at an injection speed of 1.6 mL/h. When the injection was finished, cooled down to room temperature and quenched in chloroform;
f. Precipitated the quantum dots with acetone and ethanol followed by centrifugation. Re-dispersed in TCE.

3.2.2 Properties of HgSe/CdSe Core/Shell Synthesized via Hot-Injection

Alloying was previously observed in HgSe/CdS core/shells at ~250 °C.[58] This is a higher temperature than for HgTe/CdTe, which is likely related to the larger lattice energy of HgSe compared to HgTe. Even though the CdSe CQD synthesis is normally conducted at temperatures above 250 °C, previous studies have shown that some selenium precursors can react with cadmium oleate at temperatures as low as 150 °C.[126] We therefore explored a number of selenium precursors at different growth temperatures including Se-OAm, Se-ODE, $(TMS)_2Se$ and TOPSe. Our best results were obtained with TOPSe as the selenium precursor at 200 °C via slow syringe pump

injection. Compared with the two published methods of shell growth on HgSe,[58-59] this new approach allows us to grow thick CdSe shell without independent nucleation.

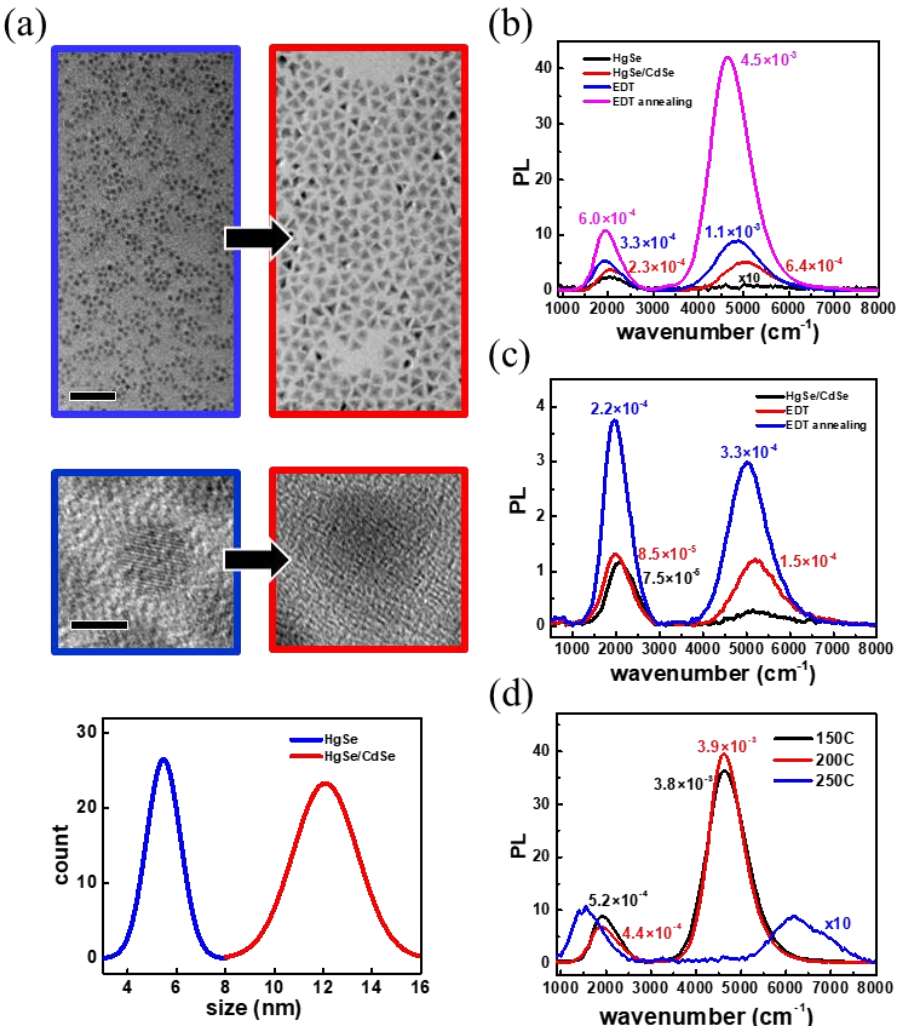

Figure 3-3 *(a) TEM, HRTEM images and normal size distributions of (blue) HgSe core and (red) thick HgSe/CdSe core/shell (scale bar: 50 nm in TEM and 5 nm in HRTEM); PL spectra of HgSe/CdSe films with different treatment, measured (b) in air and (c) in a N_2-filled cell; (d) PL spectra of EDT-treated HgSe/CdSe film after annealing at different temperatures for 1 h. The values on the spectra are the intraband and interband QY.*

Figure 3-3a shows the TEM images of HgSe core and HgSe/CdSe core/shell. The amount of shell precursor versus core material is 30:1. The particle shape changes from spherical to tetrahedral, with a small proportion of branch-shaped structures (polypods). As previously observed,[51, 127] lowering the growth temperatures for colloids yields more angular shapes. XRD shows that the HgSe/CdSe core/shell is still zinc-blende. The particle size increases significantly from 5.4 nm (diameter) to 12.1 nm (from the vertices to the edge) after the shell growth. Assuming a perfect tetrahedron, the core would however barely fit in the core/shell, given that the tetrahedron in-sphere is ~5.7 nm diameter. Therefore, we expect that the CdSe layer remains thin in the middle of the facets.

For HgSe cores ~5.4 nm diameter, the intraband PL is around 2000 cm^{-1} and the interband PL around 4500 cm^{-1}. As shown in Figure 3-3c, when the HgSe/CdSe core/shell film are under N_2, the interband PL decreases significantly compared with the same film in air and most of the ratio change comes from the interband PL.

Figure 3-3d shows that films of the hot-injection HgSe/CdSe have excellent thermal stability up to 200 °C with some minor changes in doping. At 250 °C, the interband PL blue-shifts and the intraband red-shifts. We again attribute this to Hg/Cd alloying, since it is consistent with the formation of a wider gap material with smaller confinement. This is similar to early reports of alloying in CdSe/ZnSe nanoparticles occurring at a specific temperature.[128] This alloying also strongly decreases the PL intensity as carriers are no longer confined to the core.

To summarize section 3.2, we developed a hot-injection method to grow HgSe/CdSe core/shells. There is a large increase in particle size after shell growth and the quantum dot shape changes from spherical to angular. More importantly, no independent nucleation is observed, which means in

principle, there is no limit in shell thickness. Compared with our best HgSe, the intraband PL of HgSe/CdSe core/shells improves 2-fold after EDT ligand exchange and annealing. We also reported the first intraband PL QY of 6×10^{-4} at 5 μm emission. HgSe/CdSe core/shell has excellent thermal stability up to 200 °C, above which interface alloying will start to happen.

3.3 Synthesis of HgSe/CdX (X=S, Se, Te) Core/Shell via c-ALD

3.3.1 Synthesis Procedures

The detailed procedures are shown below:

a. Oleylamine (OAm) (Sigma-Aldrich, 70%) was purified by degassing it using a Schlenk line setup under vacuum at 135 °C for 3 h. It was then cooled down under argon and stored in glovebox for future use;
b. HgSe CQDs were synthesized following the procedures in reference 15 and re-dispersed in TCE at a concentration of 0.01 mmol HgSe/mL toluene;
c. Synthesize HgSe/CdX core/shell via colloidal atomic layer deposition (c-ALD) in glovebox. In a typical synthesis, 1 mL of HgSe toluene solution (contained 0.01 mmol of HgTe) was put in a test tube together with 100 μL of purified OAm and 2 mL of formamide (FA) to form a 2-phase system. To grow one layer of CdX, 40 μL of chalcogenide FA solution (0.5 M $(NH_4)_2S$, 1 M Na_2Se, 1.1 M Na_2Te for S, Se and Te, respectively) was injected and vigorously stirred for 2 min. Then the bottom FA phase was removed, and the top toluene phase was washed three times with FA to remove any leftover Na_2Te. Next, 2 mL of FA and 60 μL of 0.1 M solution of cadmium acetate ($Cd(OAc)_2$, Sigma-Aldrich, 99.99%) in FA was injected and stirred for 2 min. The FA phase was removed, and the toluene phase was washed three times with FA to remove any leftover $Cd(OAc)_2$. After the

desired number of layers were grown, 1 drop of OAm was added and the dots were precipitated with 0.1 M DDAB in ethanol and centrifugation. The precipitate was re-dispersed in TCE for further characterization.

3.3.2 Properties of HgSe/CdX Core/Shell Synthesized via c-ALD

c-ALD growth of HgSe/CdX (E=S, Se) core/shell has been used before to optimize the interband emission at 2 μm.[59] Here we focus on the intraband PL at 5 μm and we add the HgSe/CdTe system. The lattice mismatch between HgSe and CdX are < 0.1% with CdSe, 4.3% with CdS and 6.7% with CdTe. The effect of the various shells on the PL intensity and intraband/interband ratio is also investigated. According to Kasha's rule which states that the emission comes from the lowest energy transition, one could expect that an undoped dot would emit interband PL while dots doped with one or two electrons would emit intraband PL. Therefore, variations in the PL intensities can arise from changes of the doping as well as changes of the non-radiative mechanisms, both effects possibly arising from the shell.

Figure 3-4a shows the typical TEM images of HgSe core and HgSe/CdSe core/shell after 3 c-ALD growth cycles. From the size distributions in Figure 3-4a, the core size is 4.9 ± 0.3 nm, and the core/shell is 6.3 ± 0.3 nm. The percentage size increase is ~30% and therefore larger than for the case of the HgTe cores. The size increase is 1.4 ± 0.4 nm or ~2.3 monolayers of CdSe, using half of the CdSe lattice constant of 0.608 nm for one monolayer.

Figure 3-4b shows the effect of the three CdSe c-ALD cycles on the absorption of the solutions. Each cycle increases the first interband exciton and decreases the intraband absorption, indicating that the shell gradually undopes the cores.[58-59] The absorption from CdSe becomes clear by the last cycle with the absorbance increase above 14000 cm^{-1} (the bandgap of bulk CdSe). Figure 3-4c

shows the solution absorption spectra of HgSe/CdS and HgSe/CdSe, with 3 c-ALD cycles. The effects are similar, but the remaining n-doping follows CdS < CdSe. As the intraband absorption decreases, the peak red-shifts and becomes narrower. This is attributed primarily to the larger cores being the most likely to remain doped, since for a given size distribution, the electron states of large dots are at lower energies compared to small ones.

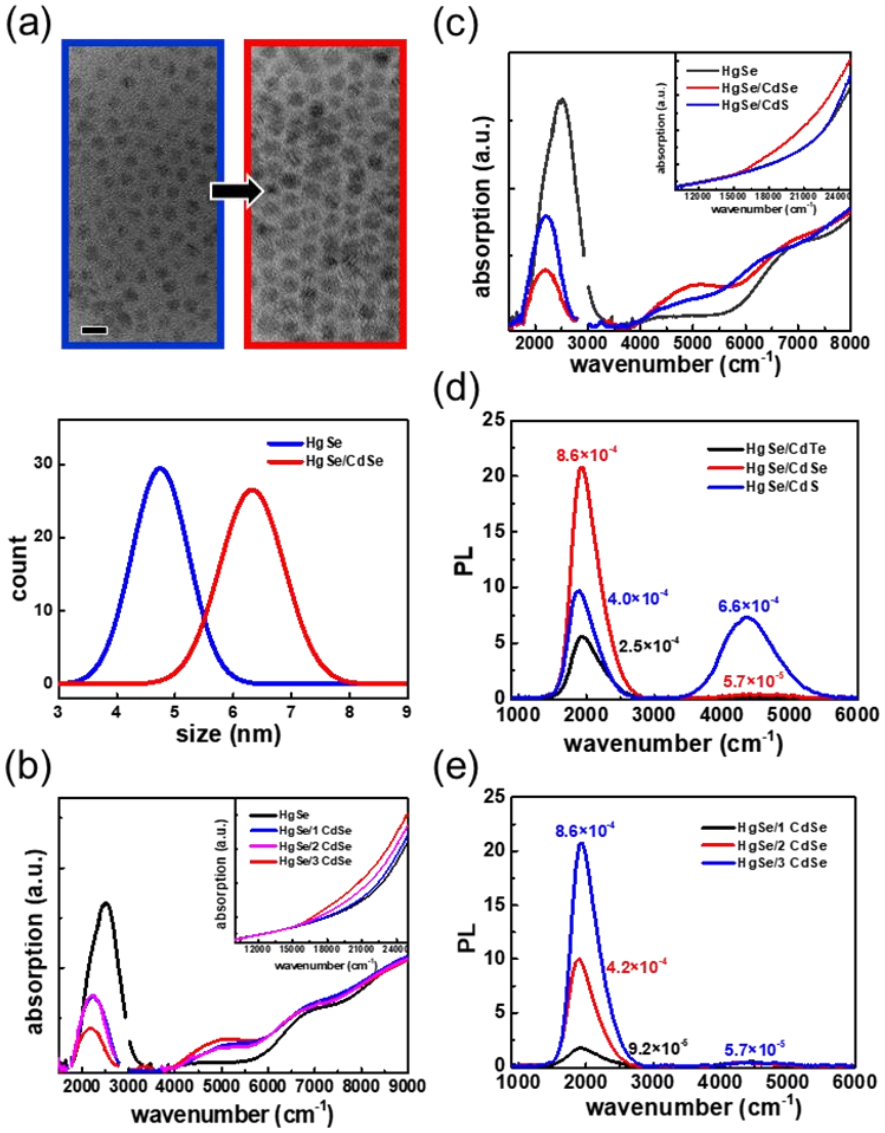

Figure 3-4 *(a) TEM images and normal size distributions of (blue) HgSe core and (red) HgSe/CdSe core/shell after 3 cycles of c-ALD (scale bar: 10 nm); (b) Solution absorption spectra*

Figure 3-4, continued

of HgSe and HgSe/CdSe CQDs with different numbers of c-ALD cycles. HgSe and HgSe/CdSe were normalized at the band gap of CdSe (Inset: same plot shows the solution absorption on the high-energy side); (c) Solution absorption spectra of HgSe and HgSe/CdX CQDs. HgSe and HgSe/CdSe were normalized at band gap of CdSe, HgSe and HgSe/CdS were normalized at band gap of CdS (Inset: same plot shows the absorption on the high-energy side); (d) PL spectra of films of HgSe/CdX CQDs; (e) PL spectra of films of HgSe/CdSe CQDs with different numbers of c-ALD cycles. All absorption spectra were obtained in TCE solution and PL spectra were measured as films with EDT ligand exchange.

Similar to previous results,[58] the HgSe/CdSe and HgSe/CdS core/shells in solution show interband PL but very weak intraband PL and this is attributed to quenching by vibrational features of solvent and ligands. The PL was therefore measured on films after EDT treatment.

As shown in Figure 3-4d, the interband PL intensity follows CdTe < CdSe < CdS. It was previously reported that the interband PL of HgSe/CdS was an order of magnitude stronger than for HgSe/CdSe and this was attributed to better hole confinement in HgSe/CdS.[59] Since the confinement for the holes states in the HgSe cores decreases in the order Te < Se < S, our observation could support the previous assignment of interband PL being affected by hole transfer to the outer surface.

The intraband PL intensity follows CdTe < CdS < CdSe. Since the different shell materials affect the doping of HgSe/CdX, we cannot confidently assign the differences to the PL efficiency. With our procedure, the brightest intraband PL was systematically obtained with CdSe shells.

Figure 3-4e shows the PL spectra for each CdSe cycle. The intraband PL increases from 1 cycle of c-ALD to 3 cycles. Combining the results of shell material and shell thickness, the strongest PL at 5 μm was obtained with films of HgSe/CdSe CQDs made with 3 c-ALD cycles of CdSe, and after EDT treatment. The PL intensity was ~5 times the intensity of the strongest intraband PL we ever measured with films of HgSe cores, with a quantum yield close to 1×10^{-3}.

3.3.3 Temperature Dependence of the HgSe/CdX Core/Shell Photoluminescence and Discussion

The is an important figure of merit for CQD applications. Near unity QY is readily available for quantum dots emitting in the visible range.[66] However, IR CQDs have low QY. In the short-wave IR range (1.4-3 μm), the best HgTe CQDs have PL QY comparable with PbSe or PbS.[33] The interband PL QY of HgSe is lower, with published value ~0.003 at 1.8 μm.[59] As the emission moves deeper into the infrared, the QY of HgTe CQDs decreases quasi-exponentially,[32] being of order 10^{-4} at 5 μm.[67] The non-radiative mechanisms are not yet known. One possible mechanism is a direct coupling of the electronic wavefunction to trap states as is typical for visible CQDs.[129] Trapping is usually activated and can therefore be investigated by the temperature dependence. The results of such measurements are shown in Figure 3-5.

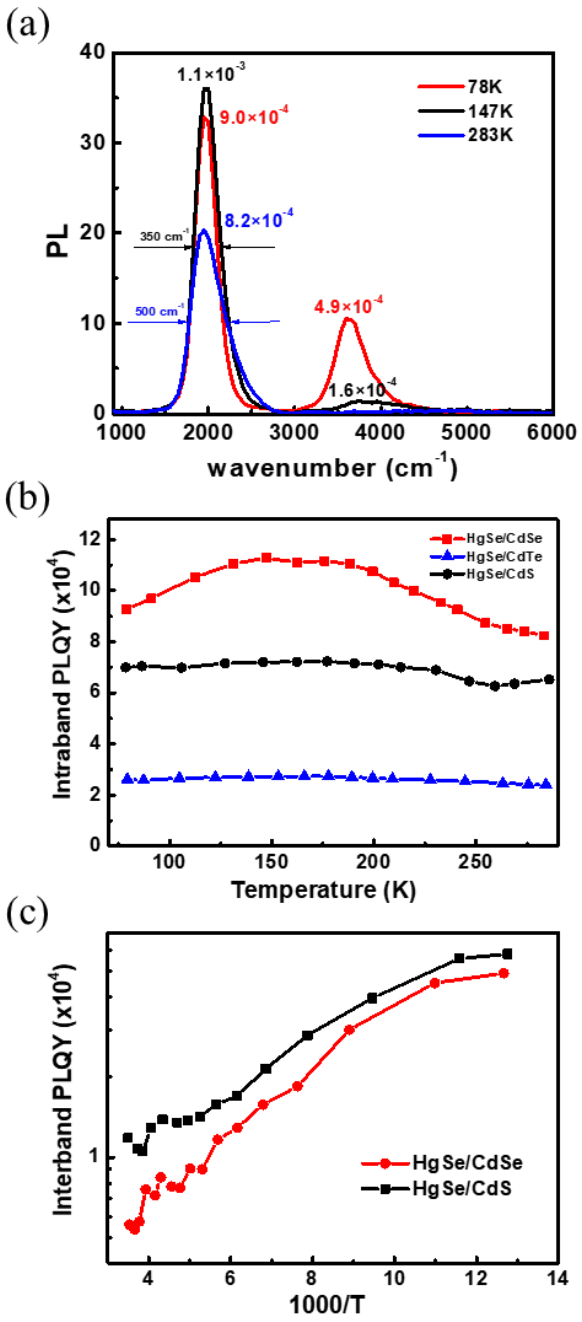

Figure 3-5 *(a) Temperature-dependent PL measurement of HgSe/CdSe. The values on the spectra are the calculated intraband QY. Similar measurements on HgSe/CdS and HgSe/CdTe are shown in supporting information, part 5; (b) Intraband PL QY as a function of temperature; (c) Interband PL QY on a log scale as a function of 1/temperature. The values on the spectra are the intraband and interband QY.*

As shown in Figure 3-5a, the intraband PL shows no shift with temperature within the setup resolution (50 cm^{-1}). The small intraband shift is consistent with a simple $k \cdot p$ model[15] even though the interband shows a large red-shift upon cooling.[4] The strong red-shift of the interband PL is similar to case of the interband PL of HgTe CQDs.[67] And this is assigned to the change of the bulk band gap of HgSe.

Figure 3-5 also shows that the intraband PL narrows from 500 cm^{-1} FWHM to 350 cm^{-1} at lower temperatures and its integrated intensity varies surprisingly little across temperatures, by 37% for CdSe, 11% for CdS and 14% for CdTe, without a monotonic relationship between PL intensity and temperature. The lack of thermal activation likely rules out trapping processes for the intraband relaxation.

This is unlike the interband PL which, as shown in Figure 3-5c, does increase by an order of magnitude from 300 K to 80 K, with an initial Arhenius activation energy of 170 cm^{-1}. Such an activated process supports the prior proposal that the interband emission of the core/shell is limited by hole trapping to the outer shell surface.

The low QY in the mid-infrared may arise from a number of other mechanisms. In molecular systems, the "energy gap law" states that the non-radiative relaxation scales exponentially with the transition energy, as $k_{nr} \sim exp - \gamma E$.[130] This accounts for the very low PL efficiency of molecular dyes in the near-infrared. The exponential form has been explained by the Franck-Condon overlap of vibrations between the ground and excited states in the presence of electron-vibration coupling.[130] The absence of temperature dependence implies that the modes are of high energy, and not affected by temperature. While this applies for molecules where the electronic states are strongly coupled to C-C and C-H stretches, it does not apply to HgTe and HgSe if low-frequency

optical phonons are involved. Another mechanism proposed by Cooney et al. is an electron-vibration coupling to outer ligands due to the extent of the wavefunction at the surface.[131] This should lead to an exponential suppression of the coupling with larger shell thickness and it is likely ruled out by the weak effect of the shell. Yet another mechanism is that the relaxation occurs via a polaronic mixing to the internal short-lived optical phonons.[132-133] The experiments reported here will constrain such mechanism. A quantitative model previously applied to the CQDs is the near-field energy transfer to the IR absorbing ligands vibrations.[134-135] Previous studies on HgTe CQD films showed that the interband PL is quenched as it overlaps with C-H fundamental or overtone vibrations.[67] In this model, the non-radiative rate is inversely proportional to the fourth power of the distance between inner core and outer surface.[134-135] In the case of HgTe/CdTe, a size increase of ~12% would enhance the PL by only 57%, consistent with the limited PL improvement observed. For the large tetrahedral HgSe/CdSe core/shell, the surface is still rather close to the HgSe core and therefore coupling to the ligands can still play an important role. For the c-ALD HgSe/CdSe with a size increase of 30%, a 3-fold enhancement could be expected and this is also roughly in line with the observation. This suggests that in order to get another order of magnitude improvement in PL QY, at least 8 more layers need to be grown on the existing core/shell. We note that, at 5 microns, there are no fundamental vibrations for the ligands used here, and the energy must then be transferred to a weak background of overtone and combinations modes.[134]

3.4 Synthesis of HgSe CQDs in Oleic Acid and HgSe/CdSe Tetrapods

As discussed in section 2.3 and 2.6, HgTe CQDs can be synthesized with $Hg(oleate)_2$ and TOPTe at low temperatures, which can later be used to grow *zb*-HgTe/*w*-CdSe tetrapods. Similar approach is used here to synthesize OAcid-capped HgSe and *zb*-HgSe/*w*-CdSe tetrapods.

3.4.1 Synthesis Procedures

The detailed procedures for synthesizing HgSe CQDs in OAcid are shown below:

a. In glovebox, weighed 10 mmol Se powder (Sigma-Aldrich, 99.99%) in a 20 mL vial. 10 mL of TOP (Sigma-Aldrich, 97%) was added and the solution was stirred at room temperature overnight to form a yellow solution. This step is to prepare 1 M TOPSe as Se precursor;
b. Weighed 1 mmol of HgO powder (Sigma-Aldrich, 99%) in a 20 mL glass vial. Added 4 mL of oleic acid (OAcid, Sigma-Aldrich, 90%) and 4 mL of octadecene (ODE, Sigma-Aldrich, 90%). Put the vial on a hot plate inside the glovebox;
c. Set the hot plate temperatures at 125 °C and started stirring. When the actual temperature reached 110 °C, the red color from HgO powder gradually disappeared. It took about 15-20 min for the solution becoming colorless, then stopped heating. This step is to prepare mercury oleate ($Hg(oleate)_2$) as mercury precursor;
d. When the solution was cooled to 45 °C, injected 0.2 mL of 1 M TOPSe. The color turned red and slowly became black. Reacted for 13 h;
e. Took the vial out of glovebox for cleaning. The dots were precipitated by adding a mixture of acetone and ethanol. After centrifugation, the solids were re-dispersed in TCE. The concentration is ~0.02 mmol HgSe/mL TCE. The dots were used as cores for HgSe/CdSe tetrapods synthesis.

The detailed procedures for synthesizing *zb*-HgSe/*w*-CdSe tetrapods are shown below:

a. 10 mmol CdO (Sigma-Aldrich, 99.99%) and 40 mmol OAcid (Sigma-Aldrich, 90%) was added to a flask, which was purged under argon for 15 min. Next, the mixture was heated

at 240 °C for 20 min to dissolve CdO powders. The solution was cooled to 50 °C and poured into 100 mL of acetone. White cadmium oleate solid precipitated out. Rinsed the product with acetone twice and dried it under vacuum for 2 days. The cadmium oleate powder was dissolved in OAcid to make a 0.5 M solution and used as Cd precursor;

b. Took 2 mL OAcid and 4 mL ODE in a 3-neck flask. The flask was degassed under Schlenk line for 1 h. 1 mL of OAcid-capped HgSe TCE solution was injected into the flask and degassed for another 30 min to remove TCE;
c. Flushed the system with argon and kept the HgSe cores under argon for 15 min;
d. 0.6 mL of $Cd(oleate)_2$ solution, 0.3 mL of TOPSe and 5.1 mL of ODE were filled in a 6 mL syringe. Loaded the syringe on a syringe pump. Next, increased the temperature of the flask to 210 °C, started the pump at an injection speed of 1.6 mL/h. When the injection was finished, cooled down the reaction mixture to room temperature and quenched in chloroform;
e. Precipitated the quantum dots with acetone and ethanol followed by centrifugation. Re-dispersed in TCE. The final solution was much darker than the initial HgSe solution despite the same TCE volume.

3.4.2 Properties of Oleic Acid-Capped HgSe CQDs and HgSe/CdSe Tetrapods

The OAcid-capped HgSe CQDs are well separated in TCE solution and spherical under TEM. Figure 3-6 shows a typical TEM image and absorption spectrum of 4.5 nm dots.

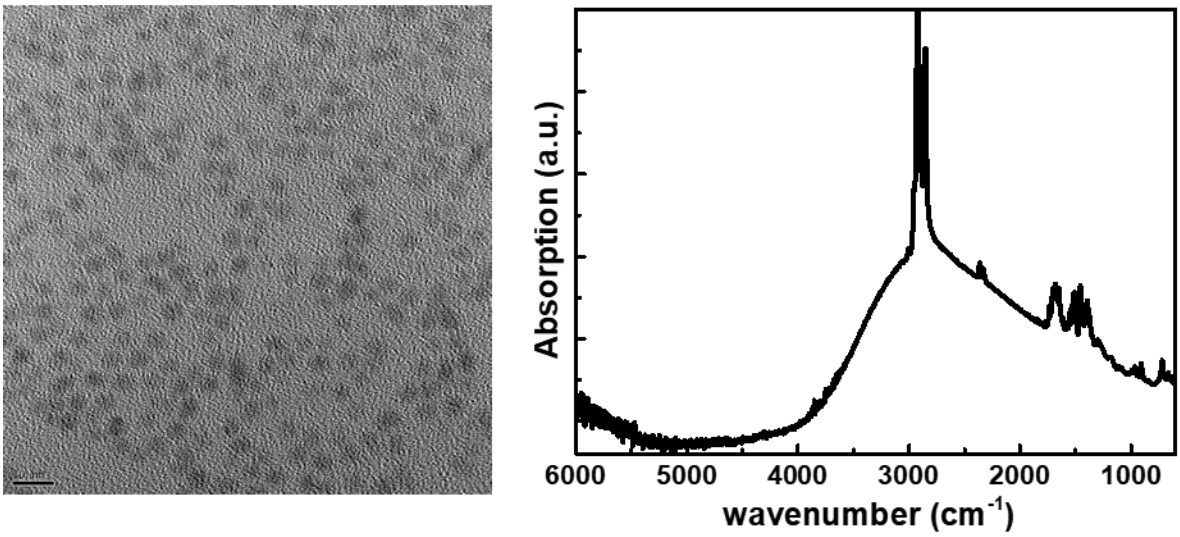

Figure 3-6 *(left) TEM image of OAcid-capped HgSe CQDs (scale bar: 10 nm); (right) ATR-IR spectrum of the same sample measured on ZnSe substrate.*

The absorption spectrum is broader than the substituted selenourea synthesis shown in Figure 3-2. Also, the peak is not symmetric that might have contributions from scattering at the low energy side. The PL is negligible, probably due to the fact that it is on top of the C-H and C=O vibrations from oleic acid.

Similar to *zb*-HgTe/*w*-CdSe, *zb*-HgSe/*w*-CdSe also has a tetrapod morphology with wurtzite arms. The TEM and XRD of the tetrapods are shown in Figure 3-7(a-b).

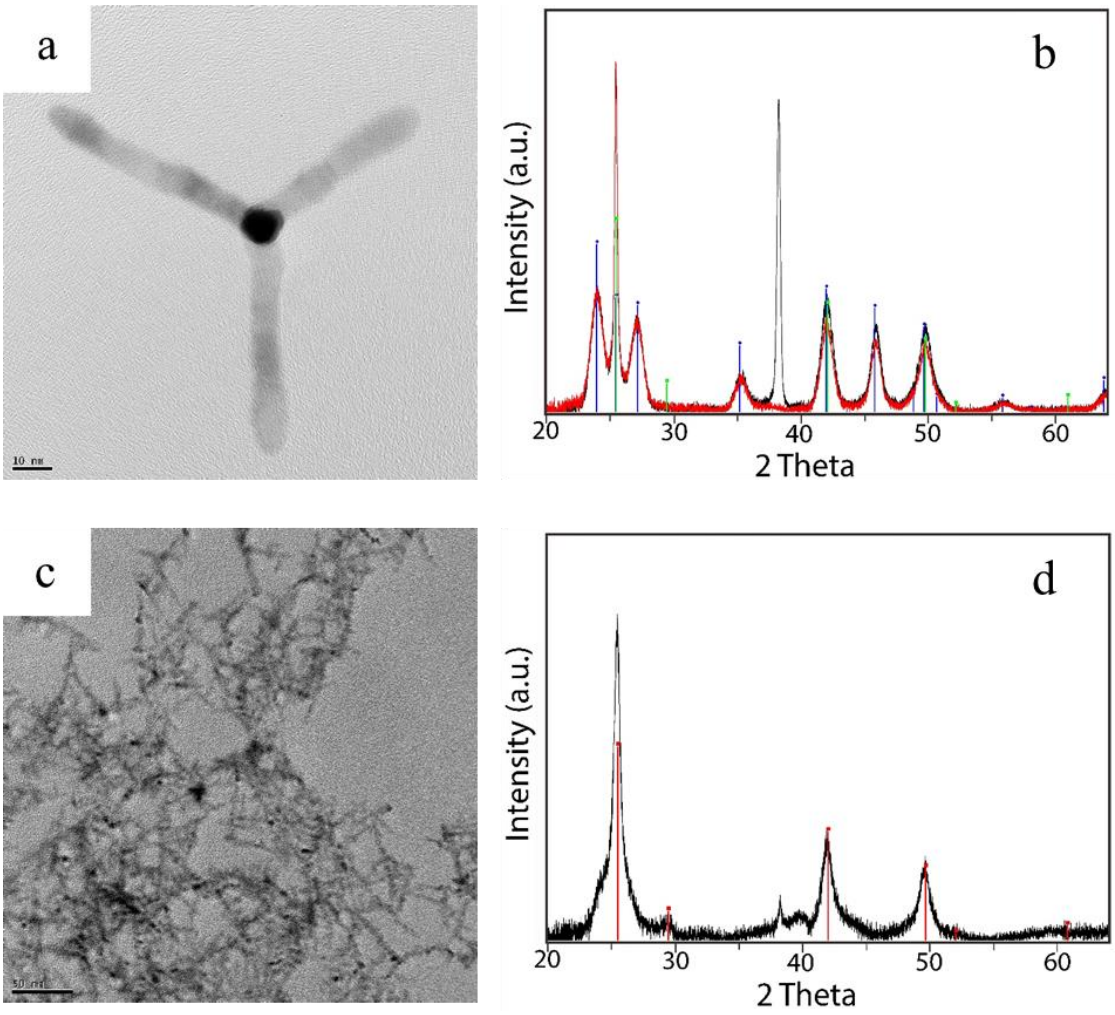

Figure 3-7 *(a) TEM image of zb-HgSe/w-CdSe tetrapods synthesized with TOPSe (scale bar: 10 nm); (b) XRD spectra of zb-HgSe/w-CdSe tetrapods film before (black) and after (red) annealing at 150 °C for 30 min. The blue and green lines indicate the positions of bulk w-CdSe and zb-CdSe, respectively; (c) TEM image of zb-HgSe/zb-CdSe synthesized with Se-ODE (scale bar: 50 nm); (d) XRD spectrum of zb-HgSe/zb-CdSe synthesized with Se-ODE. The red lines indicate the positions of bulk zb-CdSe.*

The XRD spectrum matches the positions of *w*-CdSe (or HgSe), but the high peaks at ~25.5°, 42° and 49° suggest that the *zb*-HgSe cores are still present. Compared with *zb*-HgTe/*w*-CdSe, *zb*-

HgSe/*w*-CdSe tetrapods have more extended arms as long as 100 nm. The width of the arm is ~6-7 nm, larger than the size of HgSe cores, which indicates HgSe is buried beneath a shell of CdSe. This makes the *zb*-HgSe/*w*-CdSe tetrapod thermally stable despite its anisotropy, as proved by the unchanged XRD linewidth after annealing in Figure 3-7b.

In their PbSe/CdSe paper, Jennifer Hollingsworth and co-workers mentioned the choice of Se precursor would determine the final phase of the CdSe shell.[122] The use of Se-ODE resulted in square-shaped *zb*-PbSe/*zb*-CdSe, while TOPSe gave *zb*-PbSe/*w*-CdSe tetrapods. Giving the fact that ODE is a non-coordinating solvent, the presence of TOP is the only difference between these two syntheses. To test this idea, I replaced the TOPSe with Se-ODE as the Se precursor and the results are shown in Figure 3-7(c-d). The Se-ODE based synthesis yields more branched *zb*-HgSe/*zb*-CdSe. The XRD spectrum shows that the heterostructures are pure zinc-blende. This verifies the idea that TOP plays an important role in controlling the phase of CdSe. TOP is a strong binding ligand to metal atoms. As a result, the addition of TOP may slow down the reaction and shift the shell growth from thermodynamically control to kinetically control. Therefore, one may expect to tune the HgSe/CdSe shape and phase by using a mixture of different Se precursors.

3.5 Conclusions

In chapter 3, I reported a synthesis of monodispersed HgSe CQDs as well as two new synthetic methods for HgSe/CdX CQDs. The use of 3-substituted selenourea greatly lowers the precursor conversion rate and makes it possible to better control the nucleation step, which is the key for making monodispersed HgSe CQDs. For HgSe/CdX CQDs, I used both hot-injection and c-ALD methods to grow the shells. The hot-injection of Cd and Se precursors produced large HgSe/CdSe, while c-ALD allowed the growth of CdS, CdSe, and CdTe shells with some thickness control. All

core/shells showed moderate improvements in the mid-infrared PL intensity. At 5 microns wavelength, the brightest emitter is HgSe/CdSe with a quantum yield around 10^{-3} for the intraband $1S_e$-$1P_e$ transitions. The shell increased the intraband PL of the core by about 5 times. I explain the systematic but moderate improvement with the shell and the lack of temperature dependence by the model of a near-field energy transfer from the core to absorbers outside the shells. However, it is also possible that the interfaces grown here are still defective. While this work showed a vastly improved thermal stability of the core/shells, therefore widening the range of possible processing, it highlights the difficulties of achieving bright mid-IR emission with CQDs.

In the last part of chapter 3, I discussed my results on OAcid-capped HgSe and HgSe/CdSe tetrapods. The different results coming from TOPSe and Se-ODE suggest TOP plays an important role in the CdSe phase control.

Chapter 4 Synthesis of HgS CQDs and Core/Shells

In this chapter, the synthesis of HgS CQDs and HgS/CdS core/shells will be discussed, using a special two-phase method. By tuning HgS CQD sizes, a gradual transition from intraband to surface plasmon is observed, which is universal for all heavily-doped CQD systems. Much of the content in this chapter has been published in reference 85.

4.1 Synthesis of HgS CQDs by Two-Phase Method

In a two-phase synthesis, two immiscible solvents are used, each contains one type of precursor (cation or anion). In this case, the mercury precursor is in nonpolar TCE, while sulfide precursor in a polar solvent. The purpose of the two-phase synthesis is to better control the precursors conversion rate by adjusting their concentrations and solvents, which would then yield particles with better monodispersity.

4.1.1 Synthesis Procedures

a. The mercury precursor was prepared by dissolving 0.05 mmol of $HgCl_2$ in 10 mL of OAm and 10 mL of TCE at 100 °C in glovebox. When the white solids were all dissolved, stopped heating and added 0.2 mL of TOP. Without adding TOP, the mercury precursor will turn foggy as it cools down;
b. The sulfur precursor was $(NH_4)_2S$ (Sigma-Aldrich, 40-48 wt% in H_2O). In a typical synthesis, 2 mL of the mercury precursor solution was mixed with 20 μL of $(NH_4)_2S$ diluted in 2 mL of H_2O under vigorous stirring at room temperature. The H_2O can be replaced by

other polar solvents as discussed later in section 4.1.2. After 30 min, the nonpolar phase, which contained the final HgS CQDs, was collected via centrifugation;

c. HgS CQDs were separated from the solution by the addition of methanol and centrifugation. The CQDs were then re-dispersed in TCE for further characterization. For CQDs larger than 6 nm, the addition of DDT prior to precipitation was necessary to obtain a re-dispersible product;

d. To increase the CQDs size, equivalent volumes of the Hg and S precursors were added dropwise to a preexisting HgS CQDs solution. The CQDs were separated and re-dispersed following the same procedure in step c after a desired size was achieved.

e. Extremely large HgS CQDs (size around 15 nm diameter) were obtained by directly adding 20 μL of $(NH_4)_2S$ to 2 mL of mercury precursor and reacting for 15 h. The CQDs were separated and re-dispersed as described in step c. All the CQDs were obtained under ambient conditions (20 °C and exposed to air).

4.1.2 Effect of Different Synthetic Parameters on HgS CQDs

In a two-phase synthesis, two immiscible solvents are used. This phase separation between reagents was explored in order to achieve a more controlled growth of the CQDs.

All syntheses in section 4.1.1 were done under ambient conditions. No significant change in particle morphology and optical properties has been observed when did the experiment in glovebox, as shown in Figure 4-1.

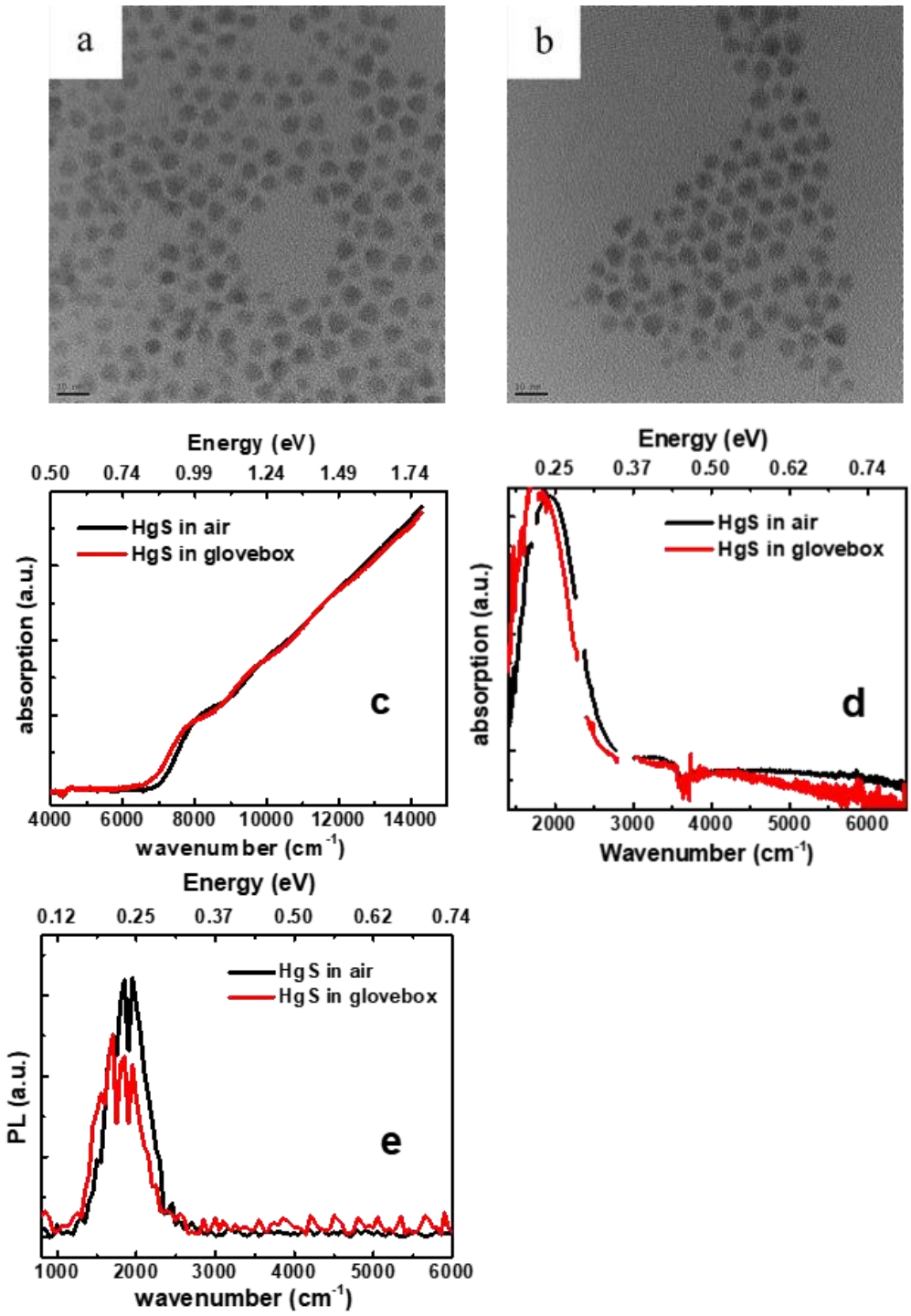

Figure 4-1 *TEM images of HgS synthesized (a) under ambient conditions and (b) under N_2; (c) Interband absorption, (d) Intraband absorption and (e) PL spectra of HgS synthesized in air or in N_2. The interband absorption spectra were obtained after sulfide treatment and the intraband absorption spectra were obtained as synthesized.*

However, slightly increase the reaction temperatures would result in larger particles with much worse size dispersion, as shown in Figure 4-2. This indicates Ostwald ripening dominates at higher temperatures.

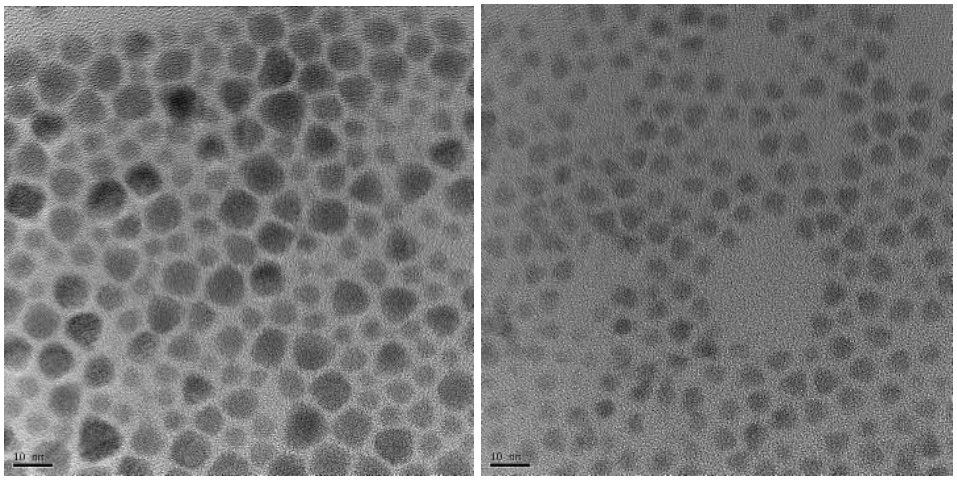

Figure 4-2 *TEM images of HgS CQDs synthesized at 40 °C (Left) and 20 °C (Right). The same Hg:S ratio (1:30), reaction time and solvents (H_2O) were used in these two syntheses.*

Besides environmental conditions, the three main factors that affect the size and shape of the final products are the relative amount of $HgCl_2$ and $(NH_4)_2S$ precursor, the polar solvent that dissolves the $(NH_4)_2S$, and the reaction time.

To study the effect of the precursor amount, H_2O was used as the polar solvent that dissolved the $(NH_4)_2S$ precursor. By varying the Hg:S precursor ratio from 1:2 to 1:30, the HgS CQDs' sizes can be tuned from 2.9 nm to 5.7 nm diameters with a size distribution of less than 8%. This is a significant improvement over the previous hot-injection method using thioacetamide, where the size distribution was 20%.[11] Larger particles are grown by subsequent addition of reagents.

To study the effect of different solvents, the same 1:30 $HgCl_2$: $(NH_4)_2S$ precursor ratio and reaction time (30 min) were used, with 20 μL of $(NH_4)_2S$ dissolved in 2 mL of different solvents. The results are summarized in Table 4-1 and the TEM images of these HgS CQDs synthesized using different solvents are shown in Figure 4-3.

Table 4-1 Summary of the solvents and HgS CQD size and morphology

Solvents	Dielectric constant	Size and morphology
formamide (FA)	111	12.1 nm, tetrahedral
H_2O	80	5.7 nm, spherical
1:1 FA:ethanol	~70	9.8 nm, tetrahedral
propylene carbonate	64.9	15.3 nm, tetrahedral
DMSO	46.7	aggregated dots
Acetonitrile	37.5	precipitate
Ethanol	24.5	precipitate
n-butanol	17.7	precipitate

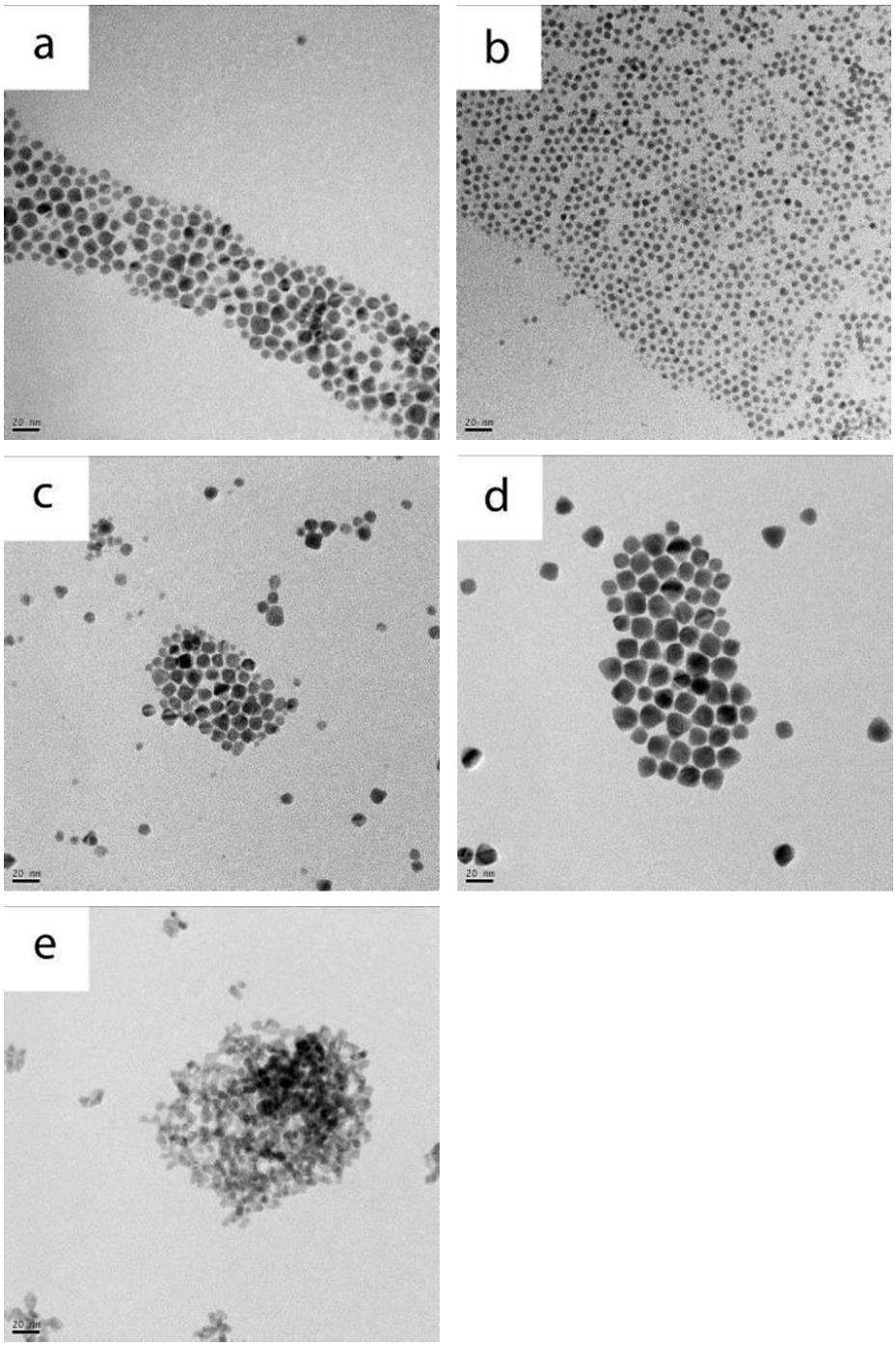

Figure 4-3 *TEM images of HgS CQDs using (a) FA; (b) H_2O; (c) 1:1 FA:ethanol; (d) Propylene carbonate; (e) DMSO as the solvent for $(NH_4)_2S$.*

Table 4-1 and Figure 4-3 show a clear correlation between the dielectric constant and the final HgS product, where solvents with a dielectric constant higher than DMSO can yield CQDs without aggregation. We propose that these results arise from the partition of $(NH_4)_2S$ between the polar and nonpolar phases. Varying the dielectric constant affects the partition since the solubility of polar molecules are loosely correlated to the solvent dielectric constant even though there is no simple monotonic relationship between them.[136] With $(NH_4)_2S$ in solvents more polar than DMSO, the partition of $(NH_4)_2S$ in the nonpolar phase is smaller, therefore slowing down the reaction rate and allowing controlled growth of the CQDs. Solvents less polar than DMSO, such as acetonitrile and ethanol, are miscible with the nonpolar phase and this leads to uncontrolled precipitation. The partition mechanism is further supported by a control experiment of dissolving Na_2S instead of $(NH_4)_2S$ in the polar solvent, where no reaction happens. This is because Na_2S, unlike $(NH_4)_2S$, exists only in ionic form in the polar solvents, and thus cannot transfer to the nonpolar phase. Although the partition of the polar reagent is related to the dielectric constant, the CQD size and dispersity must also depend strongly on the kinetics of phase transfer. This would be affected by the size of the polar/nonpolar domains and the diffusion rate of precursors in polar/nonpolar solvents, and thus cannot be predicted using dielectric constant alone.[48, 137]

As expected from the classical model of uniform growth followed by Ostwald ripening, the reaction time also affects the HgS CQDs sizes and dispersity. Therefore, while the HgS CQDs size increases constantly at early times, the size distribution becomes worse at longer times. An example of such ripening after a period of growth is shown in Figure 4-4.

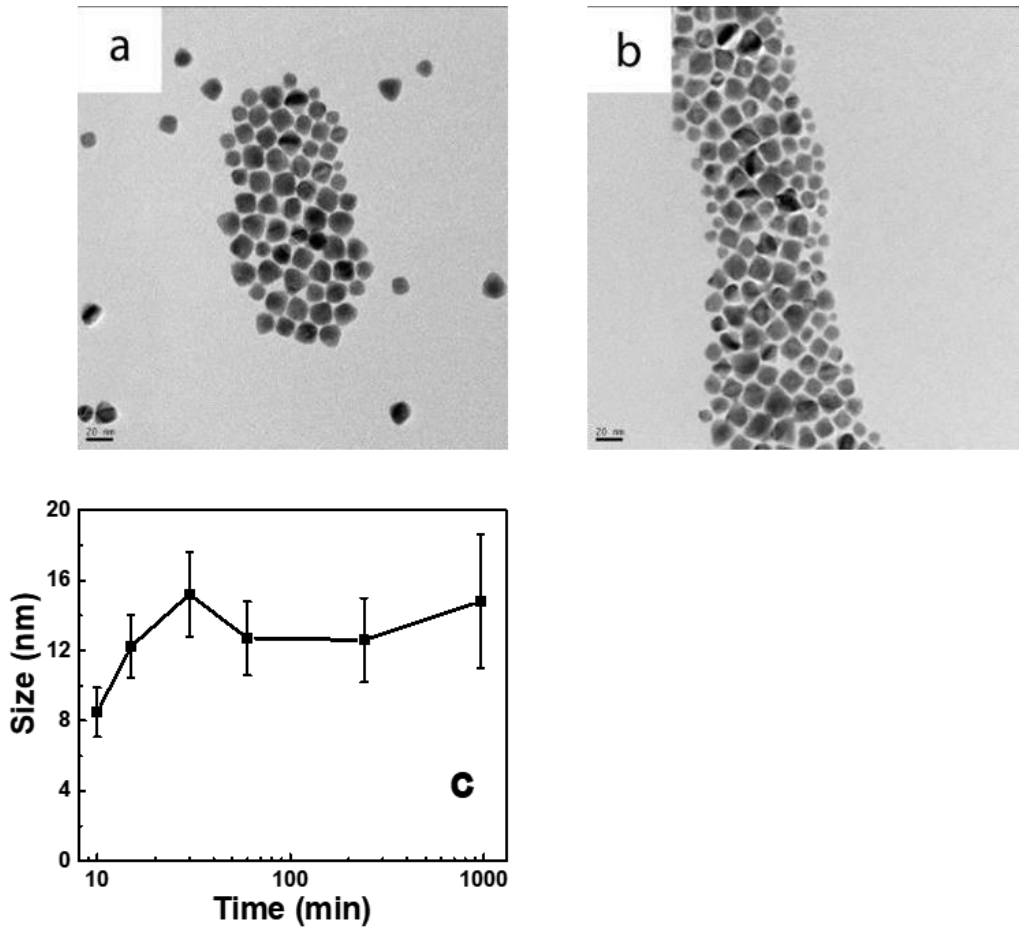

Figure 4-4 *TEM images of HgS CQDs with (a) 30 min; (b) 16 h reaction times; (c) A plot of the CQD sizes with time (x-axis is in log scale). The error bars are the standard deviations of the particle size distributions. The data show uniform growth at early times followed by a stable mean size but broadening distribution at longer times. The sulfur precursor was 20 μL of* $(NH_4)_2S$ *dissolved in 2 mL of propylene carbonate and the Hg:S ratio is 1:30.*

Overall, the ambient synthesis of the HgS nanocrystals, using two immiscible solvents as the reagents, provides a versatile way to obtain a wide range of sizes of the HgS nanoparticles with small size dispersion. In the following, we used water for the polar phase to obtain HgS CQDs

ranging from 2.9 nm to 14.5 nm diameters with size distribution within 10%. The TEM images are shown in Figure 4-5.

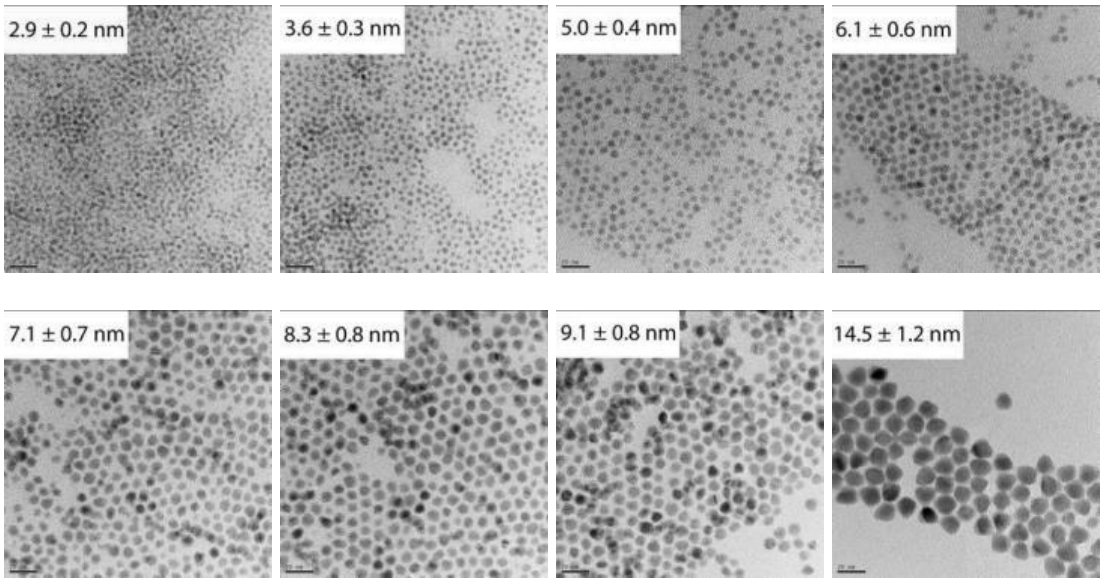

Figure 4-5 *TEM images of HgS CQDs with sizes ranging from 2.9 nm to 14.5 nm.*

HgS has two common crystal structures. One is the room temperature stable bulk form of α-HgS, the other is β-HgS (zinc-blende structure). The HgS CQDs exhibit the zinc-blende structure and the grain size calculated from the XRD linewidth using the Scherrer equation $0.9\lambda/\beta\cos\theta$ is consistent with the TEM results.

4.1.3 Optical Properties of HgS CQDs

Like HgSe, the synthesized HgS CQDs have air-stable n-doping and intraband absorption. To obtain the interband absorption spectrum of HgS, a solution-based sulfide treatment needs to be used. For a typical suifide treatment, 1 mL of HgS TCE solution which had an interband shoulder absorption around 0.1 O.D./cm was put into a test tube. 1 mL of formamide, 50 μL of oleylamine

and 150 μL of 0.1 M $(NH_4)_2S$ in formamide were added into the test tube, stirred for 8 min and the bottom layer (TCE) was kept. Formamide was used to wash the bottom layer twice to remove excess $(NH_4)_2S$. The solution is ready for measurements. The addition of oleylamine is necessary to keep the dots in the TCE phase.

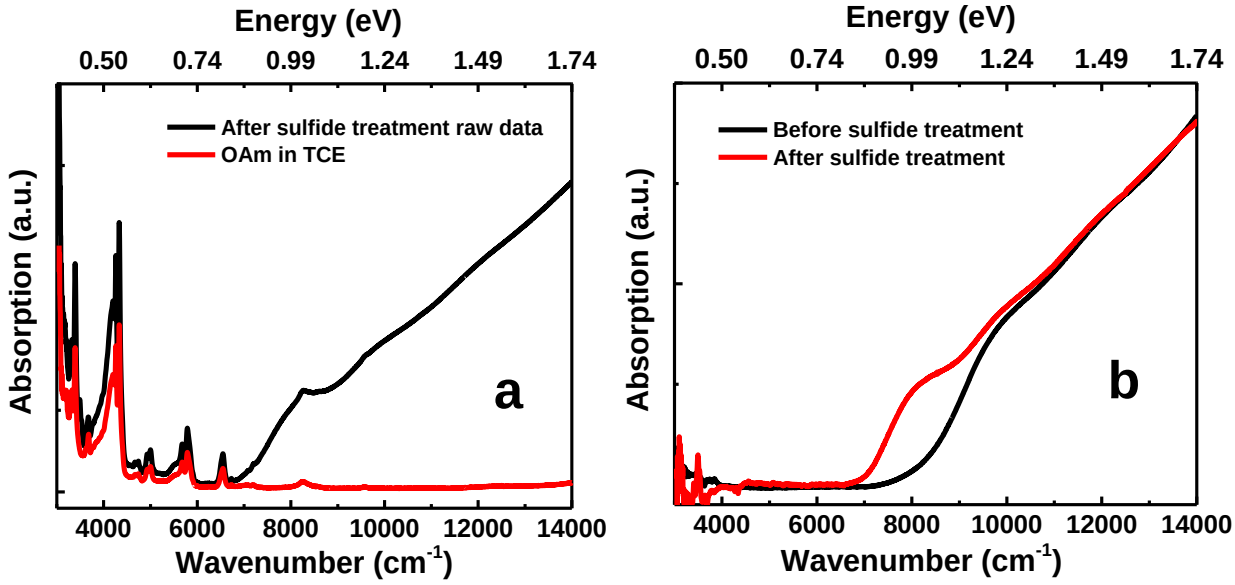

Figure 4-6 *(a) Raw data of interband absorption of 5.7 nm HgS quantum dots after sulfide treatment (black) and reference spectrum of OAm in TCE (red); (b) Interband absorption spectra of 5.7 nm HgS quantum dots before and after sulfide treatment, after substracting the OAm spectrum.*

Figure 4-6a shows the raw data of the interband absorption spectrum of 5.7 nm HgS quantum dots after sulfide treatment. There are several peaks due to the excess oleyamine in the solution. To clean the spectrum, an OAm (in TCE) reference is subtracted from the raw data. The results are shown in Figure 4-6b. After the sulfide treatment, the HgS shows a clear exciton feature at ~7500 cm^{-1}, which is not present before treatment. The sulfide treatment is therefore used to undope the

HgS CQDs and obtain their interband absorption spectra. The absorption and PL spectra are shown in Figure 4-7 for HgS CQDs of different sizes.

As synthesized, the HgS CQDs exhibit a strong intraband absorption, as shown in Figure 4-7a, indicating that they are n-doped. They also show intraband PL (Figure 4-7b) with no interband PL detected. Both intraband absorption and PL energies decrease monotonically with increasing particle size, such that, across the size range (2.9−14.5 nm), the intraband absorption peak tunes from 2600 cm^{-1} to 1000 cm^{-1}. The tuning of the intraband PL is smaller, likely limited by the energy transfer to ligands vibrations as for HgSe. As reported previously, the doping effects are primarily assigned to surface modifications which change the electrostatic environment and the absolute positions of the states of the quantum dots.[11] Figure 4-7c shows the interband absorption spectra after sulfide treatment for the range of dots sizes where the intraband absorption is eliminated.

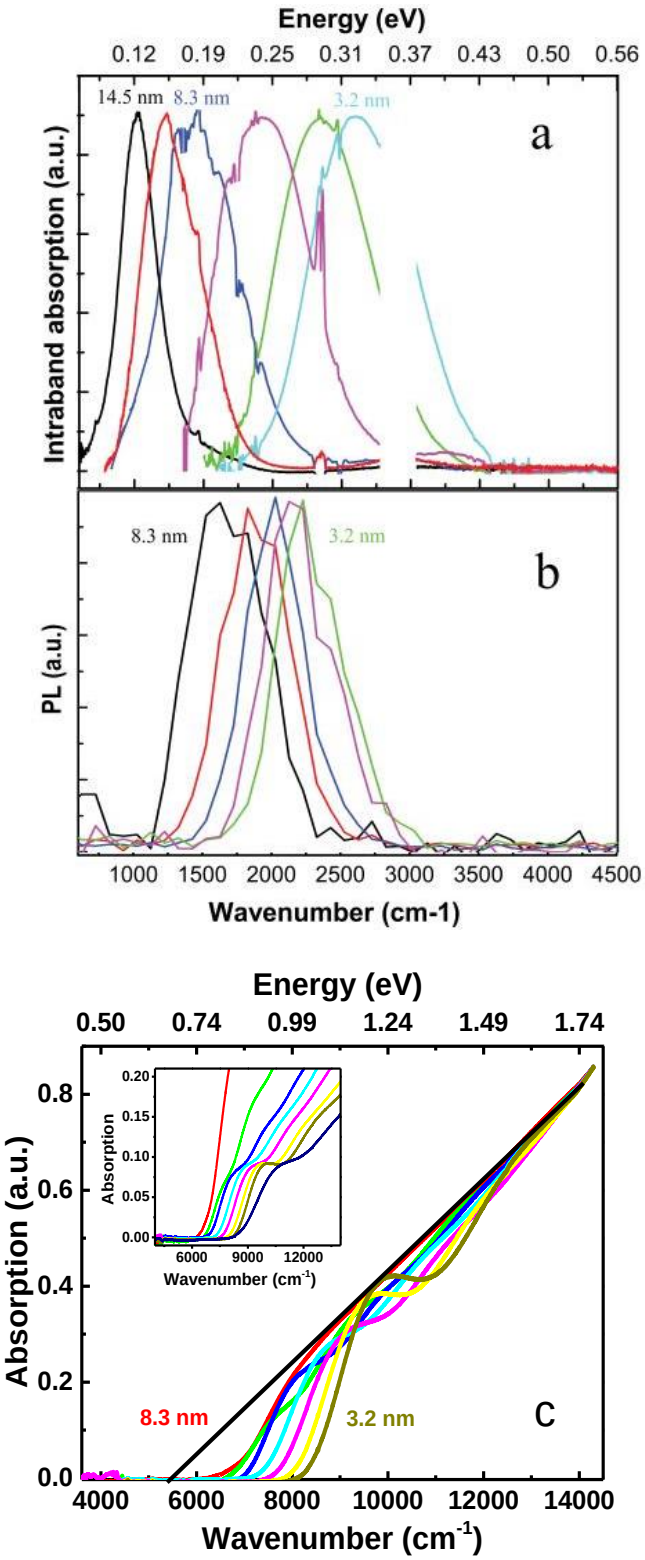

Figure 4-7 *Normalized spectra of HgS CQDs of different sizes: (a) intraband absorption measured on film; (b) PL spectra measured in solution; (c) Interband absorption after sulfide treatment*

Figure 4-7, continued

normalized at high energy (inset: same plot normalized at first exciton shoulder), measured in solution. The solid black line is an extrapolation of the absorption at higher energies and the x-intercept is an estimate of the bulk gap of 0.67 eV.

4.1.4 HgS Band Gap and Doping Density

Band gap:

In spite of the experimental and theoretical efforts that have been made, there has been no consensus about the bandgap of β-HgS, with both positive and negative values reported.[12-14] The experimental difficulties are due to the instability of β-HgS in bulk form and the strong natural doping of β-HgS thin films.[138] A previous report on β-HgS CQDs gave a value of ~0.6 eV based on the correlation of the interband and intraband bleach and a $k \cdot p$ model.[11] The interband optical data reported in Figure 4-7 cover a wider range with better size control and they provide new and more direct information about this bandgap. The interband absorption spectra of HgS, shown in Figure 4-7c, are characteristic of positive direct bandgap semiconductors with strong absorption at the band edge and a rapid drop at low energy.[139] By normalizing the spectra at the highest energy recorded, we get an approximate normalization of the optical absorption per volume. It is then clear that, as the size increases, the absorption is asymptotically vanishing at a finite energy, indicating a positive bandgap value. As a first estimate of the gap, we tentatively use the *x*-intercept of the black line in Figure 4-7c which gives a bandgap around 5400 cm^{-1} (0.67 eV), in fair agreement with the previous value.[11] Another approximate determination is to use the points where the interband absorption is about 1% of the absorption at 14000 cm^{-1}. On a log scale, the absorption drops precipitously below some cut-off energy and the 1% point is in the range where the slope is

~ one decade/60 meV, where absorption involves phonons below the optical gap of the dot. This cut-off energy converges approximately to 0.68 eV at large sizes. There remain significant errors and the gap could be smaller since the larger dots could not be undoped. We therefore propose a value of 0.65 $\pm$ 0.05 eV for the bulk bandgap of β-HgS. This value is close to a determination of the optical gap of 0.54 eV for evaporated β-HgS.[138] It also agrees with one theoretical calculation using the QSGW method, which predicts a bandgap of 0.61 eV and a small spin-orbit splitting of -0.06 eV.[14] The small spin orbit splitting is likely the reason why the spectra of HgS nanocrystals are similar to those of CdS nanocrystals, in terms of showing a weaker first excitonic peak compared to CdSe and HgSe nanocrystals with similar size dispersion.

Relationship between intraband and interband absorption spectra:

Because of their better size dispersion, the undoped interband spectra of the 3−6 nm diameter HgS nanocrystals show several features (Figure 4-8a). The energies of the features are extracted by using a smooth baseline and several Gaussian functions, as shown in Figure 4-8b, and their values are shown in Figure 4-8c for the 3−6 nm diameter range. The features should correspond to excited states of HgS CQDs. Assigning the first and second peaks to 1S and 1P excitons, we find that their energy differences match very well the intraband energies, as shown in Figure 4-8d. Therefore, within the 3−6 nm diameter range, the intraband absorption is assigned to the $1S_e-1P_e$ transition, which is in agreement with previous results.[11]

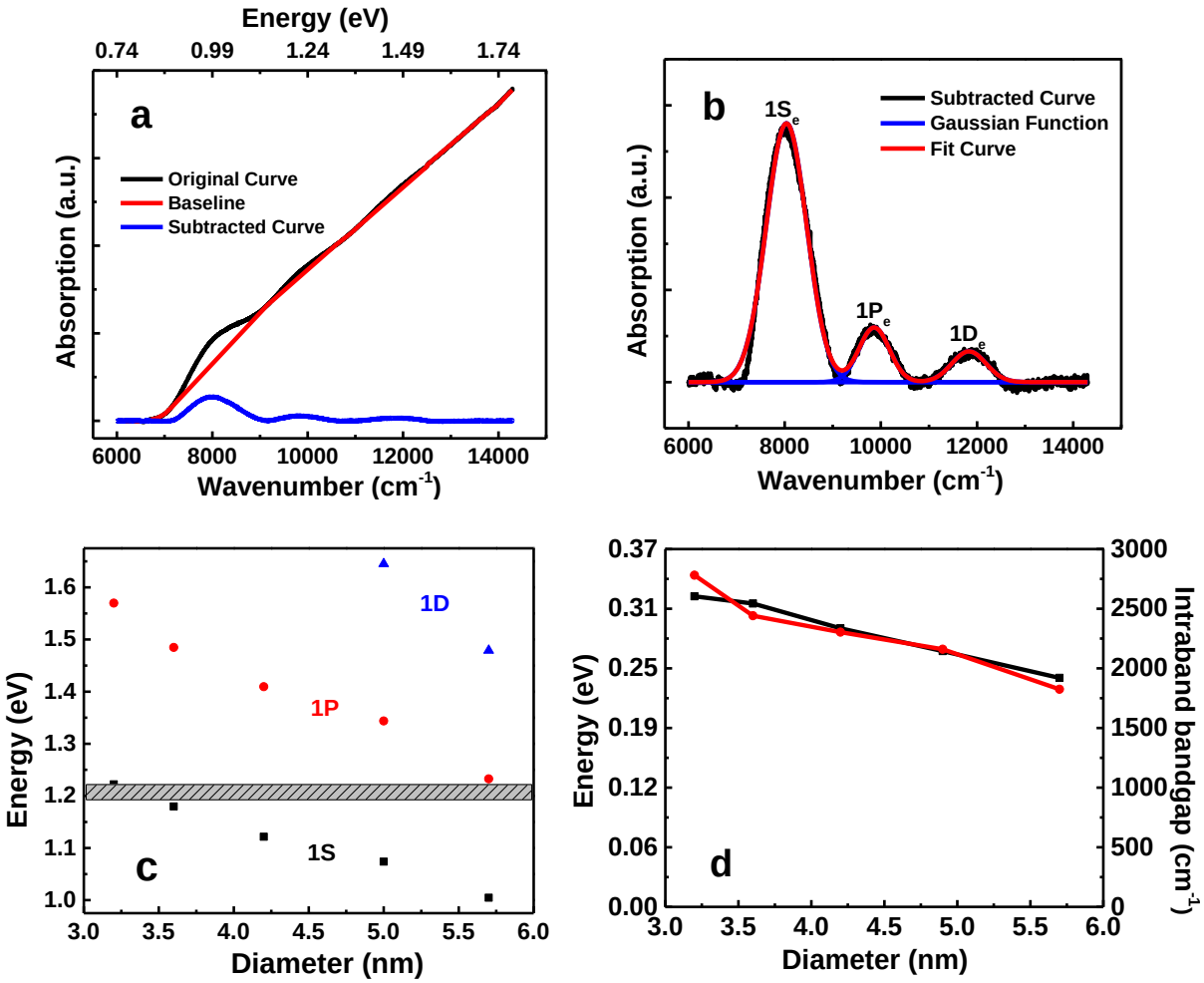

Figure 4-8 *(a) Optical absorption of 5.7 nm HgS CQDs after sulfide treatment (black), baseline (red) and subtracted curve (blue); (b) Subtracted curve fitted with three Gaussian functions; (c) Peak energies versus particle size; The dashed area represents the possible Fermi level range, where the $1S_e$ state has ~2 electrons and the $1P_e$ state is empty across the size range; (d) Intraband absorption energy (black) and energy difference between the first two interband features (red).*

Doping density:

The doping density is calculated from the interband absorption spectra of HgS CQDs before and after the sulfide treatment. Figure 4-9 shows the results from 5.7 nm HgS CQDs.

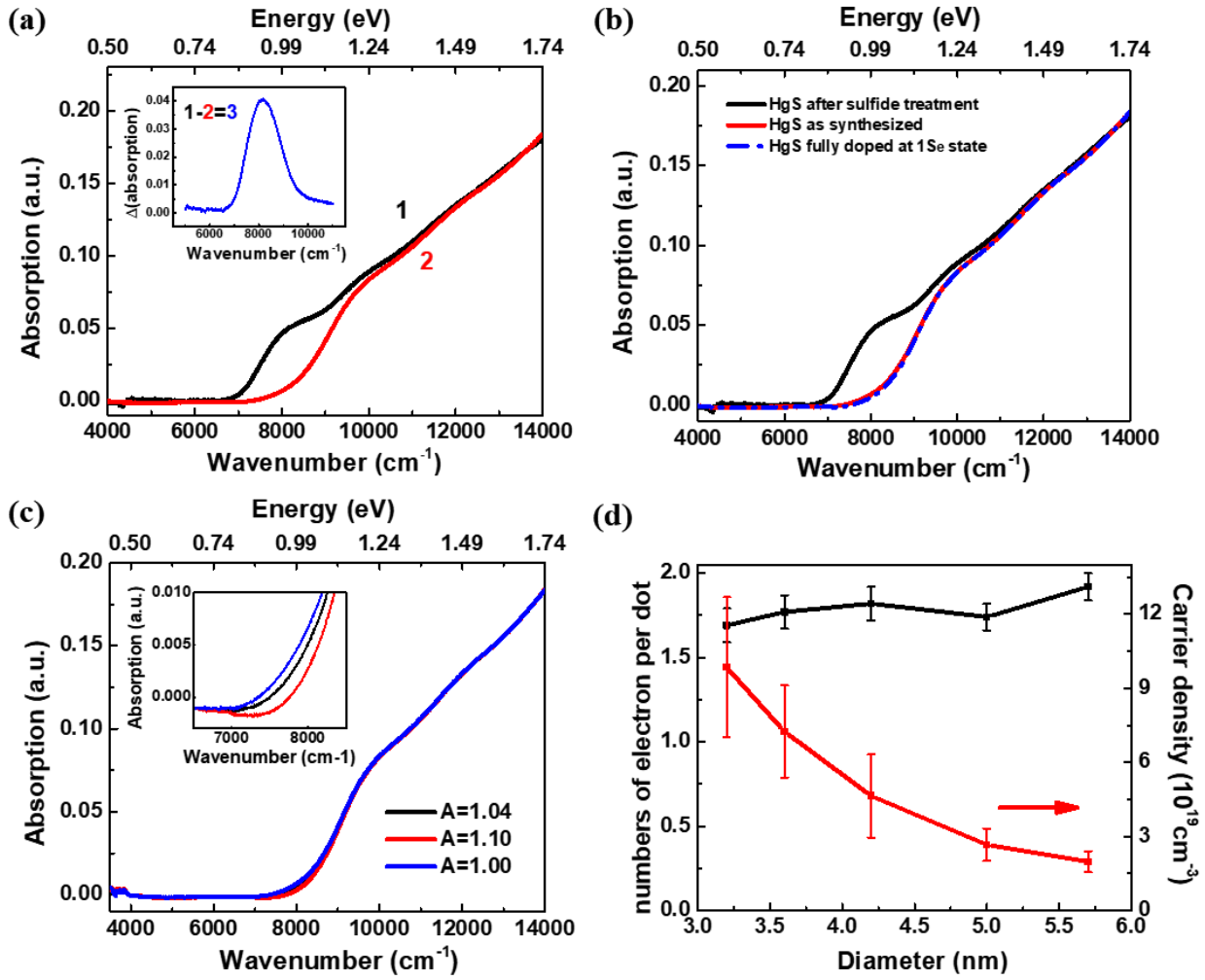

Figure 4-9 *(a) Interband absorption of HgS particles before (red) and after (black) sulfide treatment. Inset: the curve from the subtraction of black and red lines, representing the optical absorption from $1S_e$ state; (b) Derived absorption of HgS fully doped at $1S_e$ state (dashed blue line); (c) Derived absorption of HgS fully doped at $1S_e$ state with different A values (inset: zoom in of the absorption curves); (d) Number of electron per dot (black line) and carrier density (number of electron per volume, red line) with different HgS particle sizes as synthesized.*

Figure 4-9a is the same as Figure 4-6b, where the red line is the absorption of HgS CQDs as synthesized and the black line after sulfide treatment. The difference of the two curves comes from

the result that sulfide treatment undopes the $1S_e$ state of the HgS CQDs. The subtraction between these two absorption spectra results in the blue curve in the inset (curve 3), which accounts for the spectral change due to the difference in doping. We note that it shows a single peak as expected if only the $1S_e$ state occupation is modified. The next step is to subtract the blue curve in Figure 4-9a from the black curve as much as possible to completely bleach the 1S exciton. The result is shown as the dashed blue line in Figure 4-9b. The relationship is as followed:

$$HgS\ fully\ doped\ curve = curve1 - A * curve3$$

here A is the subtracting parameter. In this case, $A = 1.04$.

The $1S_e$ peak position comes from the Gaussian fitting of the subtraction. The fitting peak is 8237 cm^{-1} in this case. Therefore, the final doping density is:

$$\text{Number of } e^- \text{ per dot} = 2 \times \frac{\text{Abs(black, 8237 cm}^{-1}\text{) - Abs(red, 8237 cm}^{-1}\text{)}}{\text{Abs(black, 8237 cm}^{-1}\text{) - Abs(blue, 8237 cm}^{-1}\text{)}}$$

where Abs(black/red/blue) is the absorbance from black/red/blue spectrum in Figure 4-9b. The calculated result is 1.92 e^-/dot, which is the natural doping density of 5.7 nm HgS CQDs as synthesized.

The error of this method comes from two factors. First, there is the choice of the subtracting parameter A. In our method, A could be determined within 0.1. As shown in Figure 4-9c, the red curve shows an unphysical decrease in absorption around 7500 cm^{-1}, which is a sign of over-subtraction. The blue curve is under-subtraction and could subtract further to get the black curve. As a result, the error from different A values is $\pm$ 0.1 e^-/dot.

Another source of error comes from the line width of the Gaussian fitting for curve 3. The FWHM of curve 3 covers wavelength from 7500 cm^{-1} to 8900 cm^{-1}. And within this range, the deviation of doping density is less than $\pm$ 0.01 e^-/dot. As a result, this error is negligible compared with the

error coming from the uncertainly of A. The combined error is then $\pm$ 0.1 e^-/dot, which also applies to other sizes using similar calculation process.

Based on the calculation above, Figure 4-9d shows that the doping density of HgS CQDs is close to 2 electrons per dot and stays stable between $(1.7-1.9) \pm 0.1$ electrons per dot for sizes between 3 and 6 nm. However, the same method is not applicable for larger dots because the excitonic peaks are no longer clearly defined and the sulfide treatment does not eliminate the n-doping.

An ambient doping of $\sim$2 electrons per dot implies that the Fermi level of the environment is higher than $1S_e$ and lower than $1P_e$. Using the excitons energies as measures of the $1S_e$ and $1P_e$ states energies, a range of the environmental Fermi levels can then be derived to allow for the stable doping, as shown in Figure 4-8c as dashed area. A recent electrochemistry study showed a similar Fermi level position within the size range.[64] At large sizes the doping density trends towards 2×10^{19} cm^{-3} (Figure 4-9d). Natural n-doping in thin films of β-HgS is well known, and a previous study on evaporated β-HgS thin films gave a doping density range from 1.46×10^{18} to 2.92×10^{19} cm^{-3}, encompassing our experimental result.[138]

4.1.5 Transition from Intraband to Surface Plasmon Resonance

In recent years, several highly doped semiconductor nanocrystal systems such as ZnO, Silicon and Cu_2S have shown intense infrared absorptions at energies below the gap and these have been assigned to surface plasmons.[140-144] Given the traditional definition of a plasmon as a collective excitation of electrons,[145] Kreibig and co-workers discussed early on how a surface plasmon resonance blue-shifts for small metal particles as a result of size quantization, and reported optical data on silver particles.[146] Schatz and co-workers performed calculations on Ag clusters and found that high symmetry tetrahedral clusters with increasing sizes exhibit a transition from discrete

electronic states to plasmons.[147] They suggested that it is through clumps of degenerate transitions that a collective plasmon mode might emerge. Dionne and co-workers observed a blue shift of the surface plasmon resonance for individual small silver metallic particles by electron energy loss spectroscopy.[148] They assigned the blue shift to quantum confinement and coined the term "quantum plasmon". Schimpf and co-workers proposed further that electronic transitions become surface plasmon resonances whenever they are strong enough to modify the dielectric constant such that its real part become $-2\varepsilon_m$ where ε_m is the matrix dielectric constant.[149] In a study using time-dependent DFT, the classical surface plasmon resonance emerged as the number of carriers increases, and the intraband transitions were renamed "quantum plasmonic resonances".[150] A phenomenological relation between single electron transition and the plasmon frequency was also proposed. Jain studied and derived the same result using a classical model and showed also a gradual evolution from single electron to collective excitations as the carrier density increased.[151] In this section, we analyze the size dependence of the HgS CQDs infrared absorption to determine how the excitation evolves from an intraband transition to a surface plasmon resonance as the particle size increases.

The size-dependence of HgS intraband optical absorption is shown in Figure 4-10a and 4-10b. The effective mass model in an infinite spherical well predicts the energy of the $1S_e-1P_e$ transition as $\frac{\hbar^2(4.49^2-\pi^2)}{2m^*R^2}$, thus linear with $1/R^2$, where R is the radius of the particle. This model clearly fails to capture the experimental behavior, as shown in Figure 4-10b. A simple two-band $k \cdot p$ model might then account for non-parabolicity,[152] with a conduction band dispersion given by:

$$E = \frac{1}{2}\left(\frac{\hbar^2 k^2}{m_0} - E_G\right) + \sqrt{\frac{\hbar^2 k^2}{2m_0}E_P + \frac{E_G^2}{4}} \qquad (1)$$

where E_G is the gap and E_P is the Kane parameter. The zero of energy is the minimum of the conduction band. For small wavevectors, this recovers the parabolic dispersion with $m^* = m_0/\left(1 + \frac{E_P}{E_G}\right)$ at the bottom of the conduction band. Although little is known about the band structure of β-HgS, the low energy dispersion of the conduction band should be well captured by Eq. (1) with appropriate parameters.

The value of E_P is remarkably similar for several II-VI and III-V semiconductors at around 20 eV but smaller values have been reported for β-HgS[152]: fitting Eq. (1) to a theoretical dispersion by Svane and co-workers gives $E_P = 9$ eV.[14] Using a reported effective mass of $m^* = 0.055$ and the gap of 0.54 eV[138] also gives $E_P \approx 9$ eV. We use E_G = 0.65 eV and several values of E_P to fit the intraband energy vs size with Eq. (1). However, as shown in Figure 4-10b, the size variation is still poorly captured by the $k \cdot p$ model for any choice of E_P, both for large and small sizes.

At small sizes, the tuning with size is much weaker than expected, indicating that confinement is not effective or that the dispersion deviates strongly from Eq. (1). Several reasons could account for the deviations at small sizes, which include the deviation from ideal spherical infinite well, the occurrence of surface states above the gap, a difference in stoichiometry for small particles, and also the limited validity of Eq. (1) at high energies. There is indeed no verified data for the bulk conduction band dispersion of β-HgS. The calculation that gives a reasonable gap does not provide the dispersion curve for kinetic energies larger than 0.12 eV.[14] Therefore, it is unknown how well Eq. (1) describes the energy dispersion at higher energies. In particular, the band has another minimum as *k* approaches the L-point, and a low L-point minimum could lead to a weak tuning of the intraband transition at small sizes.

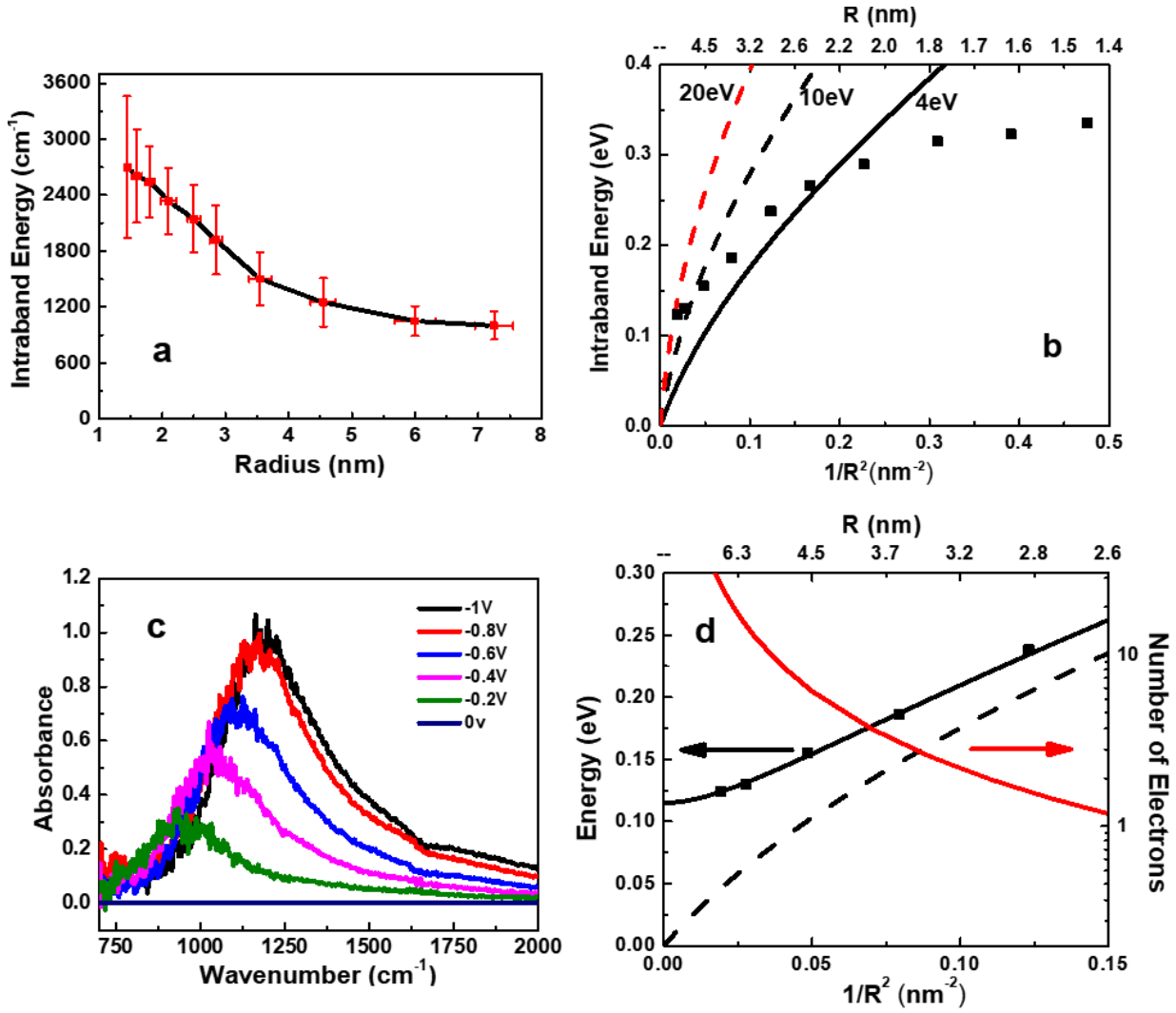

Figure 4-10 *(a) Intraband energy of different sizes HgS CQDs. The vertical error bar is the FWHM of the resonance and the horizontal error bar is the radius standard deviation; (b) Infrared absorption peak energy versus* $1/R^2$*. The lines are three predictions with different Kane parameter based on* $k \cdot p$ *model; (c) Difference spectra of 14.5 nm HgS CQDs under increasingly negative bias vs Ag/AgCl. The spectrum at 0 V is used as the reference; (d) Surface plasmon correction (solid black line) to the* $k \cdot p$ *model (black dashed line) and experimental intraband energy (squares) versus* $1/R^2$*, calculated number of electrons per dot (red line) for the density of* 1.6×10^{19} cm^{-3}.

The deviation at large sizes is a concern as well. The infrared transition settles to a non-zero value of ~1000 cm^{-1}, instead of trending to zero as expected from the vanishing quantum confinement. This observation is similar to a previous report on photocharged n-doped ZnO nanocrystals, where the intraband absorption was assigned to a surface plasmon resonance.[149, 153] Similarly, we propose that the resonance for the large HgS particles is associated with a plasmon resonance due to n-doping. In qualitative support of this assignment, Figure 4-10a shows a significant narrowing of the resonance at large size with a FWHM of 300 cm^{-1} for the 15 nm particles. The spectroelectrochemistry result in Figure 4-10c further shows that the absorbance increases and the peak position blue shifts under more reducing potentials, as expected for a plasmon resonance with an increasing carrier density.

Assuming a spatially uniform resonant polarization inside the sphere, as an approximation to a $1S_e-1P_e$ intraband transition, the dielectric constant is given by $\varepsilon = \varepsilon_{IB} + 4\pi \frac{A}{\omega_0^2-\omega^2+i\gamma\omega}$, where ε_{IB} is the material's real dielectric constant due to all interband transitions. The parameter A is related to the intraband oscillator strength f by $VA = f\frac{e^2}{m_0}$ in CGS units, where V is the nanocrystal volume and m_0 is the free electron mass. Solving for $Re(\varepsilon) = -2\varepsilon_m$ gives a quadratic equation for the frequency.[149] To obtain real solutions, there is a minimum oscillator strength required such that $\frac{2\pi A}{\varepsilon_{IB}+2\varepsilon_m} > \gamma\omega_0$. There are then two solutions, one in the anomalous dispersion regime, and the other further blue shifted.[149] Thus, directly solving for $Re(\varepsilon) = -2\varepsilon_m$ has two consequences: first, an unphysical result of two resonances arising, where there was only one; and second, an oscillation strength threshold. Instead, as pointed out by Jain, the evolution from intraband to surface plasmon resonance is smooth if one considers the effect of the local field.[151]

The internal field in response to an external uniform field E_0 is given by $E = \frac{3\varepsilon_m}{\varepsilon+2\varepsilon_m}E_0$. Expressing the resonant polarization as $P = \frac{\varepsilon-\varepsilon_{IB}}{4\pi}\left(\frac{3\varepsilon_m}{\varepsilon+2\varepsilon_m}\right)E_0$ gives $P = \frac{A}{\omega_0^2-\omega^2+i\gamma\omega}\left(\frac{3\varepsilon_m}{\varepsilon+2\varepsilon_m}\right)E_0$. After rearrangement:

$$P = \frac{A}{\omega_0^2+\frac{4\pi A}{\varepsilon_{IB}+2\varepsilon_m}-\omega^2+i\gamma\omega}\left(\frac{3\varepsilon_m}{\varepsilon_{IB}+2\varepsilon_m}\right)E_0 \qquad (2)$$

The resonance is now blue shifted to $\omega_0' = \sqrt{\omega_0^2 + \frac{4\pi A}{\varepsilon_{IB}+2\varepsilon_m}}$. Using $f = m_0/m^*$, this can be also written as:

$$\omega_0' = \sqrt{\omega_0^2 + \omega_{sp}^2} \qquad (3)$$

where $\omega_{sp}^2 = \frac{4\pi e^2}{m^*}\frac{1}{V}\frac{1}{\varepsilon_{IB}+2\varepsilon_m}$. ω_{sp} is therefore also the surface plasmon resonance of a sphere containing a density $1/V$ of free electrons of mass m^*. Eq. (3) was derived previously by Jain and discussed in the context of carriers with a given effective mass.[151] In its simplest form, the effect arises from the local field that smoothly blue shifts the transition frequency towards the quadratic mean of the frequency and the surface plasmon resonance defined for the density of electrons. If $\omega_0 = 0$, as for free electrons, $\omega_0' = \omega_{sp}$ and one recovers the usual surface plasmon frequency for a metallic sphere of dielectric constant $\varepsilon_{IB} - \frac{\omega_p^2}{\omega^2}$, where $\omega_p^2 = \frac{4\pi e^2}{m^*}\frac{1}{V}$. We note that the shift is a classical local field effect, therefore the term "quantum plasmon" applies in a restricted sense that the frequency of the bound electrons ω_0 may arise from quantum mechanics.[147-149]

If there are *N* degenerate resonances, they each induce a field that drives the other resonances and the overall effect is stronger. Such situation arises when $N = 2$ in a QD^{2-} (such as $1S_e-1P_e$ transition) or $N = 6$ for QD^{8-} (such as $1P_e-1D_e$ transition) and so on. The bright collective mode

has an oscillator strength Nf. Its frequency is also blue shifted according to Eq. (4), where $\omega_{sp}^2 = \frac{4\pi e^2}{m^*}\frac{N}{V}\frac{1}{\varepsilon_{IB}+2\varepsilon_m}$.

For small carrier density, the correction to the single electron intraband transition is not very large. For example, using the oscillator strength from the $k \cdot p$ model, Eq. (3) gives a less than 10% blue shift for the doubly charged $1S_e-1P_e$ transition. On the contrary, the correction becomes important if there are several strong and neighboring transitions.

Since there is no physical threshold, we propose to define the intraband absorption as "intraband transition" if $\omega_0 > \omega_{sp}$, and "surface plasmon resonance" if $\omega_0 < \omega_{sp}$. The same condition was used by Jain to determine a carrier density that delineates the two regimes.[151]

As discussed at the beginning of this section and shown in Figure 4-10b, the finite energy of the HgS intraband absorption at large sizes invalidates the notion of a single electron transition. However, Figure 4-10d shows that, for the larger sizes, the deviation from the $k \cdot p$ model using $E_P = 4$ eV and $E_G = 0.65$ eV is well captured with Eq. (3) and a fixed surface plasmon frequency ω_{sp}= 0.115 eV. E_P and E_G give an electron effective mass $m^* = 0.14m_0$. Using $\varepsilon_{IB} = 10$ and $\varepsilon_m = 2.2$,[152] this corresponds to an electron density of 1.6×10^{19} cm^{-3} . This number is an order of magnitude lower that reported for ZnO nanocrystals, consistent with the lower plasmon energy observed here.[149, 153] This electron density for the large nanocrystals is, however, in line with the trend in Figure 4-9d. Based on the definition above and the results in Figure 4-10d, the intraband absorption for the HgS particles may then be called a "surface plasmon" for diameters larger than 10 nm, and an "intraband transition" for the smaller particles.

The evolution of the line shape from a broader inhomogeneous line to a narrower Lorentzian at large sizes is not explained by this model. However, it is expected that, since the energy of the resonance is determined by the carrier density and no longer by the size of the particle, the

transition energy is becoming more homogeneous. The limiting linewidth is also an interesting topic.[154] In 2017, Christophe Delerue used a computational method to systematically study the plasmonic linewidth in doped ZnO nanocrystals.[155] He found the width of the LSPR peak was limited by the ionized impurity scattering, which played an important role in the plasmon damping by providing channels for the plasmon decay. As a result, increasing the dopant concentration would broaden the linewidth while varying the particle sizes has little effect. Narrowing plasmonic linewidth is of potential interest for applications in the long-wave infrared, since it matches well the 8−12 microns wavelength range of atmospheric transparency.

Blue shifts due to the local field effects also inform earlier spectroelectrochemistry experiments on CdSe, PbSe and ZnO colloidal quantum dots.[61, 63, 156] All these systems showed a blue shift of the intraband infrared absorption under more reducing conditions. This could not be explained using single electron transitions, since one instead expects the transitions to red shift from $1S_e-1P_e$ to $1P_e-1D_e$ due to the reduced dispersion at higher energy. Here, the increase of local field with the number of available oscillators explains these earlier observations, and reconciles differing interpretations of the intraband absorption as single electron transitions versus plasmon resonances.

4.2 Synthesis of HgS/CdS Core/Shell by Two-Phase Method

4.2.1 Synthesis Procedures

The detailed synthesis procedures are shown below:

a. The cadmium precursor was prepared by dissolving 0.05 mmol of $CdCl_2$ in 10 mL of OAm, 10 mL of TCE and 0.8 g of diphenylamine at 100 °C in glovebox. When all white solids were dissolved, stopped heating and added 0.2 mL of TOP;
b. Synthesized HgS CQDs following the procedures in section 4.1.1;

c. The HgS cores were precipitated and re-dispersed in a predetermined amount of $CdCl_2$ precursor solution, dictated by the desired shell thickness, in which the $(NH_4)_2S$ was injected at once to grow a shell. After 2−3 hours of reaction under vigorous stirring, the dots were separated from the solution by the addition of methanol and centrifugation. The CQDs were then re-dispersed in TCE for further characterization. All syntheses were done under ambient conditions (20 °C and exposed to air).

4.2.2 Properties of HgS/CdS Core/shell

CdS is nearly lattice matched to HgS, allowing in principle the formation of thick shells. The HgS/CdS has a type I alignment which should allow strong confinement of both electrons and holes.[86] The HgS/CdS core/shell synthesis is done under ambient conditions at room temperature. It was found that the cadmium and sulfur precursor grew efficiently to form a shell, leading to a large size increase with no independent nucleation, as observed in Figure 4-11.

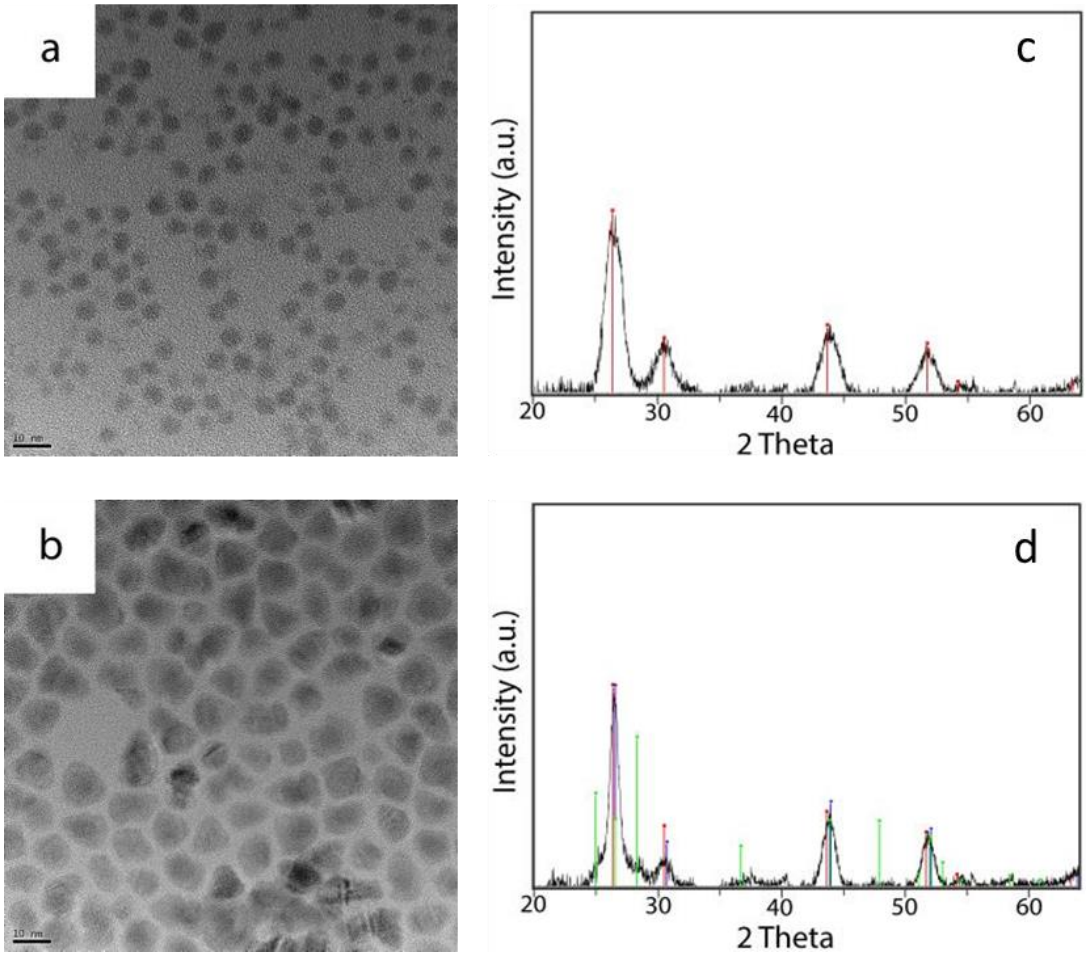

Figure 4-11 *TEM images of (a) HgS cores with average size of 5.5 nm and (b) HgS/CdS with average size of 9.0 nm; XRD spectrum of (c) HgS cores and (d) HgS/CdS core/shell. The red line indicates the bulk β-HgS peak positions, the blue line indicates the bulk β-CdS and the green line α-CdS. The XRD-derived size of HgS/CdS is 9.3 nm, consistent with the TEM value.*

The final core/shell appears rather tetrahedral with a significant fraction of irregular shapes. The XRD spectrum shows the nanocrystals are only in zinc-blende form, meaning the preexisting *β*-HgS core directs the growth of a zinc blende CdS shell. The grain size, derived from the XRD line width using the Scherrer equation, matches the TEM value. The growth of the CdS shell is therefore epitaxial on the HgS core.

The optical spectra, shown in Figure 4-12a and 4-12b, verify that the quantum confinement is retained in the HgS/CdS core/shell structure. The interband absorption spectrum is similar to the intrinsic HgS cores, showing the same three excitonic features.

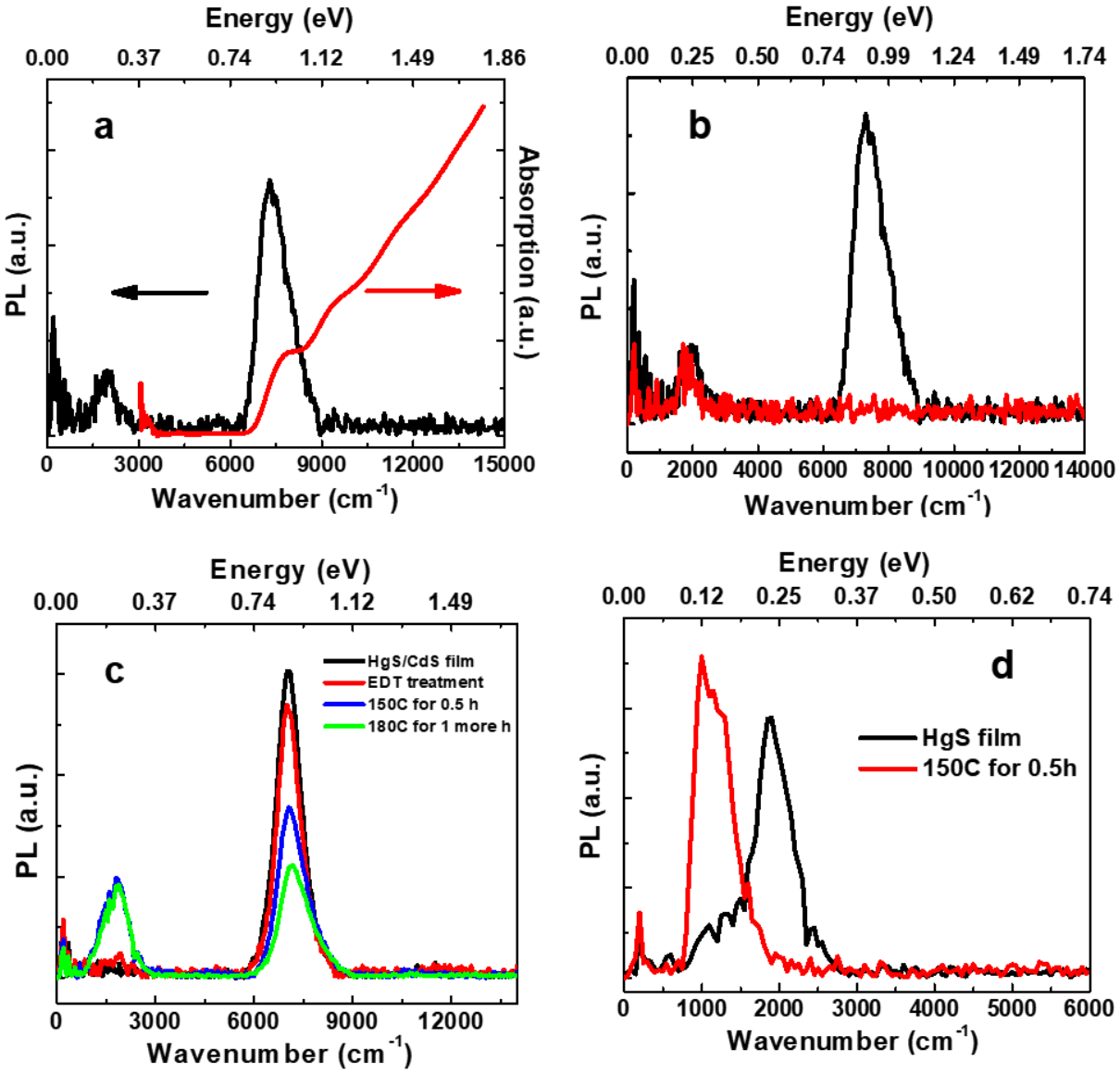

Figure 4-12 *(a) Absorption and PL spectra of the HgS/CdS core/shell; (b) PL spectra of the HgS core after sulfide treatment (red line) and the HgS/CdS core/shell (black line). Measured in TCE solution; (c) HgS/CdS core/shell film annealing test; (d) HgS film annealing test.*

The CdS shell growth causes the HgS/CdS core/shells to exhibit a strong interband PL around 1.5 microns, which is not observed with the HgS cores even after sulfide treatment. The HgS/CdS interband quantum yield was measured as ~5% using an IR-26 reference method.[68, 157] Similar to the previously reported case of HgSe/CdS,[58] the intraband absorption of the HgS cores disappears upon the growth of a CdS shell, meaning that the CdS shell removes the intrinsic n-doping of the HgS cores. There remains, however, a very weak intraband PL at around 2000 cm^{-1} with similar intensity, position, and FWHM compared with the sulfide treated HgS cores.

The initial impetus for encapsulating HgS in CdS was the lack of thermal stability of the cores upon mild annealing. A previous study on HgSe/CdS reported an interesting recovery of doping after ligand exchange with short dithiols and annealing.[58] The HgS/CdS films show similar behavior. The recovery of some intraband PL and a partial loss of the interband PL upon annealing are shown in Figure 4-12c and suggest a recovery of n-doping. As a comparison, Figure 4-12d shows that the bare HgS CQDs lose the intraband PL after 30 min at 150 °C annealing. The upper limit temperature that the HgS/CdS core/shell film could withstand is 200 °C, above which the interfacial alloying would start to happen.

4.3 Conclusions

In chapter 4, I present a simple, highly tunable, two-phase synthesis of HgS CQDs. All syntheses are done under ambient conditions, in air and at room temperature, leading to HgS CQDs with small size dispersion and resolved optical features. The synthesized particles are naturally n-doped, with ~2 electrons per dot in the 3-6 nm diameter range and could be rendered intrinsic with a sulfide treatment. Because HgS is lattice-matched to CdS, the HgS/CdS core/shell is easily grown

to large sizes. This growth leads to the appearance of a strong interband PL in the near-IR. While the natural n-doping is removed with the CdS shell, it reappears upon film fabrication and strengthens further upon annealing. The ease of these syntheses will motivate future studies on these HgS CQD materials for applications such as intraband photodetection, as well as the possible extension of this method to other nanocrystal systems.

For larger sizes HgS nanocrystals, the intraband absorption could not be quenched by sulfide ions and it approached 0.1 eV instead of zero as the size increases. This is assigned to the emergence of a surface plasmon resonance with an electron density of $\sim 1.6 \times 10^{19}$ cm^{-3}. In agreement with a prior work by Jain, a classical model of the local field provides a smooth evolution from single electron transitions to a collective surface plasmon mode. The local field blue shifts the oscillator frequencies to the quadratic mean of the original frequency and the surface plasmon frequency defined for the same density of free electrons. In the absence of a physical threshold separating intraband transitions and surface plasmon, the transitions are labelled as surface plasmon if the bound oscillator frequency is smaller than the surface plasmon frequency.

Chapter 5 Future Directions

I think the purpose of developing new synthetic methods is to provide new possibilities. For example, having a non-aggregated HgTe CQD synthesis makes it possible for the first time to do ligand exchange and grow shell on this material, which allows it to have novel optical and transport properties. In the field of semiconductor nanocrystals, synthesizing a good-quality material that has a small size-dispersion, desired morphology and good optical or transport properties is always the first step for real applications.

In this chapter, I want to discuss several possible directions in mercury chalcogenide CQDs research.

5.1 Learn Synthesis from Organometallic Chemistry

A large proportion of CQD properties comes from its surface. And CQD surfaces, basically are, metal-organic compounds. Borrowing ideas and methods from the field of organometallic chemistry would benefit reaction mechanism study, development of new precursors and surface species recognition.

5.1.1 Reaction Mechanism Study

The study of reaction mechanism uses standard organic chemistry techniques such as NMR to probe the stable intermediates, active precursors, impurities and byproducts. For example, Christopher M. Evans et al. used ^{31}P NMR to study TOPSe precursor and found that pure TOPSe had no reactivity with lead carboxylates.[158] Only after the addition of secondary phosphines did the reaction start to happen. The proposed reaction mechanism is shown in Figure 5-1.

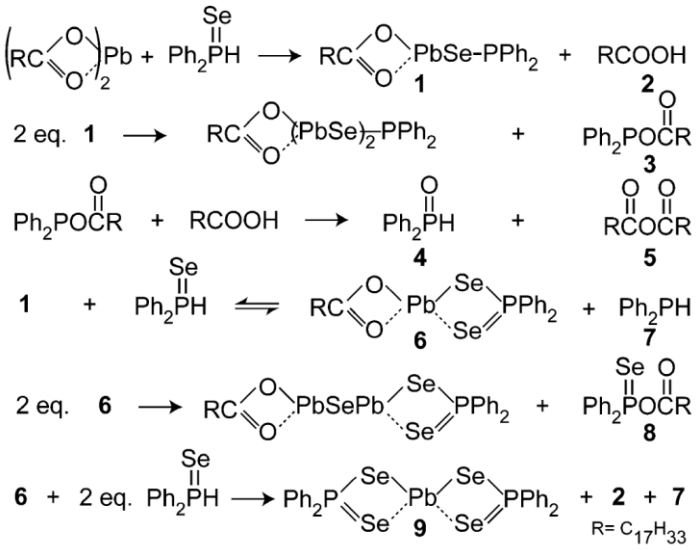

Figure 5-1 *Possible reaction mechanism for the reaction between secondary phosphine and Pb(oleate)$_2$. Adapted from reference 158.*

The higher reactivity from secondary phosphine selenide, diphenylphosphine selenide in this case, may apply to HgSe/CdSe core/shell synthesis via hot-injection to lower the reaction temperature and make the dots more spherical. This reactivity tuning by adding secondary phosphine has been used in PbSe CQD synthesis to obtain monodispersed dots with wide size-tunability.[159]

Another example comes from a recent study from Todd Krauss group.[160] In this work, ^{31}P and ^{77}Se NMR revealed that Cd(octanoate)$_2$ and TBPSe, which are common precursors for CdSe CQD synthesis, decomposed to alkyl cadmium and H_2Se at elevated temperatures above 250 °C, with the mechanism shown in Figure 5-2. The decomposition of Cd(octanoate)$_2$ to alkyl cadmium is still up for debate, as cadmium precursor would easily react with H_2S or H_2Se at much lower temperatures or even room temperature. As a result, the decomposition of Cd(octanoate)$_2$ is only due to the high temperature synthesis and not a necessary condition to obtain CdSe quantum dots.

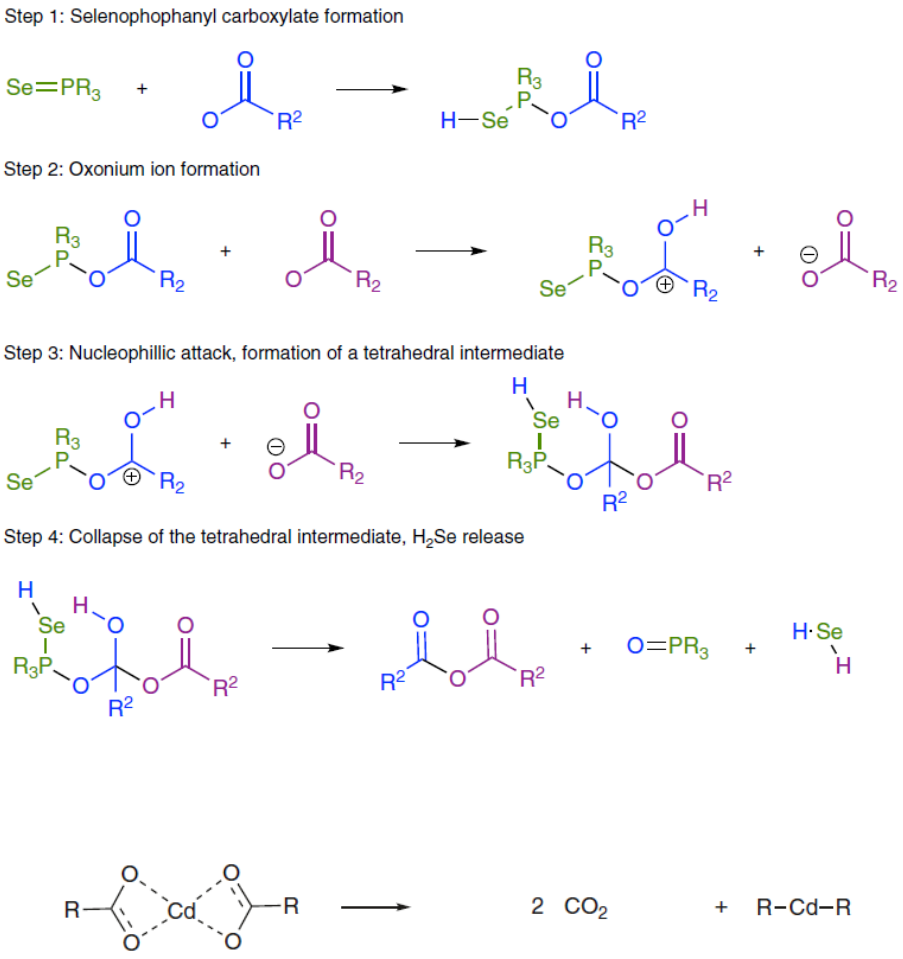

Figure 5-2 *Reaction schemes for (top) H_2Se releasing and (bottom) alkyl cadmium formation. Adapted from reference 160.*

There are no reports for the active precursors in mercury chalcogenide CQD synthesis. However, if it follows the similar mechanism in Figure 5-2, special care needs to be taken to protect against possible alkyl mercury formation. Therefore, we should avoid high temperature growth in mercury chalcogenide CQDs to minimize the possible danger of organic mercury exposure.

5.1.2 New Precursor Development

Precursors are extremely important in CQD synthesis. A precursor that has reasonable reactivity in the nucleation step while maintains a relative high oversaturation during the growth is crucial to avoid Ostwald ripening and get monodispersed dots.[161] One problem in mercury chalcogenide CQD synthesis is that most precursors such as $(TMS)_2Te$, $(TMS)_2Se$ and selenourea can react at low temperatures even room temperature, indicating they are still too reactive for the synthesis. This will cause the precursor to be consumed very fast at elevated temperatures and quickly enter Ostwald ripening regime. A low-temperature, kinetically controlled synthesis is also prone to have more defects compared with high-temperature growth. In section 3.1, we discussed the synthesis of monodispersed HgSe CQDs. The slow conversion rate of 3-substituted selenourea is the key to avoid ripening and obtain monodispersed dots. However, 3-substituted selenourea can still react with mercury precursors at room-temperature. As a result, developing even less reactive chalcogen precursors such as 4-substituted selenourea might be a good option.

Another possible way to suppress ripening is to slowly inject extra precursors into the reaction mixture. One example is the synthesis of monodispersed InAs CQDs by continuous injection as shown in Figure 5-3.[162]

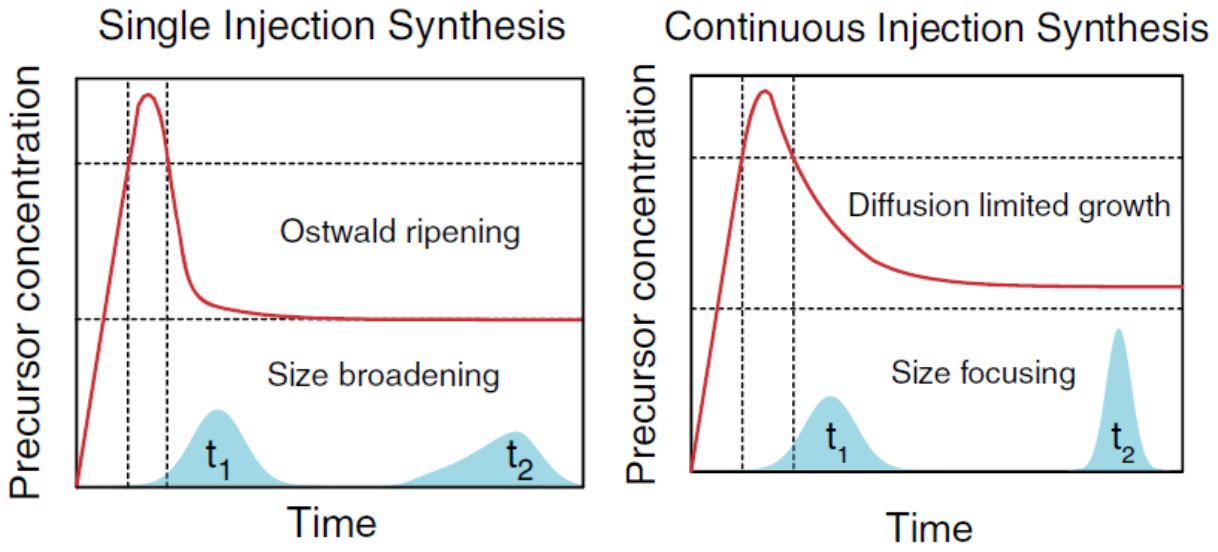

Figure 5-3 *Comparison between (left) typical hot-injection and (right) continuous precursor injection. Adapted from reference 162.*

In this synthesis, only 10% of total arsenide precursors were used for nucleation and the rest 90% were slowly injected. And InAs can be obtained with < 8% size dispersion. Similar approach has been adopted by Sohee Jeong and co-workers by continuous injection of InAs nanoclusters.[163] Note that continuous injection is different from multiple precursor injections, the former usually requires a syringe pump to better control the injection rate.

5.1.3 Surface Chemistry

In section 2.3.2, we mentioned that there are a number of reports which showed excess metal atoms on the quantum dot surfaces.[89-95] The ratios between cation and anion were determined by various techniques such as NMR, XPS, inductively coupled plasma – mass spectrometry (ICP-MS), inductively coupled plasma – optical emission spectrometry (ICP-OES) and Rutherford backscattering spectrometry (RBS). Other important surface information could be retrieved with

these techniques. For example, XPS is good at determining the oxidation states of surface atoms, which have different binding energies. Figure 5-4 shows the XPS results of OAcid-capped PbS CQDs before and after air exposure.[95] It is clear that surface S^{2-} gets oxidized to S^{4+} and S^{6+} in air.

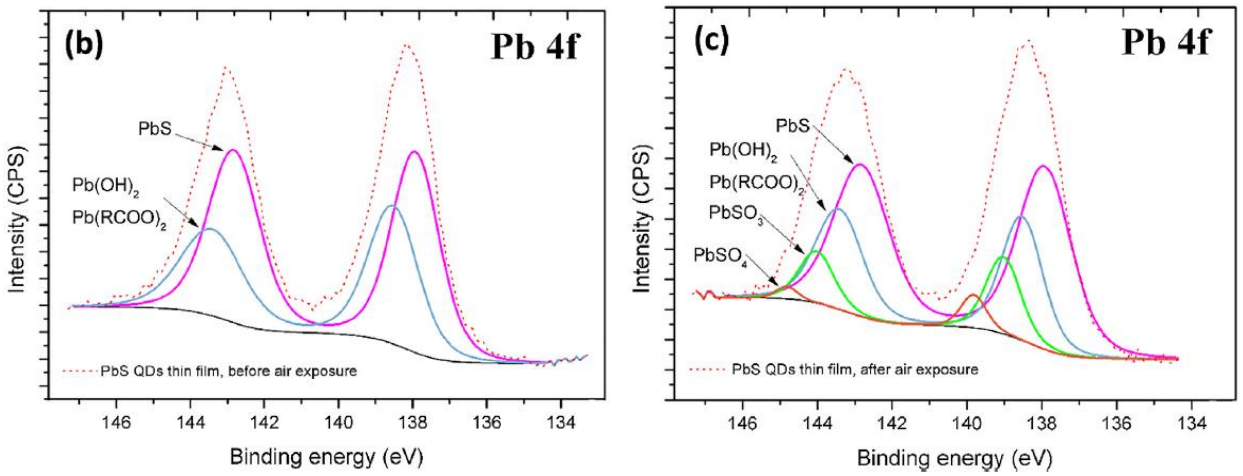

Figure 5-4 *XPS spectra of PbS CQD films (a) before and (after) air exposure. Adapted from reference 95.*

In mercury chalcogenide synthesis, because mercury precursor tends to get reduced at elevated temperatures, it is a question whether Hg^0 or Hg^+ species exist or not. Moreover, S, Se and Te all tend to oxidize in air, in what form do these elements exist is of great importance. Prashant Kamat and co-workers previously reported a light-induced surface oxidation of CdSe to CdO and SeO_2.[164] Similar reaction may happen in mercury chalcogenide CQDs to form HgO and TeO_2 (or SeO_2). Both HgO and TeO_2 (or SeO_2) are wide-gap materials that can form type-I core/shell with HgTe (or HgSe). This heterostructure may help reducing the effect of surface traps but are not good for charge transport. This might be the reason why EDT/HCl treatment, which can dissolve HgO and TeO_2 (or SeO_2), is good for electrochemistry measurement but sometimes makes the PL worse

than bare mercury chalcogenide CQDs (not core/shells).[64] XPS could be a possible method to answer these questions.

NMR is another important technique that could differentiate bound and free ligands in the solution.[165] As a result, it is the best way to determine the exact surface ligands. NMR can also work quantitatively to give the number of ligands based on the integrated resonance intensity. Figure 5-5 shows the NMR of free and bound OAcid in toluene-d8. The peaks of bound ligands usually become broader and shift downfield.

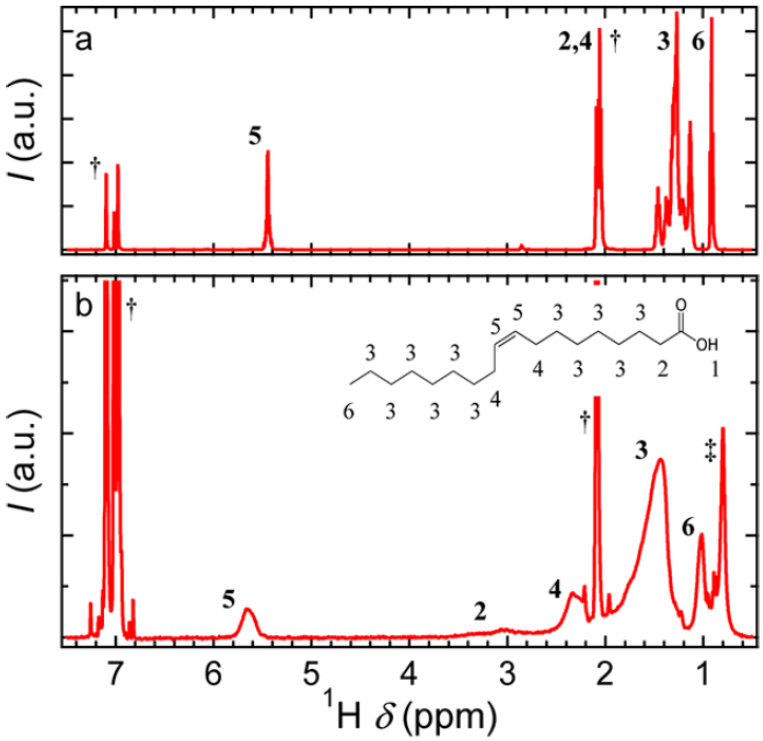

Figure 5-5 *NMR spectra of (top) free and (bottom) CdSe-bound OAcid in toluene-d8. Adapted from reference 165.*

There is no NMR study on mercury chalcogenide CQDs yet. However, it may help a lot to decide the exact surface ligand or ligand ratio, especially if mixed ligands such as amine, TOP and thiol are used at the same time. Besides, to correlate the surface ligand with PL intensity can provide us with more information about the energy coupling to ligand vibrational modes and possible surface traps.[79]

5.2 Inorganic Ligand Exchange and Matrix

Inorganic ligand exchange and matrix embedment are standard methods to remove surface organic ligands from CQDs. The benefits for doing these surface treatments include stabilizing nanocrystals, improving carrier mobility, controlling the doping level and increasing quantum yield.

If the thermal stability of nanocrystals is so low that they tend to sinter on films, a matrix embedment might be a good solution. The common materials used for inorganic matrix include SiO_2, TiO_2, and As_2S_3.[56] In principle, these inorganic materials are better than organic ligand in terms of light and thermal stability, which makes it possible to fabricate all-inorganic devices.[166-167]

As mentioned previously, mercury chalcogenide CQDs have poor thermal stability. Therefore, it should be a good idea to grow matrix on them. However, up till now, only one paper on $HgTe/As_2S_3$ has been published, with no indication of improved stability.[8] Here in Figure 5-6, I show the preliminary results on $HgTe/SiO_2$ and $HgTe/TiO_2$.

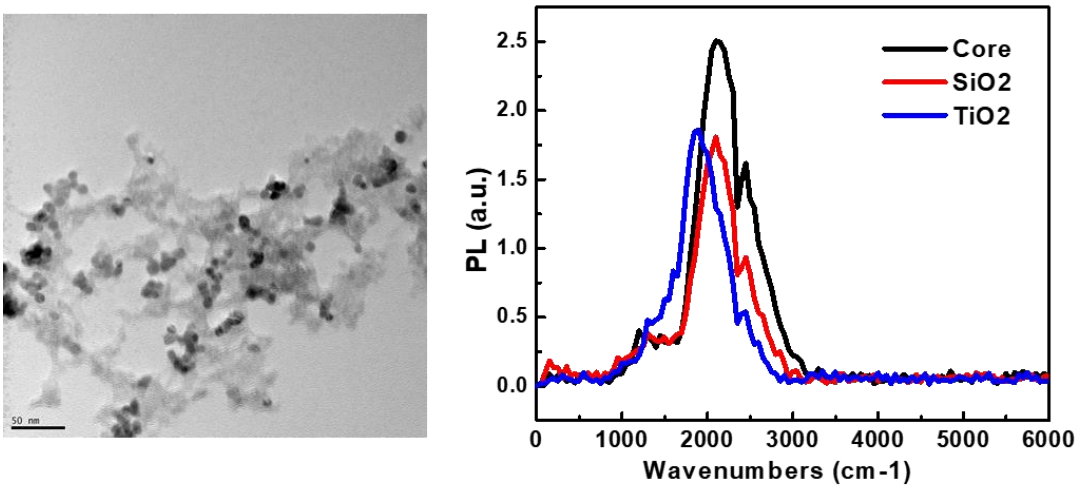

Figure 5-6 *(left) TEM image of HgTe/TiO_2; (right) Film PL spectra of HgTe/SiO_2 and HgTe/TiO_2 compared with initial HgTe CQDs.*

The growth of SiO_2 and TiO_2 are based on published results using tetraethyl orthosilicate and titanium butoxide as the Si and Ti precursor, respectively.[168-169] Small amount of water was added to the toluene solution of non-aggregated OAm-capped HgTe CQDs together with the Si or Ti precursor to induce a hydrolysis reaction. The obtained solids were then annealed at 200 °C to remove water. As shown in Figure 5-6, HgTe dots are embedded in TiO_2 matrix with small regions of aggregated particles and TiO_2 is likely to be in the form of an amorphous matrix. The PL is preserved even after annealing at 200 °C for 4 h. In section 2.4, I mentioned that the HgTe/CdTe core/shell cannot withstand temperatures above 200 °C due to the interfacial alloying. Here, because TiO_2 is likely amorphous and not lattice mismatched with HgTe, the diffusion of interfacial atoms and therefore alloying is greatly suppressed. This strategy may make it possible to sinter mercury chalcogenide CQD films at temperatures as high as 300 °C to "burn" all surface organic molecules.

In terms of PL QY, most ligand exchange or inorganic matrix methods would maintain or have a negative effect on the PL intensity despite the removal of organic molecules, which has been observed in many CQD systems such as As_2S_3-treated HgTe and halide-exchanged PbSe.[8, 170] One possible reason is that these treatments will introduce surface traps to the quantum dots as the better-passivated organic ligands are replaced by short, ionic ligands. If the ligand exchange is carried out in air, an exposure to O_2 may cause severe oxidation of the surface anions as well. Besides, ligand exchange may induce aggregation as the quantum dot distance shortens. To partially recover from these negative effects, a proper choice of the exchange ions may be important. In the study of PbSe,[170] it was found that the softer I^- gave the best PL compared with harder ions such as Br^- and Cl^- given the fact that it has the strongest interaction with Pb^{2+}. As a result, I^- can better passivate the PbSe surfaces and avoid sintering. Since Hg^{2+} is even softer than Pb^{2+}, ions like I^- and S^{2-} may be the ones to choose. Also, performing ligand exchange on type-I core/shells may greatly decrease the chance of creating surface traps.

The biggest advantage of ligand exchange and inorganic matrix is the improvement of carrier mobility. In aggregated-HgTe/As_2S_3 system, the electron mobility, ~10^{-2} $cm^2/(V \cdot s)$, was two-order magnitude higher than that of the EDT-treated dots.[8] The mobility increase would directly improve the performance of infrared photodetectors. In PC devices, the detectivity in theory is proportional to the square root of mobility. In PV devices, mobility has a positive effect on the diffusion coefficient. However, higher mobility also means lower resistance and higher Johnson noise in PV devices.

5.3 Wide-Gap Intraband Materials

There are four narrow gap CQD materials that have been reported to have air-stable intraband transitions: HgS, HgSe, HgTe and Ag_2Se. Meanwhile, chemically or electrochemically doped CdSe CQDs also have mid-IR intraband absorptions. This brings up a question: is it possible to have air-stable intraband transition in wide-gap materials?

One basic requirement is that the environmental Fermi level needs to be higher than or at least close to the conduction band energy of bulk semiconductors.

From Figure 5-7, most common metal chalcogenide CQDs, such as CdS, CdSe and PbSe, have zero hope to become air-stable intraband materials. However, several candidates, such as FeS_2 and WS_2, meet this band energy criteria. Besides, compared with metal chalcogenides, the conduction band energies of their oxide counterparts become closer to the environmental Fermi level. One possible candidate is CdO, which has shown surface plasmon resonance in its nanoparticle form.[171] In section 4.1, we discussed the transition between intraband transition and surface plasmon as the particle size changes. As a result, growing smaller CdO nanoparticles may be able to show intraband transitions.

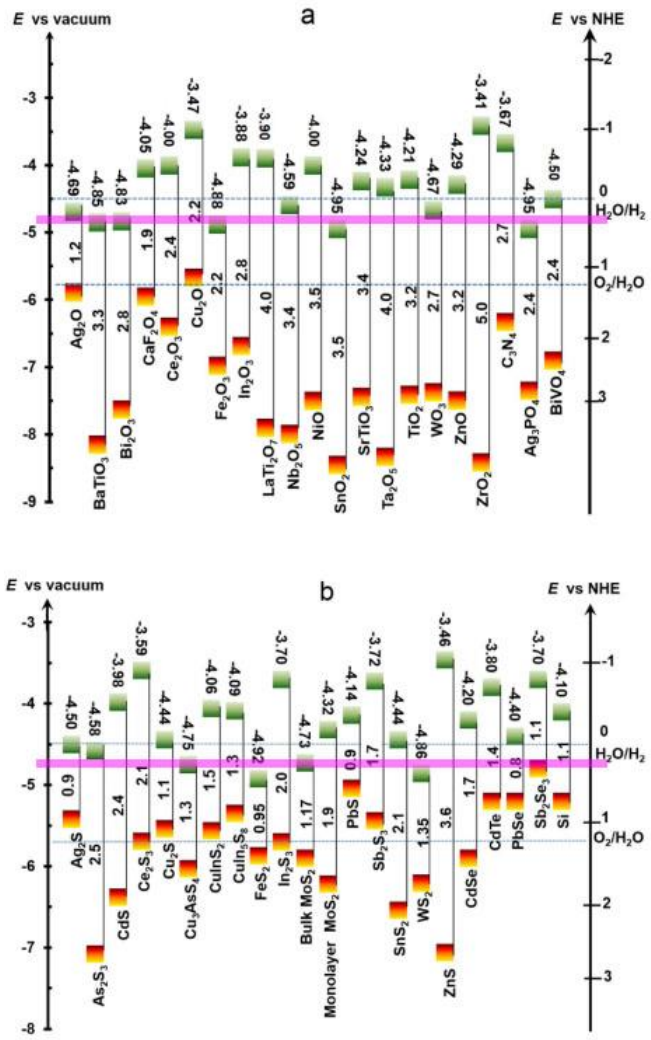

Figure 5-7 *Band gap positions of common semiconductors. The green square is conduction band and the red square is valence band. Magenta strips were added to represent the range of ambient Fermi level. The energy gap is adapted from reference 108 and the positions of ambient Fermi level are adapted from reference 64.*

References

1. Richards, P. L. Bolometers for Infrared and Millimeter Waves. *J. Appl. Phys.* **1994,** *76* (1), 1-24.

2. Rogalski, A. HgCdTe Infrared Detector Material: History, Status and Outlook. *Rep. Prog. Phys.* **2005,** *68* (10), 2267.

3. Lhuillier, E.; Guyot-Sionnest, P. Recent Progresses in Mid Infrared Nanocrystal Optoelectronics. *IEEE J. Sel. Top. Quantum Electron.* **2017,** *23* (5), 1-8.

4. Ackerman, M. M.; Tang, X.; Guyot-Sionnest, P. Fast and Sensitive Colloidal Quantum Dot Mid-Wave Infrared Photodetectors. *ACS Nano* **2018,** *12* (7), 7264-7271.

5. Melnychuk, C.; Guyot-Sionnest, P. Slow Auger Relaxation in HgTe Colloidal Quantum Dots. *J. Phys. Chem. Lett.* **2018,** *9* (9), 2208-2211.

6. Keuleyan, S.; Lhuillier, E.; Brajuskovic, V.; Guyot-Sionnest, P. Mid-Infrared HgTe Colloidal Quantum Dot Photodetectors. *Nat. Photonics* **2011,** *5* (8), 489-493.

7. Lhuillier, E.; Keuleyan, S.; Rekemeyer, P.; Guyot-Sionnest, P. Thermal Properties of Mid-Infrared Colloidal Quantum Dot Detectors. *J. Appl. Phys.* **2011,** *110* (3), 033110.

8. Lhuillier, E.; Keuleyan, S.; Zolotavin, P.; Guyot-Sionnest, P. Mid-Infrared HgTe/As_2S_3 Field Effect Transistors and Photodetectors. *Adv. Mater.* **2013,** *25* (1), 137-141.

9. Guyot-Sionnest, P.; Roberts, J. A. Background Limited Mid-Infrared Photodetection with Photovoltaic HgTe Colloidal Quantum Dots. *Appl. Phys. Lett.* **2015,** *107* (25), 253104.

10. Tang, X.; Ackerman, M. M.; Guyot-Sionnest, P. Thermal Imaging with Plasmon Resonance Enhanced HgTe Colloidal Quantum Dot Photovoltaic Devices. *ACS Nano* **2018,** *12* (7), 7362-7370.

11. Jeong, K. S.; Deng, Z.; Keuleyan, S.; Liu, H.; Guyot-Sionnest, P. Air-Stable n-Doped Colloidal HgS Quantum Dots. *J. Phys. Chem. Lett.* **2014,** *5* (7), 1139-1143.

12. Delin, A. First-Principles Calculations of the II-VI Semiconductor β-HgS: Metal or Semiconductor. *Phys. Rev. B: Condens. Matter Mater. Phy.* **2002,** *65* (15), 153205.

13. Delin, A.; Klüner, T. Excitation Spectra and Ground-State Properties from Density-Functional Theory for the Inverted Band-Structure Systems β-HgS, HgSe, and HgTe. *Phys. Rev. B: Condens. Matter Mater. Phy.* **2002,** *66* (3), 035117.

14. Svane, A.; Christensen, N. E.; Cardona, M.; Chantis, A. N.; van Schilfgaarde, M.; Kotani, T. Quasiparticle Band Structures of β-HgS, HgSe, and HgTe. *Phys. Rev. B: Condens. Matter Mater. Phy.* **2011,** *84* (20), 205205.

15. Deng, Z.; Jeong, K. S.; Guyot-Sionnest, P. Colloidal Quantum Dots Intraband Photodetectors. *ACS Nano* **2014,** *8* (11), 11707-11714.

16. Lhuillier, E.; Scarafagio, M.; Hease, P.; Nadal, B.; Aubin, H.; Xu, X. Z.; Lequeux, N.; Patriarche, G.; Ithurria, S.; Dubertret, B. Infrared Photodetection Based on Colloidal Quantum-Dot Films with High Mobility and Optical Absorption up to THz. *Nano Lett.* **2016,** *16* (2), 1282-1286.

17. Tang, X.; Wu, G. f.; Lai, K. W. C. Plasmon Resonance Enhanced Colloidal HgSe Quantum Dot Filterless Narrowband Photodetectors for Mid-Wave Infrared. *J. Mater. Chem. C* **2017,** *5* (2), 362-369.

18. Junod, P.; Hediger, H.; Kilchör, B.; Wullschleger, J. Metal-Non-Metal Transition in Silver Chalcogenides. *Philos. Mag.* **1977,** *36* (4), 941-958.

19. Sahu, A.; Qi, L.; Kang, M. S.; Deng, D.; Norris, D. J. Facile Synthesis of Silver Chalcogenide (Ag_2E; E = Se, S, Te) Semiconductor Nanocrystals. *J. Am. Chem. Soc.* **2011,** *133* (17), 6509-6512.

20. Sahu, A.; Khare, A.; Deng, D. D.; Norris, D. J. Quantum Confinement in Silver Selenide Semiconductor Nanocrystals. *Chem. Commun.* **2012,** *48* (44), 5458-5460.

21. Park, M.; Choi, D.; Choi, Y.; Shin, H.-b.; Jeong, K. S. Mid-Infrared Intraband Transition of Metal Excess Colloidal Ag_2Se Nanocrystals. *ACS Photonics* **2018,** *5* (5), 1907-1911.

22. Qu, J.; Goubet, N.; Livache, C.; Martinez, B.; Amelot, D.; Gréboval, C.; Chu, A.; Ramade, J.; Cruguel, H.; Ithurria, S.; Silly, M. G.; Lhuillier, E. Intraband Mid-Infrared Transitions in Ag_2Se Nanocrystals: Potential and Limitations for Hg-Free Low-Cost Photodetection. *J. Phys. Chem. C* **2018,** *122* (31), 18161-18167.

23. Rabii, S. Energy-Band Structure and Electronic Properties of SnTe. *Phys. Rev.* **1969,** *182* (3), 821-828.

24. Littlewood, P. B.; Mihaila, B.; Schulze, R. K.; Safarik, D. J.; Gubernatis, J. E.; Bostwick, A.; Rotenberg, E.; Opeil, C. P.; Durakiewicz, T.; Smith, J. L.; Lashley, J. C. Band Structure of SnTe Studied by Photoemission Spectroscopy. *Phys. Rev. Lett.* **2010,** *105* (8), 086404.

25. Kovalenko, M. V.; Heiss, W.; Shevchenko, E. V.; Lee, J.-S.; Schwinghammer, H.; Alivisatos, A. P.; Talapin, D. V. SnTe Nanocrystals: A New Example of Narrow-Gap Semiconductor Quantum Dots. *J. Am. Chem. Soc.* **2007,** *129* (37), 11354-11355.

26. Xu, Y.; Al-Salim, N.; Hodgkiss, J. M.; Tilley, R. D. Solution Synthesis and Optical Properties of SnTe Nanocrystals. *Cryst. Growth Des.* **2011,** *11* (7), 2721-2723.

27. Guo, S.; Fidler, A. F.; He, K.; Su, D.; Chen, G.; Lin, Q.; Pietryga, J. M.; Klimov, V. I. Shape-Controlled Narrow-Gap SnTe Nanostructures: From Nanocubes to Nanorods and Nanowires. *J. Am. Chem. Soc.* **2015,** *137* (48), 15074-15077.

28. Arachchige, I. U.; Kanatzidis, M. G. Anomalous Band Gap Evolution from Band Inversion in $Pb_{1-x}Sn_xTe$ Nanocrystals. *Nano Lett.* **2009,** *9* (4), 1583-1587.

29. Murray, C. B.; Norris, D. J.; Bawendi, M. G. Synthesis and Characterization of Nearly Monodisperse CdE (E = Sulfur, Selenium, Tellurium) Semiconductor Nanocrystallites. *J. Am. Chem. Soc.* **1993,** *115* (19), 8706-8715.

30. Green, M.; Mirzai, H. Synthetic Routes to Mercury Chalcogenide Quantum Dots. *J. Mater. Chem. C* **2018,** *6* (19), 5097-5112.

31. Rogach, A.; Kershaw, S. V.; Burt, M.; Harrison, M. T.; Kornowski, A.; Eychmüller, A.; Weller, H. Colloidally Prepared HgTe Nanocrystals with Strong Room-Temperature Infrared Luminescence. *Adv. Mater.* **1999,** *11* (7), 552-555.

32. Kovalenko, M. V.; Kaufmann, E.; Pachinger, D.; Roither, J.; Huber, M.; Stangl, J.; Hesser, G.; Schäffler, F.; Heiss, W. Colloidal HgTe Nanocrystals with Widely Tunable Narrow Band Gap Energies: From Telecommunications to Molecular Vibrations. *J. Am. Chem. Soc.* **2006,** *128* (11), 3516-3517.

33. Abdelazim, N. M.; Zhu, Q.; Xiong, Y.; Zhu, Y.; Chen, M.; Zhao, N.; Kershaw, S. V.; Rogach, A. L. Room Temperature Synthesis of HgTe Quantum Dots in an Aprotic Solvent Realizing High Photoluminescence Quantum Yields in the Infrared. *Chem. Mater.* **2017,** *29* (18), 7859-7867.

34. Green, M.; Wakefield, G.; Dobson, P. J. A Simple Metalorganic Route to Organically Passivated Mercury Telluride Nanocrystals. *J. Mater. Chem.* **2003,** *13* (5), 1076-1078.

35. Kim, S.; Kim, T.; Im, S. H.; Seok, S. I.; Kim, K. W.; Kim, S.; Kim, S.-W. Bandgap Engineered Monodisperse and Stable Mercury Telluride Quantum Dots and Their Application for Near-Infrared Photodetection. *J. Mater. Chem.* **2011,** *21* (39), 15232-15236.

36. Keuleyan, S.; Lhuillier, E.; Guyot-Sionnest, P. Synthesis of Colloidal HgTe Quantum Dots for Narrow Mid-IR Emission and Detection. *J. Am. Chem. Soc.* **2011,** *133* (41), 16422-16424.

37. Tang, X.; Tang, X.; Lai, K. W. C. Scalable Fabrication of Infrared Detectors with Multispectral Photoresponse Based on Patterned Colloidal Quantum Dot Films. *ACS Photonics* **2016,** *3* (12), 2396-2404.

38. Chen, M.; Shao, L.; Kershaw, S. V.; Yu, H.; Wang, J.; Rogach, A. L.; Zhao, N. Photocurrent Enhancement of HgTe Quantum Dot Photodiodes by Plasmonic Gold Nanorod Structures. *ACS Nano* **2014,** *8* (8), 8208-8216.

39. Chen, M.; Yu, H.; Kershaw, S. V.; Xu, H.; Gupta, S.; Hetsch, F.; Rogach, A. L.; Zhao, N. Fast, Air-Stable Infrared Photodetectors based on Spray-Deposited Aqueous HgTe Quantum Dots. *Adv. Funct. Mater.* **2014,** *24* (1), 53-59.

40. Huo, N.; Gupta, S.; Konstantatos, G. MoS_2–HgTe Quantum Dot Hybrid Photodetectors beyond 2 μm. *Adv. Mater.* **2017,** *29* (17), 1606576.

41. Palosz, W.; Trivedi, S.; Zhang, D.; Meissner, G.; Olver, K.; DeCuir, E.; Wijewarnasuriya, P. S.; Jensen, J. L. HgTe Quantum Dots for Near-, Mid-, and Long-Wavelength IR Devices. *J. Electron. Mater.* **2017,** *46* (9), 5411-5417.

42. Keuleyan, S. E.; Guyot-Sionnest, P.; Delerue, C.; Allan, G. Mercury Telluride Colloidal Quantum Dots: Electronic Structure, Size-Dependent Spectra, and Photocurrent Detection up to 12 μm. *ACS Nano* **2014,** *8* (8), 8676-8682.

43. Goubet, N.; Jagtap, A.; Livache, C.; Martinez, B.; Portalès, H.; Xu, X. Z.; Lobo, R. P. S. M.; Dubertret, B.; Lhuillier, E. Terahertz HgTe Nanocrystals: Beyond Confinement. *J. Am. Chem. Soc.* **2018,** *140* (15), 5033-5036.

44. Izquierdo, E.; Robin, A.; Keuleyan, S.; Lequeux, N.; Lhuillier, E.; Ithurria, S. Strongly Confined HgTe 2D Nanoplatelets as Narrow Near-Infrared Emitters. *J. Am. Chem. Soc.* **2016,** *138* (33), 10496-10501.

45. Martinez, B.; Livache, C.; Goubet, N.; Izquierdo, E.; Silly, M. G.; Ithurria, S.; Lhuillier, E. Optoelectronics Using 2D Colloidal Nanocrystals from Wide Band Gap to Narrow Band Gap Materials. *Phys. Status Solidi C* **2017,** *14* (10), 1700138.

46. Livache, C.; Izquierdo, E.; Martinez, B.; Dufour, M.; Pierucci, D.; Keuleyan, S.; Cruguel, H.; Becerra, L.; Fave, J. L.; Aubin, H.; Ouerghi, A.; Lacaze, E.; Silly, M. G.; Dubertret, B.; Ithurria, S.; Lhuillier, E. Charge Dynamics and Optolectronic Properties in HgTe Colloidal Quantum Wells. *Nano Lett.* **2017,** *17* (7), 4067–4074.

47. Izquierdo, E.; Dufour, M.; Chu, A.; Livache, C.; Martinez, B.; Amelot, D.; Patriarche, G.; Lequeux, N.; Lhuillier, E.; Ithurria, S. Coupled HgSe Colloidal Quantum Wells through a Tunable Barrier: A Strategy To Uncouple Optical and Transport Band Gap. *Chem. Mater.* **2018,** *30* (12), 4065-4072.

48. Higginson, K. A.; Kuno, M.; Bonevich, J.; Qadri, S. B.; Yousuf, M.; Mattoussi, H. Synthesis and Characterization of Colloidal β-HgS Quantum Dots. *J. Phys. Chem. B* **2002,** *106* (39), 9982-9985.

49. Kuno, M.; Higginson, K. A.; Qadri, S. B.; Yousuf, M.; Lee, S. H.; Davis, B. L.; Mattoussi, H. Molecular Clusters of Binary and Ternary Mercury Chalcogenides: Colloidal Synthesis, Characterization, and Optical Spectra. *J. Phys. Chem. B* **2003,** *107* (24), 5758-5767.

50. Howes, P.; Green, M.; Johnston, C.; Crossley, A. Synthesis and Shape Control of Mercury Selenide (HgSe) Quantum Dots. *J. Mater. Chem.* **2008,** *18* (29), 3474-3480.

51. Liu, L.; Zhuang, Z.; Xie, T.; Wang, Y.-G.; Li, J.; Peng, Q.; Li, Y. Shape Control of CdSe Nanocrystals with Zinc Blende Structure. *J. Am. Chem. Soc.* **2009,** *131* (45), 16423-16429.

52. Hendricks, M. P.; Campos, M. P.; Cleveland, G. T.; Jen-La Plante, I.; Owen, J. S. A Tunable Library of Substituted Thiourea Precursors to Metal Sulfide Nanocrystals. *Science* **2015,** *348* (6240), 1226-1230.

53. Campos, M. P.; Hendricks, M. P.; Beecher, A. N.; Walravens, W.; Swain, R. A.; Cleveland, G. T.; Hens, Z.; Sfeir, M. Y.; Owen, J. S. A Library of Selenourea Precursors to PbSe Nanocrystals with Size Distributions near the Homogeneous Limit. *J. Am. Chem. Soc.* **2017,** *139* (6), 2296-2305.

54. Hamachi, L. S.; Jen-La Plante, I.; Coryell, A. C.; De Roo, J.; Owen, J. S. Kinetic Control over CdS Nanocrystal Nucleation Using a Library of Thiocarbonates, Thiocarbamates, and Thioureas. *Chem. Mater.* **2017,** *29* (20), 8711-8719.

55. Hines, M. A.; Guyot-Sionnest, P. Synthesis and Characterization of Strongly Luminescing ZnS-Capped CdSe Nanocrystals. *J. Phys. Chem.* **1996,** *100* (2), 468-471.

56. Ghosh Chaudhuri, R.; Paria, S. Core/Shell Nanoparticles: Classes, Properties, Synthesis Mechanisms, Characterization, and Applications. *Chem. Rev.* **2012,** *112* (4), 2373-2433.

57. Harrison, M. T.; Kershaw, S. V.; Rogach, A. L.; Kornowski, A.; Eychmüller, A.; Weller, H. Wet Chemical Synthesis of Highly Luminescent HgTe/CdS Core/Shell Nanocrystals. *Adv. Mater.* **2000,** *12* (2), 123-125.

58. Deng, Z.; Guyot-Sionnest, P. Intraband Luminescence from HgSe/CdS Core/Shell Quantum Dots. *ACS Nano* **2016,** *10* (2), 2121-2127.

59. Sagar, L. K.; Walravens, W.; Maes, J.; Geiregat, P.; Hens, Z. HgSe/CdE (E = S, Se) Core/Shell Nanocrystals by Colloidal Atomic Layer Deposition. *J. Phys. Chem. C* **2017,** *121* (25), 13816-13822.

60. Shim, M.; Guyot-Sionnest, P. n-Type Colloidal Semiconductor Nanocrystals. *Nature* **2000,** *407* (6807), 981-983.

61. Shim, M.; Guyot-Sionnest, P. Organic-Capped ZnO Nanocrystals: Synthesis and n-Type Character. *J. Am. Chem. Soc.* **2001,** *123* (47), 11651-11654.

62. Yu, D.; Wang, C.; Guyot-Sionnest, P. n-Type Conducting CdSe Nanocrystal Solids. *Science* **2003,** *300* (5623), 1277-1280.

63. Guyot-Sionnest, P.; Wang, C. Fast Voltammetric and Electrochromic Response of Semiconductor Nanocrystal Thin Films. *J. Phys. Chem. B* **2003,** *107* (30), 7355-7359.

64. Chen, M.; Guyot-Sionnest, P. Reversible Electrochemistry of Mercury Chalcogenide Colloidal Quantum Dot Films. *ACS Nano* **2017,** *11* (4), 4165-4173.

65. Shen, G.; Chen, M.; Guyot-Sionnest, P. Synthesis of Nonaggregating HgTe Colloidal Quantum Dots and the Emergence of Air-Stable n-Doping. *J. Phys. Chem. Lett.* **2017,** *8* (10), 2224-2228.

66. Lin, W.; Niu, Y.; Meng, R.; Huang, L.; Cao, H.; Zhang, Z.; Qin, H.; Peng, X. Shell-Thickness Dependent Optical Properties of CdSe/CdS Core/Shell Nanocrystals Coated with Thiol Ligands. *Nano Res.* **2016,** *9* (1), 260-271.

67. Keuleyan, S.; Kohler, J.; Guyot-Sionnest, P. Photoluminescence of Mid-Infrared HgTe Colloidal Quantum Dots. *J. Phys. Chem. C* **2014,** *118* (5), 2749-2753.

68. Semonin, O. E.; Johnson, J. C.; Luther, J. M.; Midgett, A. G.; Nozik, A. J.; Beard, M. C. Absolute Photoluminescence Quantum Yields of IR-26 Dye, PbS, and PbSe Quantum Dots. *J. Phys. Chem. Lett.* **2010,** *1* (16), 2445-2450.

69. Liu, H.; Guyot-Sionnest, P. Photoluminescence Lifetime of Lead Selenide Colloidal Quantum Dots. *J. Phys. Chem. C* **2010,** *114* (35), 14860-14863.

70. Pietryga, J. M.; Schaller, R. D.; Werder, D.; Stewart, M. H.; Klimov, V. I.; Hollingsworth, J. A. Pushing the Band Gap Envelope: Mid-Infrared Emitting Colloidal PbSe Quantum Dots. *J. Am. Chem. Soc.* **2004,** *126* (38), 11752-11753.

71. Moreels, I.; Justo, Y.; De Geyter, B.; Haustraete, K.; Martins, J. C.; Hens, Z. Size-Tunable, Bright, and Stable PbS Quantum Dots: A Surface Chemistry Study. *ACS Nano* **2011,** *5* (3), 2004-2012.

72. Houtepen, A. J.; Hens, Z.; Owen, J. S.; Infante, I. On the Origin of Surface Traps in Colloidal II–VI Semiconductor Nanocrystals. *Chem. Mater.* **2017,** *29* (2), 752-761.

73. Geiregat, P.; Houtepen, A. J.; Sagar, L. K.; Infante, I.; Zapata, F.; Grigel, V.; Allan, G.; Delerue, C.; Van Thourhout, D.; Hens, Z. Continuous-Wave Infrared Optical Gain and Amplified Spontaneous Emission at Ultralow Threshold by Colloidal HgTe Quantum Dots. *Nat. Mater.* **2017,** *17*, 35.

74. Grigel, V.; Sagar, L. K.; De Nolf, K.; Zhao, Q.; Vantomme, A.; De Roo, J.; Infante, I.; Hens, Z. The Surface Chemistry of Colloidal HgSe Nanocrystals, toward Stoichiometric Quantum Dots by Design. *Chem. Mater.* **2018**.

75. Kirkwood, N.; Monchen, J. O. V.; Crisp, R. W.; Grimaldi, G.; Bergstein, H. A. C.; du Fossé, I.; van der Stam, W.; Infante, I.; Houtepen, A. J. Finding and Fixing Traps in II–VI and III–V

Colloidal Quantum Dots: The Importance of Z-Type Ligand Passivation. *J. Am. Chem. Soc.* **2018,** *140* (46), 15712–15723.

76. van der Stam, W.; du Fossé, I.; Grimaldi, G.; Monchen, J. O. V.; Kirkwood, N.; Houtepen, A. J. Spectroelectrochemical Signatures of Surface Trap Passivation on CdTe Nanocrystals. *Chem. Mater.* **2018,** *30* (21), 8052–8061.

77. Shen, G.; Guyot-Sionnest, P. HgTe/CdTe and HgSe/CdX (X = S, Se, and Te) Core/Shell Mid-Infrared Quantum Dots. *Chem. Mater.* **2019,** *31* (1), 286-293.

78. Green, M. The Nature of Quantum Dot Capping Ligands. *J. Mater. Chem.* **2010,** *20* (28), 5797-5809.

79. Grandhi, G. K.; M, A.; Viswanatha, R. Understanding the Role of Surface Capping Ligands in Passivating the Quantum Dots Using Copper Dopants as Internal Sensor. *J. Phys. Chem. C* **2016,** *120* (35), 19785–19795.

80. Kim, W.; Lim, S. J.; Jung, S.; Shin, S. K. Binary Amine−Phosphine Passivation of Surface Traps on CdSe Nanocrystals. *J. Phys. Chem. C* **2010,** *114* (3), 1539-1546.

81. Morgan, D. P.; Kelley, D. F. Mechanism of Hole Trap Passivation in CdSe Quantum Dots by Alkylamines. *J. Phys. Chem. C* **2018,** *122* (44), 25661–25667.

82. Talapin, D. V.; Rogach, A. L.; Kornowski, A.; Haase, M.; Weller, H. Highly Luminescent Monodisperse CdSe and CdSe/ZnS Nanocrystals Synthesized in a Hexadecylamine−Trioctylphosphine Oxide−Trioctylphospine Mixture. *Nano Lett.* **2001,** *1* (4), 207-211.

83. Tang, Z.; Kotov, N. A.; Giersig, M. Spontaneous Organization of Single CdTe Nanoparticles into Luminescent Nanowires. *Science* **2002,** *297* (5579), 237-240.

84. Liu, H.; Keuleyan, S.; Guyot-Sionnest, P. n- and p-Type HgTe Quantum Dot Films. *J. Phys. Chem. C* **2012,** *116* (1), 1344-1349.

85. Shen, G.; Guyot-Sionnest, P. HgS and HgS/CdS Colloidal Quantum Dots with Infrared Intraband Transitions and Emergence of a Surface Plasmon. *J. Phys. Chem. C* **2016,** *120* (21), 11744-11753.

86. Wei, S.-H.; Zunger, A. Calculated Natural Band Offsets of All II–VI and III–V Semiconductors: Chemical Trends and the Role of Cation d Orbitals. *Applied Physics Letters* **1998,** *72* (16), 2011-2013.

87. Boles, M. A.; Ling, D.; Hyeon, T.; Talapin, D. V. The Surface Science of Nanocrystals. *Nat. Mater.* **2016,** *15*, 141.

88. De Roo, J.; Ibáñez, M.; Geiregat, P.; Nedelcu, G.; Walravens, W.; Maes, J.; Martins, J. C.; Van Driessche, I.; Kovalenko, M. V.; Hens, Z. Highly Dynamic Ligand Binding and Light Absorption Coefficient of Cesium Lead Bromide Perovskite Nanocrystals. *ACS Nano* **2016,** *10* (2), 2071-2081.

89. Jasieniak, J.; Mulvaney, P. From Cd-Rich to Se-Rich − the Manipulation of CdSe Nanocrystal Surface Stoichiometry. *J. Am. Chem. Soc.* **2007,** *129* (10), 2841-2848.

90. Carroll, G. M.; Tsui, E. Y.; Brozek, C. K.; Gamelin, D. R. Spectroelectrochemical Measurement of Surface Electrostatic Contributions to Colloidal CdSe Nanocrystal Redox Potentials. *Chem. Mater.* **2016,** *28* (21), 7912-7918.

91. Hou, B.; Cho, Y.; Kim, B. S.; Hong, J.; Park, J. B.; Ahn, S. J.; Sohn, J. I.; Cha, S.; Kim, J. M. Highly Monodispersed PbS Quantum Dots for Outstanding Cascaded-Junction Solar Cells. *ACS Energy Lett.* **2016,** *1* (4), 834-839.

92. Moreels, I.; Lambert, K.; Smeets, D.; De Muynck, D.; Nollet, T.; Martins, J. C.; Vanhaecke, F.; Vantomme, A.; Delerue, C.; Allan, G.; Hens, Z. Size-Dependent Optical Properties of Colloidal PbS Quantum Dots. *ACS Nano* **2009,** *3* (10), 3023-3030.

93. Cademartiri, L.; Bertolotti, J.; Sapienza, R.; Wiersma, D. S.; von Freymann, G.; Ozin, G. A. Multigram Scale, Solventless, and Diffusion-Controlled Route to Highly Monodisperse PbS Nanocrystals. *J. Phys. Chem. B* **2006,** *110* (2), 671-673.

94. Moreels, I.; Lambert, K.; De Muynck, D.; Vanhaecke, F.; Poelman, D.; Martins, J. C.; Allan, G.; Hens, Z. Composition and Size-Dependent Extinction Coefficient of Colloidal PbSe Quantum Dots. *Chem. Mater.* **2007,** *19* (25), 6101-6106.

95. Beygi, H.; Sajjadi, S. A.; Babakhani, A.; Young, J. F.; van Veggel, F. C. J. M. Surface Chemistry of As-Synthesized and Air-Oxidized PbS Quantum Dots. *Appl. Surf. Sci.* **2018,** *457*, 1-10.

96. Peng, Z. A.; Peng, X. Formation of High-Quality CdTe, CdSe, and CdS Nanocrystals Using CdO as Precursor. *J. Am. Chem. Soc.* **2001,** *123* (1), 183-184.

97. Qu, L.; Peng, Z. A.; Peng, X. Alternative Routes toward High Quality CdSe Nanocrystals. *Nano Lett.* **2001,** *1* (6), 333-337.

98. Peng, Z. A.; Peng, X. Nearly Monodisperse and Shape-Controlled CdSe Nanocrystals via Alternative Routes: Nucleation and Growth. *J. Am. Chem. Soc.* **2002,** *124* (13), 3343-3353.

99. Hines, M. A.; Scholes, G. D. Colloidal PbS Nanocrystals with Size-Tunable Near-Infrared Emission: Observation of Post-Synthesis Self-Narrowing of the Particle Size Distribution. *Adv. Mater.* **2003,** *15* (21), 1844-1849.

100. Niu, Y.; Pu, C.; Lai, R.; Meng, R.; Lin, W.; Qin, H.; Peng, X. One-Pot/Three-Step Synthesis of Zinc-Blende CdSe/CdS Core/Shell Nanocrystals with Thick Shells. *Nano Res.* **2017,** *10* (4), 1149-1162.

101. Weidman, M. C.; Beck, M. E.; Hoffman, R. S.; Prins, F.; Tisdale, W. A. Monodisperse, Air-Stable PbS Nanocrystals via Precursor Stoichiometry Control. *ACS Nano* **2014,** *8* (6), 6363-6371.

102. Hudson, M. H.; Chen, M.; Kamysbayev, V.; Janke, E. M.; Lan, X.; Allan, G.; Delerue, C.; Lee, B.; Guyot-Sionnest, P.; Talapin, D. V. Conduction Band Fine Structure in Colloidal HgTe Quantum Dots. *ACS Nano* **2018,** *12* (9), 9397–9404.

103. Kroupa, D. M.; Hughes, B. K.; Miller, E. M.; Moore, D. T.; Anderson, N. C.; Chernomordik, B. D.; Nozik, A. J.; Beard, M. C. Synthesis and Spectroscopy of Silver-Doped PbSe Quantum Dots. *J. Am. Chem. Soc.* **2017,** *139* (30), 10382-10394.

104. Pietryga, J. M.; Werder, D. J.; Williams, D. J.; Casson, J. L.; Schaller, R. D.; Klimov, V. I.; Hollingsworth, J. A. Utilizing the Lability of Lead Selenide to Produce Heterostructured Nanocrystals with Bright, Stable Infrared Emission. *J. Am. Chem. Soc.* **2008,** *130* (14), 4879-4885.

105. Yang, H.; Wong, E.; Zhao, T.; Lee, J. D.; Xin, H. L.; Chi, M.; Fleury, B.; Tang, H.-Y.; Gaulding, E. A.; Kagan, C. R.; Murray, C. B. Charge Transport Modulation in PbSe Nanocrystal Solids by Au_xAg_{1-x} Nanoparticle Doping. *ACS Nano* **2018,** *12* (9), 9091–9100.

106. Liu, M.-t.; Li, W. Growth and Optical Property of PbS/ZnS Nanocrystals. *Superlattices Microstruct.* **2018,** *120*, 727-731.

107. Ithurria, S.; Talapin, D. V. Colloidal Atomic Layer Deposition (c-ALD) using Self-Limiting Reactions at Nanocrystal Surface Coupled to Phase Transfer between Polar and Nonpolar Media. *J. Am. Chem. Soc.* **2012,** *134* (45), 18585-18590.

108. Li, J.; Wu, N. Semiconductor-Based Photocatalysts and Photoelectrochemical Cells for Solar Fuel Generation: a Review. *Catal. Sci. Technol.* **2015,** *5* (3), 1360-1384.

109. Jasieniak, J.; MacDonald, B. I.; Watkins, S. E.; Mulvaney, P. Solution-Processed Sintered Nanocrystal Solar Cells via Layer-by-Layer Assembly. *Nano Lett.* **2011,** *11* (7), 2856-2864.

110. Panthani, M. G.; Kurley, J. M.; Crisp, R. W.; Dietz, T. C.; Ezzyat, T.; Luther, J. M.; Talapin, D. V. High Efficiency Solution Processed Sintered CdTe Nanocrystal Solar Cells: The Role of Interfaces. *Nano Lett.* **2014,** *14* (2), 670-675.

111. Dvoretsky, S.; Mikhailov, N.; Sidorov, Y.; Shvets, V.; Danilov, S.; Wittman, B.; Ganichev, S. Growth of HgTe Quantum Wells for IR to THz Detectors. *J. Electron. Mater.* **2010,** *39* (7), 918-923.

112. Becker, C. R. Growth and Properties of HgTe Quantum Wells –A Topic Review. *Phys. Status Solidi B* **2014,** *251* (6), 1125-1132.

113. Arduengo, A. J.; Davidson, F.; Dias, H. V. R.; Goerlich, J. R.; Khasnis, D.; Marshall, W. J.; Prakasha, T. K. An Air Stable Carbene and Mixed Carbene "Dimers". *J. Am. Chem. Soc.* **1997,** *119* (52), 12742-12749.

114. Arduengo, A. J.; Harlow, R. L.; Kline, M. A Stable Crystalline Carbene. *J. Am. Chem. Soc.* **1991,** *113* (1), 361-363.

115. Arduengo, A. J.; Dias, H. V. R.; Harlow, R. L.; Kline, M. Electronic Stabilization of Nucleophilic Carbenes. *J. Am. Chem. Soc.* **1992,** *114* (14), 5530-5534.

116. Arduengo, A. J.; Dias, H. V. R.; Dixon, D. A.; Harlow, R. L.; Klooster, W. T.; Koetzle, T. F. Electron Distribution in a Stable Carbene. *J. Am. Chem. Soc.* **1994,** *116* (15), 6812-6822.

117. Peng, X.; Manna, L.; Yang, W.; Wickham, J.; Scher, E.; Kadavanich, A.; Alivisatos, A. P. Shape Control of CdSe Nanocrystals. *Nature* **2000,** *404* (6773), 59-61.

118. Wang, Y.; Tang, A.; Li, K.; Yang, C.; Wang, M.; Ye, H.; Hou, Y.; Teng, F. Shape-Controlled Synthesis of PbS Nanocrystals via a Simple One-Step Process. *Langmuir* **2012,** *28* (47), 16436-16443.

119. Meyns, M.; Iacono, F.; Palencia, C.; Geweke, J.; Coderch, M. D.; Fittschen, U. E. A.; Gallego, J. M.; Otero, R.; Juárez, B. H.; Klinke, C. Shape Evolution of CdSe Nanoparticles Controlled by Halogen Compounds. *Chem. Mater.* **2014,** *26* (5), 1813-1821.

120. Yong, K.-T.; Sahoo, Y.; Swihart, M. T.; Prasad, P. N. Shape Control of CdS Nanocrystals in One-Pot Synthesis. *J. Phys. Chem. C* **2007,** *111* (6), 2447-2458.

121. McDonald, M. P.; Chatterjee, R.; Si, J.; Jankó, B.; Kuno, M. Dimensional Crossover in Semiconductor Nanostructures. *Nat. Commun.* **2016,** *7*, 12726.

122. Hanson, C. J.; Hartmann, N. F.; Singh, A.; Ma, X.; DeBenedetti, W. J. I.; Casson, J. L.; Grey, J. K.; Chabal, Y. J.; Malko, A. V.; Sykora, M.; Piryatinski, A.; Htoon, H.; Hollingsworth, J. A. Giant PbSe/CdSe/CdSe Quantum Dots: Crystal-Structure-Defined Ultrastable Near-Infrared Photoluminescence from Single Nanocrystals. *J. Am. Chem. Soc.* **2017,** *139* (32), 11081–11088.

123. Manna, L.; Scher, E. C.; Alivisatos, A. P. Synthesis of Soluble and Processable Rod-, Arrow-, Teardrop-, and Tetrapod-Shaped CdSe Nanocrystals. *J. Am. Chem. Soc.* **2000,** *122* (51), 12700-12706.

124. Talapin, D. V.; Nelson, J. H.; Shevchenko, E. V.; Aloni, S.; Sadtler, B.; Alivisatos, A. P. Seeded Growth of Highly Luminescent CdSe/CdS Nanoheterostructures with Rod and Tetrapod Morphologies. *Nano Lett.* **2007,** *7* (10), 2951-2959.

125. Fiore, A.; Mastria, R.; Lupo, M. G.; Lanzani, G.; Giannini, C.; Carlino, E.; Morello, G.; De Giorgi, M.; Li, Y.; Cingolani, R.; Manna, L. Tetrapod-Shaped Colloidal Nanocrystals of II−VI Semiconductors Prepared by Seeded Growth. *J. Am. Chem. Soc.* **2009,** *131* (6), 2274-2282.

126. Wang, J.; Zhao, H.; Zhu, Y.; Song, Y. Shape-Controlled Synthesis of CdSe Nanocrystals via a Programmed Microfluidic Process. *J. Phys. Chem. C* **2017,** *121* (6), 3567-3572.

127. Zhou, J.; Zhu, M.; Meng, R.; Qin, H.; Peng, X. Ideal CdSe/CdS Core/Shell Nanocrystals Enabled by Entropic Ligands and Their Core Size-, Shell Thickness-, and Ligand-Dependent Photoluminescence Properties. *J. Am. Chem. Soc.* **2017,** *139* (46), 16556-16567.

128. Zhong, X.; Han, M.; Dong, Z.; White, T. J.; Knoll, W. Composition-Tunable $Zn_xCd_{1-x}Se$ Nanocrystals with High Luminescence and Stability. *J. Am. Chem. Soc.* **2003,** *125* (28), 8589-8594.

129. Reiss, P.; Protière, M.; Li, L. Core/Shell Semiconductor Nanocrystals. *Small* **2009,** *5* (2), 154-168.

130. Freed, K. F.; Jortner, J. Multiphonon Processes in the Nonradiative Decay of Large Molecules. *J. Chem. Phys.* **1970,** *52* (12), 6272-6291.

131. Cooney, R. R.; Sewall, S. L.; Anderson, K. E. H.; Dias, E. A.; Kambhampati, P. Breaking the Phonon Bottleneck for Holes in Semiconductor Quantum Dots. *Phys. Rev. Lett.* **2007,** *98* (17), 177403.

132. Li, X.-Q.; Nakayama, H.; Arakawa, Y. Phonon Bottleneck in Quantum Dots: Role of Lifetime of the Confined Optical Phonons. *Phys. Rev. B: Condens. Matter Mater. Phy.* **1999,** *59* (7), 5069-5073.

133. Han, P.; Bester, G. Carrier Relaxation in Colloidal Nanocrystals: Bridging Large Electronic Energy Gaps by Low-Energy Vibrations. *Phys. Rev. B: Condens. Matter Mater. Phy.* **2015,** *91* (8), 085305.

134. Guyot-Sionnest, P.; Wehrenberg, B.; Yu, D. Intraband Relaxation in CdSe Nanocrystals and the Strong Influence of the Surface Ligands. *J. Chem. Phys.* **2005,** *123* (7), 074709.

135. Pandey, A.; Guyot-Sionnest, P. Slow Electron Cooling in Colloidal Quantum Dots. *Science* **2008,** *322* (5903), 929-932.

136. Paruta, A. N.; Sciarrone, B. J.; Lordi, N. G. Solubility of Salicylic Acid as a Function of Dielectric Constant. *J. Pharm. Sci.* **1964,** *53* (11), 1349-1353.

137. Chakraborty, I.; Mitra, D.; Moulik, S. P. Spectroscopic Studies on Nanodispersions of CdS, HgS, Their Core-Shells and Composites Prepared in Micellar Medium. *J. Nanopart. Res.* **2005,** *7* (2), 227-236.

138. Siemsen, K. J.; Riccius, H. D. Preparation and Optical Properties of Evaporated β-HgS Films. *Phys. Status Solidi B* **1970,** *37* (1), 445-451.

139. Jasieniak, J.; Smith, L.; Embden, J. v.; Mulvaney, P.; Califano, M. Re-Examination of the Size-Dependent Absorption Properties of CdSe Quantum Dots. *J. Phys. Chem. C* **2009,** *113* (45), 19468-19474.

140. Scotognella, F.; Valle, G.; Srimath Kandada, A. R.; Zavelani-Rossi, M.; Longhi, S.; Lanzani, G.; Tassone, F. Plasmonics in Heavily-Doped Semiconductor Nanocrystals. *Eur. Phys. J. B* **2013,** *86* (4), 1-13.

141. Buonsanti, R.; Llordes, A.; Aloni, S.; Helms, B. A.; Milliron, D. J. Tunable Infrared Absorption and Visible Transparency of Colloidal Aluminum-Doped Zinc Oxide Nanocrystals. *Nano Lett.* **2011,** *11* (11), 4706-4710.

142. Rowe, D. J.; Jeong, J. S.; Mkhoyan, K. A.; Kortshagen, U. R. Phosphorus-Doped Silicon Nanocrystals Exhibiting Mid-Infrared Localized Surface Plasmon Resonance. *Nano Lett.* **2013,** *13* (3), 1317-1322.

143. Zhao, Y.; Pan, H.; Lou, Y.; Qiu, X.; Zhu, J.; Burda, C. Plasmonic $Cu_{2-x}S$ Nanocrystals: Optical and Structural Properties of Copper-Deficient Copper(I) Sulfides. *J. Am. Chem. Soc.* **2009,** *131* (12), 4253-4261.

144. Agrawal, A.; Cho, S. H.; Zandi, O.; Ghosh, S.; Johns, R. W.; Milliron, D. J. Localized Surface Plasmon Resonance in Semiconductor Nanocrystals. *Chem. Rev.* **2018,** *118* (6), 3121-3207.

145. Pines, D.; Bohm, D. A Collective Description of Electron Interactions: II. Collective vs Individual Particle Aspects of the Interactions. *Phys. Rev.* **1952,** *85* (2), 338-353.

146. Genzel, L.; Martin, T. P.; Kreibig, U. Dielectric Function and Plasma Resonances of Small Metal Particles. *Z. Phys. B: Condens. Matter* **1975,** *21* (4), 339-346.

147. Aikens, C. M.; Li, S.; Schatz, G. C. From Discrete Electronic States to Plasmons: TDDFT Optical Absorption Properties of Ag_n (n = 10, 20, 35, 56, 84, 120) Tetrahedral Clusters. *J. Phys. Chem. C* **2008,** *112* (30), 11272-11279.

148. Scholl, J. A.; Koh, A. L.; Dionne, J. A. Quantum Plasmon Resonances of Individual Metallic Nanoparticles. *Nature* **2012,** *483* (7390), 421-427.

149. Schimpf, A. M.; Thakkar, N.; Gunthardt, C. E.; Masiello, D. J.; Gamelin, D. R. Charge-Tunable Quantum Plasmons in Colloidal Semiconductor Nanocrystals. *ACS Nano* **2014,** *8* (1), 1065-1072.

150. Zhang, H.; Kulkarni, V.; Prodan, E.; Nordlander, P.; Govorov, A. O. Theory of Quantum Plasmon Resonances in Doped Semiconductor Nanocrystals. *J. Phys. Chem. C* **2014,** *118* (29), 16035-16042.

151. Jain, P. K. Plasmon-in-a-Box: On the Physical Nature of Few-Carrier Plasmon Resonances. *J. Phys. Chem. Lett.* **2014,** *5* (18), 3112-3119.

152. Yu, P.; Cardona, M. *Fundamentals of Semiconductors*. Springer-Verlag Berlin Heidelberg: 2010.

153. Faucheaux, J. A.; Jain, P. K. Plasmons in Photocharged ZnO Nanocrystals Revealing the Nature of Charge Dynamics. *J. Phys. Chem. Lett.* **2013,** *4* (18), 3024-3030.

154. Monreal, R. C.; Antosiewicz, T. J.; Apell, S. P. Diffuse Surface Scattering and Quantum Size Effects in the Surface Plasmon Resonances of Low-Carrier-Density Nanocrystals. *J. Phys. Chem. C* **2016,** *120* (9), 5074-5082.

155. Delerue, C. Minimum Line Width of Surface Plasmon Resonance in Doped ZnO Nanocrystals. *Nano Lett.* **2017,** *17* (12), 7599-7605.

156. Wehrenberg, B. L.; Guyot-Sionnest, P. Electron and Hole Injection in PbSe Quantum Dot Films. *J. Am. Chem. Soc.* **2003,** *125* (26), 7806-7807.

157. Hatami, S.; Wurth, C.; Kaiser, M.; Leubner, S.; Gabriel, S.; Bahrig, L.; Lesnyak, V.; Pauli, J.; Gaponik, N.; Eychmuller, A.; Resch-Genger, U. Absolute Photoluminescence Quantum Yields of IR26 and IR-Emissive $Cd_{1-x}Hg_xTe$ and PbS Quantum Dots - Method- and Material-Inherent Challenges. *Nanoscale* **2015,** *7* (1), 133-143.

158. Evans, C. M.; Evans, M. E.; Krauss, T. D. Mysteries of TOPSe Revealed: Insights into Quantum Dot Nucleation. *J. Am. Chem. Soc.* **2010,** *132* (32), 10973-10975.

159. Lian, L.; Xia, Y.; Zhang, C.; Xu, B.; Yang, L.; Liu, H.; Zhang, D.; Wang, K.; Gao, J.; Zhang, J. In Situ Tuning the Reactivity of Selenium Precursor To Synthesize Wide Range Size, Ultralarge-Scale, and Ultrastable PbSe Quantum Dots. *Chem. Mater.* **2018,** *30* (3), 982–989.

160. Frenette, L. C.; Krauss, T. D. Uncovering Active Precursors in Colloidal Quantum Dot Synthesis. *Nat. Commun.* **2017,** *8* (1), 2082.

161. Peng, X.; Wickham, J.; Alivisatos, A. P. Kinetics of II-VI and III-V Colloidal Semiconductor Nanocrystal Growth: "Focusing" of Size Distributions. *J. Am. Chem. Soc.* **1998,** *120* (21), 5343-5344.

162. Franke, D.; Harris, D. K.; Chen, O.; Bruns, O. T.; Carr, J. A.; Wilson, M. W. B.; Bawendi, M. G. Continuous Injection Synthesis of Indium Arsenide Quantum Dots Emissive in the Short-Wavelength Infrared. *Nat. Commun.* **2016,** *7*, 12749.

163. Tamang, S.; Lee, S.; Choi, H.; Jeong, S. Tuning Size and Size Distribution of Colloidal InAs Nanocrystals via Continuous Supply of Prenucleation Clusters on Nanocrystal Seeds. *Chem. Mater.* **2016,** *28* (22), 8119-8122.

164. Hines, D. A.; Becker, M. A.; Kamat, P. V. Photoinduced Surface Oxidation and Its Effect on the Exciton Dynamics of CdSe Quantum Dots. *J. Phys. Chem. C* **2012,** *116* (24), 13452-13457.

165. Hens, Z.; Martins, J. C. A Solution NMR Toolbox for Characterizing the Surface Chemistry of Colloidal Nanocrystals. *Chem. Mater.* **2013,** *25* (8), 1211-1221.

166. Li, X.; Cao, F.; Yu, D.; Chen, J.; Sun, Z.; Shen, Y.; Zhu, Y.; Wang, L.; Wei, Y.; Wu, Y.; Zeng, H. All Inorganic Halide Perovskites Nanosystem: Synthesis, Structural Features, Optical Properties and Optoelectronic Applications. *Small* **2017,** *13* (9), 1603996.

167. Zhang, Q.; Yin, Y. All-Inorganic Metal Halide Perovskite Nanocrystals: Opportunities and Challenges. *ACS Central Sci.* **2018,** *4* (6), 668-679.

168. Li, Z.-J.; Hofman, E.; Li, J.; Davis, A. H.; Tung, C.-H.; Wu, L.-Z.; Zheng, W. Photoelectrochemically Active and Environmentally Stable $CsPbBr_3/TiO_2$ Core/Shell Nanocrystals. *Adv. Funct. Mater.* **2018,** *28* (1), 1704288.

169. Chen, D.; Fang, G.; Chen, X. Silica-Coated Mn-Doped $CsPb(Cl/Br)_3$ Inorganic Perovskite Quantum Dots: Exciton-to-Mn Energy Transfer and Blue-Excitable Solid-State Lighting. *ACS Appl. Mater. Interfaces* **2017,** *9* (46), 40477–40487.

170. Lin, Q.; Yun, H. J.; Liu, W.; Song, H.-J.; Makarov, N. S.; Isaienko, O.; Nakotte, T.; Chen, G.; Luo, H.; Klimov, V. I.; Pietryga, J. M. Phase-Transfer Ligand Exchange of Lead Chalcogenide Quantum Dots for Direct Deposition of Thick, Highly Conductive Films. *J. Am. Chem. Soc.* **2017,** *139* (19), 6644-6653.

171. Gordon, T. R.; Paik, T.; Klein, D. R.; Naik, G. V.; Caglayan, H.; Boltasseva, A.; Murray, C. B. Shape-Dependent Plasmonic Response and Directed Self-Assembly in a New Semiconductor Building Block, Indium-Doped Cadmium Oxide (ICO). *Nano Lett.* **2013,** *13* (6), 2857-2863.